Investigation of immunosuppressive signals in response to irradiation in murine oral cancer cell lines

Caitlin Marie Beecher Martinsen

Biophysics and Medical Physics

Department of Physics

Faculty of Mathematics and Natural Sciences

University of Oslo

August 2023

Investigation of immunosuppressive signals in response to irradiation in murine oral cancer cell lines.

-

Caitlin Marie Beecher Martinsen

-

2023

Investigation of immunosuppressive signals in response to irradiation in murine oral cancer cell lines.

Caitlin Marie Beecher Martinsen

http://www.duo.uio.no/

Trykk: Reprosentralen, Universitetet i Oslo

Acknowledgments

This project was carried out the Biophysics and Medical Physics group at the Department of Physics, University of Oslo.

I extend my deepest gratitude to all my supervisors for giving me the opportunity to work on this project and allowing me to expand my knowledge on this important topic. To my main supervisor, Prof. Nina F. J. Edin, thank you for always having your door open, for giving me valuable guidance in the field of radiobiology and introducing me to the very interesting intersection where physics and biology meet. You have made me appreciate science in a whole new way.

I want to thank the senior engineers at the group, especially Julia Marzioch, for teaching me cell culturing and for being someone I could always come to with questions. I am grateful for my time at the Biophysics and Medical Physics group, and I will always remember the meaningful discussions, encouraging environment and the fantastic tradition of 'Cake Friday'.

I am very thankful to my colleagues at Curida Diatec, where I have had the privilege of working alongside my thesis. Your encouragement, valuable insights and expertise in laboratory work were very valuable throughout the work on this thesis.

I would like to thank my friends and family for being so supportive and understanding throughout this whole project, and for encouraging me to keep moving forward when things became difficult. To Henrik for encouraging me to pursue a master's degree, for all his love and support and for sharing my love of science.

August 2023,

Caitlin Marie Beecher Martinsen

Abstract

Combining radiation therapy with immunotherapy using immune checkpoint inhibitors has shown promise in treatment of cancers with a lower cure rate, including head and neck cancer (HNC). The effect of combination treatment has shown varied results, which is most likely due to a lack of immunogenic signaling (the immune system does not recognize the cancer as foreign). Radiation is known to modulate immune responses and high doses in the order of 8-12 Gy have been shown to induce an immunogenic response in cancer cells leading to anti-tumor cytotoxic T-cell activation. However, high doses of radiation have also been shown to recruit immune-suppressive cells and increase immune-regulatory cytokine secretion, which may impair the anti-tumor immune response.

The primary aim of this thesis was to investigate the complex immune related defense mechanisms exhibited by tumor cells in response to ionizing radiation. Two different immunosuppressive factors, PD-L1 (programmed death ligand 1) and PGE_2 (prostaglandin E_2), and their response to irradiation were studied. The PD-1/PD-L1 pathway's main purpose is to control the immune response, prevent an autoimmune response and to spare healthy tissue near the tumor volume, by inhibiting important immune cells, like cytotoxic T-cells. PGE_2 work as an inhibitory damage associated molecular pattern (iDAMPs), preventing cytotoxic T-cell activation by DAMPs. The murine oral cancer cell lines with different immunogenicity were used, MOC1 (very immunogenic) and MOC2 (less immunogenic). The cancer cells were irradiated with different doses, fractionation schemes and radiation types, followed by flow cytometry or ELISA, to quantify the two immunosuppressing signals.

The results showed that the less immunogenic MOC2 cells had higher levels of both immunosuppressive markers without irradiation, but no further induction by photon irradiation, except for 3 fractions of 8 Gy. The more immunogenic MOC1 cells with initially lower levels of both immunosuppressive markers responded to photon irradiation with an increase in both markers, also showing the highest effect for 3 fractions of 8 Gy. There was no significant difference between the PD-L1 levels for the same total dose given in either one or two fractions in MOC1 or MOC2 cells. One experiment with protons measuring PD-L1 showed a very high effect when the cells were positioned in the distal end of the proton Bragg peak for both cell lines, even for the low dose of 4 Gy. However, the PD-L1 levels for cells irradiated in front of the proton Bragg peak were comparable to those of photon irradiation.

These findings indicate that cancer cells have intricate immunosuppressor mechanisms that are upregulated in response to radiation. It also indicates that cancers with characteristics like MOC1 cells, which is a more immunogenic cell line, may benefit more from combination therapy of immune checkpoint inhibitors and radiation. Therefore, treatment involving the combination of radiation and immune checkpoint inhibitors targeting the COX-2 and PD-L1 pathways, should be investigated to enhance tumor rejection in therapies.

Abbreviations

Abbreviations	Definitions
AP cells	Antigen presenting cells
ATP	Adenosine triphosphate
B-cell	B-lymphocyte
BSA	Bovine serum albumin
CD4 T-cells	Helper T-cells
CD8 T-cells	Cytotoxic T-cells
cGAMP	Cyclic guanosine monophosphate–adenosine monophosphate
cGAS-STING	Cyclic GMP-AMP synthase - stimulator of interferon genes
CO_2	Carbon dioxide
COX	Cyclooxygenase
DAMP	Damage-associated molecular pattern
DNA	Deoxyribonucleic acid
DSB	Double strand break
ELISA	Enzyme-linked immunoassay
4-PL	Four-parameter logistic
FSC	Forward scatter
G_0 phase	Gap 0 phase
G_1 phase	Gap 1 phase
G_2 phase	Gap 2 phase
Gy	Gray
HDRT	High Dose Radiation Therapy
HEPA	High efficiency particulate air

HMGB1	High-Mobility-Group Box 1
HNC	Head and neck cancer
HNSCC	Head and neck squamous cell carcinoma
HRP	Horseradish peroxidase
HRR	Homologous recombination repair
iDAMP	Inhibitory damage-associated molecular pattern
ICB	Immune checkpoint blocking
ICD	Immunogenic cell death
ICI	Immune chekpoint inhibitor
KERMA	Kinetic energy released in matter
LAF	Laminar air flow
LET	Linear energy transfer
M phase	Mitosis phase
MeV	Megaelectron volt
MOC1	Murine oral cancer 1
MOC2	Murine oral cancer 2
NHEJ	Non-homologous end joining
NK cells	Natural killer cells
NSB	Non-Specific Binding
OAR	Organs at risk
OCL	Oslo cyclotron lab
OD	Optical density
PBS	Phosphate-buffered saline
PD-1	Programmed cell death 1

PD-L1	Programmed death-ligand 1
PGE_2	Prostaglandin E2
PI	Propidium iodide
PMMA	Poly methyl methacrylate
PMT	Photomultiplier tubes
RBE	Relative biological effect
RNA	Ribonucleic acid
S phase	Synthesis phase
SSB	Single strand break
SSC	Side scatter
SSD	Source surface distance
T-cell	T-lymphocyte
TME	Tumor microenvironment

Table of Contents

1 Introduction

Head and neck squamous cell carcinomas (HNSCCs) represent a challenging and diverse cancer type, making them difficult to treat effectively. In Norway there were 737 new cases of head and neck cancer in 2021, constituting 2 % of all new cancer cases (Kreftregisteret, 2022). Despite substantial effort invested in therapeutic development, the 5-year survival rate for HNSCC remains discouragingly low. The reason being late-stage diagnoses, recurrent metastasis, and the resistance that HNSCC shows against available treatments, including radiation therapy.

Radiation therapy is the treatment modality used for over 50% of cancer patients, with either a curative or palliative goal. The purpose of radiation therapy is to deliver ionizing radiation to cancer cells, causing a permanent halt in their proliferation (Rodriguez-Ruiz et al., 2020). For HNSCC patients, radiotherapy is intricate due to the presence of multiple organs at risk (OAR) in proximity. Norway will establish its first proton therapy center in 2024. Protons deposit most of their energy at the end of their track in the so-called Bragg peak, where they have a higher linear energy (LET) transfer compared to conventional photon radiation. Higher LET causes more damage in the cells, consequently producing higher radiobiological effects. In addition, there is no dose behind the Bragg peak. Proton therapy has become a promising type of radiotherapy to administer to HNSCC patients, since it can deliver high doses to precise areas, while sparing surrounding healthy tissue.

It has become clear that ionizing radiation effects go beyond halting the proliferation of cancer cells. It has been shown to also initiate an adaptive, tumor targeting immune response that operates locally and systematically to control the tumor. The response originates from ionizing radiation's ability to increase the antigen expression on cancer cells and facilitate the release of immunostimulatory cytokines and damage associated molecular patterns (DAMPs). This recruits and activates cells from the immune system to initiate anticancer immunity (Rodriguez-Ruiz et al., 2020). Radiation can thus alter the immunogenicity of tumors and increase their susceptibility to immune recognition (Mckelvey et al., 2018). Combining radiation therapy with immune checkpoint inhibitors, such as PD-L1 inhibitor, has shown promise in enhancing the effectiveness of the treatment. However, the optimal radiation type, doses and fractionation scheme vary for different tumors and not all patients benefit from the treatment. Tumor type and its characteristics significantly influence the responses.

HNSCCs are highly immune-suppressive, allowing them to evade immune surveillance and recognition by the immune cells. One such immunosuppressive mechanism is the presence of PD-L1 protein on the cancer cell membrane, which binds PD-1 to immune cells including the cytotoxic T-cells thereby inhibiting their anti-tumor activity. The targeting of the PD-1/PD-L1 binding using either PD-L1 or PD-1 inhibitors has emerged as a promising strategy in

cancer immunotherapy. However, despite its high efficacy in some patients, the majority of patients do not respond to the treatment (Donlon et al., 2021). This is most likely due to a lack of immunogenic signaling (the immune system does not recognize the cancer as foreign). Radiation is known to modulate immune responses and high doses in the order of 8-12 Gy (HDRT) have been shown to induce an immunogenic response in cancer cells leading to anti-tumor cytotoxic T-cell activation. A combination of immunotherapy and radiation has therefore been introduced, but still less than 50% of the patients respond (Faivre-Finn et al., 2021).

There are increasing evidence that radiotherapy act as a 'double-edged sword', where it can induce immunogenicity but also immunosuppression (Donlon et al., 2021) and high doses have been shown to recruit immune-suppressive cells and increase immune-regulatory cytokine secretion, which may impair the anti-tumor immune response (Barsoumian et al., 2022).

In this thesis, two different immunosuppressive pathways and their response to irradiation are studied. One is upregulation of PD-L1 on tumor cells. The other is secretion of PGE_2 (prostaglandin E2). PGE_2 is a naturally occurring prostanoid, with various functions depending on the tissue. Like immunogenic DAMPs, it has been seen to be secreted by necrotic cancer cells, and to work as an inhibitory damage associated molecular pattern (iDAMPs), preventing cytotoxic T-cell activation by DAMPs (Hangai et al., 2016).

The primary aim of this thesis is thus to investigate the complex immune related defense mechanisms exhibited by tumor cells in response to ionizing radiation. To investigate the aim, cancer cells were irradiated with different doses, fractionation schemes and radiation types, followed by molecular assays, flow cytometry and ELISA, to quantify the two immunosuppressing signals. To compare the response based on tumor characteristics and immunogenicity variations, two different tumor models MOC1 and MOC2 with tumor characteristics and immunogenicity were used.

2 Theory

2.1 Radiation physics

Photons have been, and still are, the most common type of radiation used in cancer therapy (Rodríguez-Ruiz et al., 2018), They are administered either in the form of x-rays or γ-rays, where only the point of origin separates them (Hall & Giaccia, 2019). Today, particle radiation, such as protons and heavy carbon ions, have become more common to use in treatments, due to their advantageous dose distribution in the tissue (Hall & Giaccia, 2019). The following section describes how these two types of radiation interact and deposit energy in matter and how they are generated.

2.1.1 Ionizing radiation

Ionizing radiation is characterized by having the potential to excite the atoms in the matter they interact with (Attix, 1986). To achieve this, the radiation must have a higher kinetic energy than the ionization potential of the atoms and molecules in the matter. This ionization potential varies between a few electron volts to 24.6 eV depending on the atoms in the matter (Podgorsak, 2010).

The different types of ionizing radiation can be classified into two categories: directly ionizing radiation and indirectly ionizing radiation (Podgorsak, 2010). Directly ionizing radiation deposits energy in matter through a one-step process described in 2.1.1.2 and is performed by charged particles (electrons, protons, α-particles). Indirectly ionizing radiation deposits energy through a two-step process and is performed by a neutral particle (photons or neutrons). First, the neutral particle releases a charged particle through the interaction described in section 2.1.1.1. The second step is equivalent to directly ionizing radiation, where the charged particle deposits the energy in the matter (Podgorsak, 2010).

Another way to classify ionizing radiation, is by their nature; Photons are categorized as electromagnetic radiation as they behave like waves, while protons and other particles can be classified as particle radiation. The radiation in these two categories interact and ionize the atoms differently (Attix, 1986). This thesis will focus on the interactions of photons and protons as these are the radiation types used.

2.1.1.1 Electromagnetic radiation

Electromagnetic radiation consists of discrete energy quanta called photons (Attix, 1986). Photons can be divided into different categories based on their origin, where x-rays are the main focus in this thesis. X-rays can be produced in two ways: Characteristic x-rays and bremsstrahlung x-rays. Characteristic x-rays are produced when an orbital electron fills up an unoccupied spot in an orbital of lower energy. The energy difference is released as x-ray photons with a quantum energy that is characteristic for the different elements/material it is

emitted from. Bremsstrahlung x-rays are produced when charged particles are slowed down in a Coulomb force field (Podgorsak, 2010). This is the type of x-ray that is most used in diagnostics (Hall & Giaccia, 2019). The quantum energy (E) of a photon is given in equation 1:

$$E = \frac{\hbar c}{\lambda} \tag{1}$$

Where $\hbar$ is Plancks constant, c is the speed of light in vacuum and λ is the wavelength of the photon.

The way photons interact with material depends on their kinetic energy and the atomic number Z of the target material. Z is defined as the number of protons in the material (Attix, 1986). The dependency on Z and energy is shown in Figure 1. In biophysics, this target material will most commonly be human tissue which has a low atomic number Z. The three main photon interactions that are relevant for the energy deposited in a tissue are: Compton effect, photoelectric effect, and pair production (Attix, 1986).

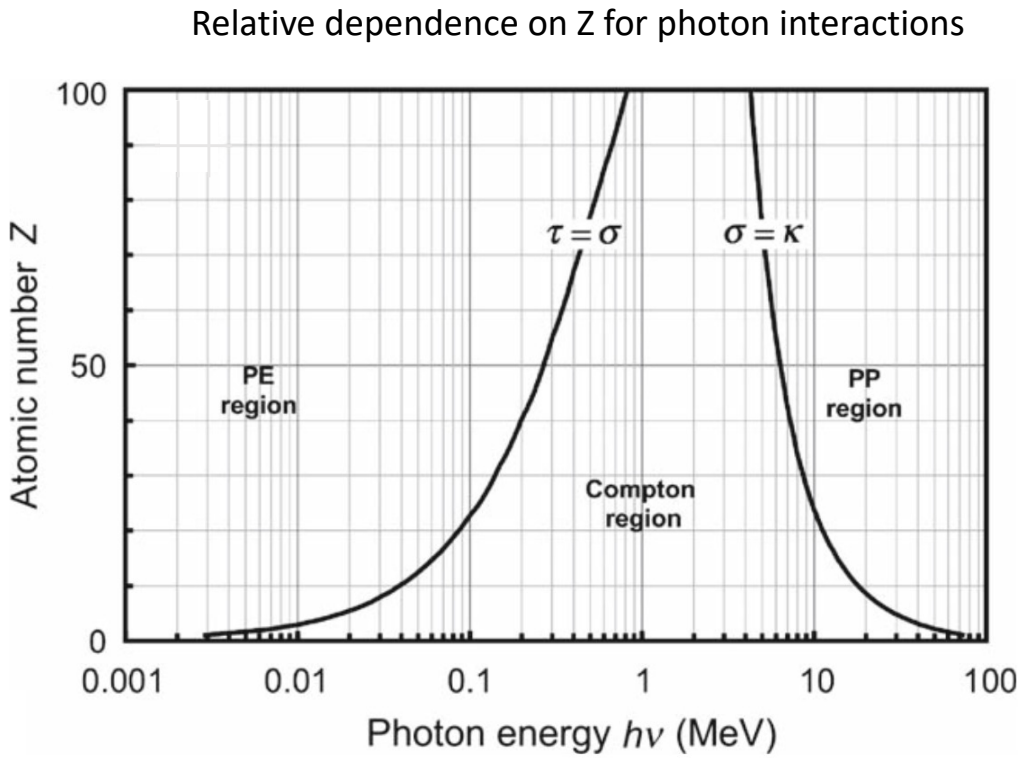

Figure 1: Relative dependence on Z-value for the three main types of photon interactions. For the left region (low energy), photoelectric effect is the dominant interaction. In the middle region, Compton effect is the main interaction and pair production is the main interaction for the right region (high energy). On the higher atomic number Z, photoelectric effect and pair production have the wider regions, and Compton effect have the wider regions for lower atomic number Z. In the area $\tau = \sigma$, the attenuation coefficient for photoelectric effect and Compton are the same. In the area $\sigma = \kappa$, the attenuation coefficient for Compton and pair production are the same. The figure is a modified version of figure 8.5 borrowed from (Podgorsak, 2010).

The Compton effect

The Compton effect describes the process when an incident photon interacts with an electron that has a lower binding energy compared to the photon (a 'free' electron) (Hall & Giaccia, 2019). A portion of the energy from the photon is transferred to the 'free' electron as kinetic energy, while the rest remains with the photon as it is deflected (Attix, 1986). This interaction is shown in Figure 2. The photon continues with the energy left after the interaction, deflected away from its path (Hall & Giaccia, 2019). One photon can continue to interact with additional 'free' electrons as long as it has sufficient energy. Therefore, the Compton effect can produce many fast-traveling electrons, that have the potential to cause biological damage to the tissue (Hall & Giaccia, 2019). In material with low Z, like human tissue, the Compton effect is the dominant interaction (Attix, 1986).

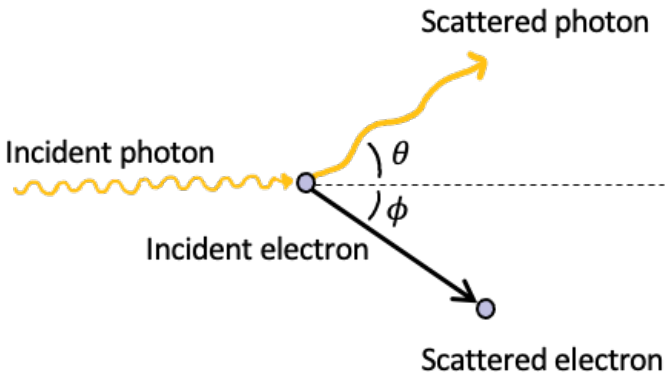

Figure 2: The Compton effect, where an incident photon interacts with a 'free' electron. A portion of the energy from the incident photon is transferred to the scattered photon, which travels with an angle θ. The rest of the energy is transferred to the scattered electron, which travels from the incident area with angle ϕ.

The Photoelectric effect

The photoelectric effect is the most important interaction for photons with lower energies interacting with a high Z material. In this interaction, the photon interacts with a tightly bound electron (an electron that has a high binding energy relative to the energy of the incoming photon) (Podgorsak, 2010). The photon is absorbed by the electron, Figure 3A, and the electron is ejected from its orbital, Figure 3B, with the kinetic energy $E_K = h\nu - E_B$, where $h\nu$ is the energy of the incoming photon and E_B is the binding energy of the electron (Hall & Giaccia, 2019).

After the photoelectric effect occurs, there is a vacancy in the orbital. This is filled by either an electron from a higher energy orbital or an outside electron. When the electron vacancy is filled up by an electron from a higher energy orbital, the difference in energy is emitted as a characteristic x-ray (Podgorsak, 2010). These x-rays have very low kinetic energy when the photoelectric effects occur in human tissue and will not contribute to the dose deposited in the tissue (Hall & Giaccia, 2019).

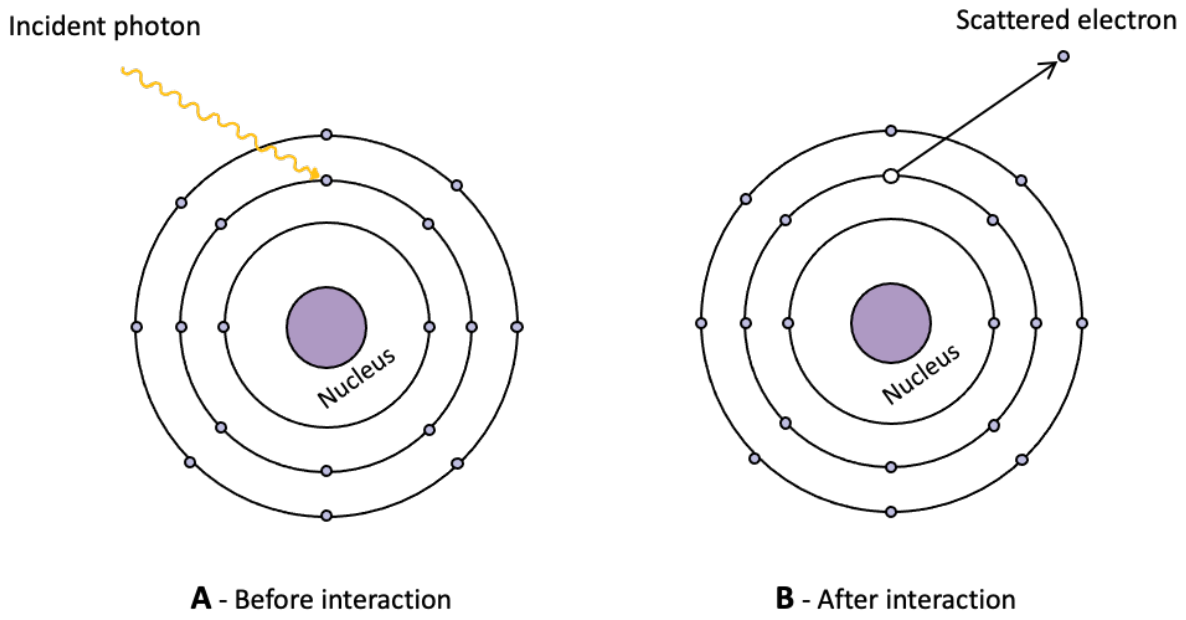

Figure 3: Photoelectric effect. ***A)*** *An incident photon interacts with a tightly bound electron.* ***B)*** *The photon is absorbed by the electron and the electron is ejected as a scattered electron.*

Pair production

In the presence of a Coulomb field, a high energy photon can be transformed into an electron-positron pair, Figure 4. Pair production can only happen if the energy of the incident photons exceeds $2m_e c^2$ (Podgorsak, 2010). This process can also occur in the Coulomb field of an electron, a process called triplet production. In this interaction, three particles (two electrons and a positron) leave the interaction site (Podgorsak, 2010).

The produced positron will move through the target material and lose its kinetic energy through collisions and Coulomb interactions. When the positron has lost all its kinetic energy, it will undergo an electron-positron annihilation with an orbital electron in the target material (Podgorsak, 2010).

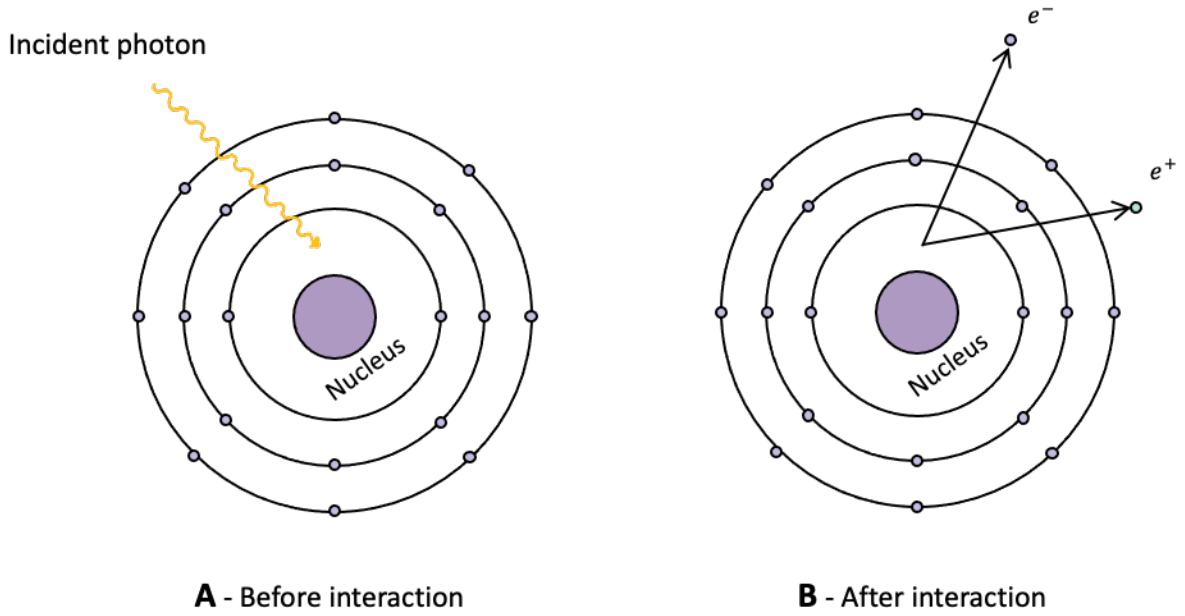

*Figure 4: Pair production. When a high energy photon interacts with the Coulomb field of the atom **(A)**, the photon can be transformed into an electron-positron pair **(B)**.*

Total photon attenuation

The linear attenuation coefficient μ, is the probability per unit length that a photon will interact with the atoms in the absorbing material. This is an important parameter used for characterization of penetrating x-rays (Podgorsak, 2010). This parameter is dependent on the energy of the photon, given in equation 1, and the atomic number Z of the absorbing media (Podgorsak, 2010). Since the coefficient is highly dependent on the material of the absorber, it is common to refer to it as the mass attenuation coefficient μ_m which is defined in equation 2:

$$\mu_m = \frac{\mu}{\rho} \tag{2}$$

Where ρ is the mass density of the absorbing material. The total mass attenuation coefficient for photon interactions is given in equation 3, and consists of the contributions from the photoelectric effect, the Compton effect, pair production and Rayleigh scattering (Attix, 1986).

$$\frac{\mu}{\rho} = \frac{\tau}{\rho} + \frac{\sigma}{\rho} + \frac{\kappa}{\rho} + \frac{\sigma_R}{\rho} \tag{3}$$

Rayleigh scattering is an interaction where the scattered photon does not have enough energy to transfer it to charged particles and is therefore negligible for the dose deposited in biological tissue (Attix, 1986).

2.1.1.2 Particle radiation

When a charged particle is traversing through matter, it experiences Coulomb interactions with the orbital electrons and nuclei of the atoms in the material (Podgorsak, 2010). These interactions are dependent on the relative size of the radius of the atom (**a**) and the distance between the nucleus and the trajectory of the charged particle (**b**) (Attix, 1986). This is illustrated in Figure 5. There are three main processes: soft collisions, hard collisions, and radiation collision (Podgorsak, 2010).

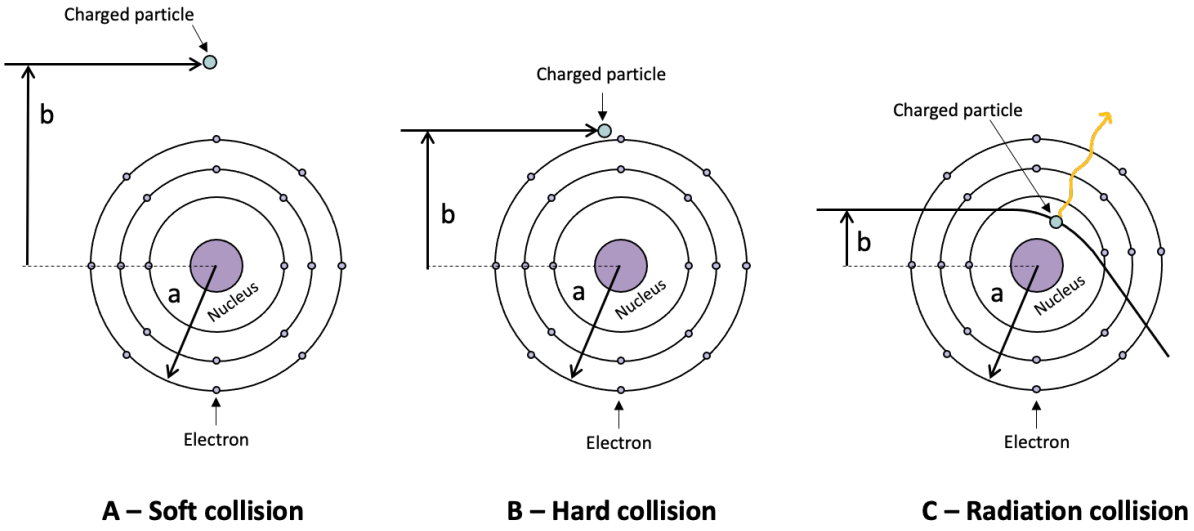

*Figure 5: How charged particles interact with an atom is dependent on the relative size between the radius of the atom (**a**) and the distance from the nucleus of the atom to the travelling charged particle (**b**). Panel A shows a soft collision where **a** >> **b**, panel B shows a hard collision where **a**~b and panel C shows a radiation collision where **a**<<**b**. In the collision in panel C, a photon is produced. The figure is adapted from figure 6.1 (Podgorsak, 2010).*

Soft collisions

Interactions where the atomic radius **a** is much greater than the impact parameter **b** are called soft collisions (Figure 5A). In this interaction, the electrical field of the charged particle affects the whole atom. This can result in either exciting the atom to a higher energy level or ionizing the atom by ejecting a valence electron (Podgorsak, 2010).

During a soft collision, the energy transferred between the charged particle and the atom is relatively low. However, despite the small energy transfer, soft collisions have the highest probability of occurring compared to other types of collisions (Podgorsak, 2010). The soft collisions account for around 50 % of the energy deposited in the material (Attix, 1986).

Hard collisions

The interactions where the values for **a** and **b** are of the same order are called hard collisions (Figure 5B). In these collisions, the charged particle is more likely to interact with a single atomic orbital electron (Podgorsak, 2010). Unlike soft collisions, hard collisions involve a significant transfer of energy. The electron that is ejected has enough energy to continue to

interact with other atoms in the material (Podgorsak, 2010). The probability of hard collisions is generally low, but the energy transferred in this collision is relatively large. The particle loses about 50% of its kinetic energy through this collision type (Podgorsak, 2010).

Radiation collision

The last possible interaction is the situation where the value **a** is much greater than value **b**, meaning that the Coulomb-force interaction will take place with the nucleus (Figure 5C). For most of these interactions, except 2-3%, there is not transferred any energy as the charged particle is scattered elastically and does not excite the nucleus or produce a photon (Attix, 1986). For the 2-3 % that is not elastic scattering, an inelastic radiative interaction occurs, which results in an x-ray photon being emitted (Attix, 1986). In these cases, the charged particle is transferring up to 100% of its kinetic energy to the photon and slowing down in the process (Attix, 1986).These specific x-rays are called bremsstrahlung (Podgorsak, 2010). The probability of interactions is proportional to Z^2, which is why a material with a high Z-number is preferred when x-rays are produced (Attix, 1986). The bremsstrahlung intensity is inversely proportional to m^2, meaning that only light particles such as electrons experience significant energy loss through these interactions (Podgorsak, 2010).

2.1.1.3 Stopping power

The stopping power is used to describe a charged particle's gradual loss of energy when traversing through a material (Podgorsak, 2010). It is defined as the rate of energy loss per unit of length by a charged particle with kinetic energy E_k when traversing a material with atomic number Z (Attix, 1986). The unit of stopping power is MeV/cm or J/m (Attix, 1986).

Stopping power can be divided into collision stopping power and radiative stopping power (Podgorsak, 2010). Collision stopping power is the sum of energy lost from the soft and hard collisions described in 2.1.1.2, and this energy is deposited where the interactions occur. The radiative stopping power results from the bremsstrahlung production and the energy can be deposited far away from the track (Podgorsak, 2010).

As mentioned, it is only light charged particles that experience significant energy loss through bremsstrahlung interactions. Therefore, the radiation loss is negligible for heavy charged particles in comparison with the collision loss (Podgorsak, 2010). The Bethe-Bloch is given in equation 4, and defines the collision stopping power (S_{col}) for a heavy charged particle with charge z and atomic number A.

$$S_{col} = 4\pi \frac{ZN_A}{A} \left(\frac{e^2}{4\pi\epsilon_0}\right)^2 \frac{z^2}{m_e c^2 \beta^2} \left[ln \frac{2m_e v^2}{I} - ln(1-\beta^2) - \beta^2\right] \quad (4)$$

Where N_A is Avogadros number, e is the elementary charge, ϵ_0 is the permittivity of vacuum, m_e is the rest mass of the electron, I is the mean ionization/excitation potential of the absorber atom, v is the velocity of the charged particle and the β is the relationship between v and the speed of light $\frac{v}{c}$ (Podgorsak, 2010). The equation shows that the collision stopping power is dependent on the kinetic energy of the particle, with the strongest dependence from the β^2 factor outside the brackets (Attix, 1986). When the kinetic energy and therefore the velocity of the particle decreases, the signal $\beta^2 = \left(\frac{v}{c}\right)^2$ approches 0. As the stopping power is dependent on the inverse of this factor, this situation makes the stopping power increase drastically. Meaning that for particles with low kinetic energy, the stopping power increases and reaches a peak, called a Bragg peak, before the particle loses its kinetic energy and there is not deposited any more energy (Podgorsak, 2010). This type of dose distribution is characteristic for all heavy charged particles, Figure 6. This distribution is useful in radiotherapy, as it allows for a high and precise dose, deep in the tissue, while minimizing the dose to the surrounding normal tissue behind the Bragg peak (Attix, 1986).

2.1.1.4 LET

Linear energy transfer (LET) is the energy transferred per unit length of the track and describes the density of the ionizations along the track. LET is measured in keV/μm (Hall & Giaccia, 2019).

How the dose is deposited in the tissue is highly dependent on the type of radiation. As described in section 2.1.1.1 and 2.1.1.2, the electromagnetic and particle radiation deposit energy in tissue differently. Ionizing radiation can be categorized according to the density of ionizations produced along their track (Podgorsak, 2010). The two categories are:

1. Low LET radiation (or sparsely ionizing radiation)
2. High LET radiation (or densely ionizing radiation)

The limit between the low LET and high LET radiation is often set to 10 keV/μm. X-rays are described as sparsely ionizing, where 250 keV x-rays have a LET of 2 keV/μm. Protons are referred to as densely ionizing, where 2MeV protons have a LET of 17 keV/μm.

2.1.1.5 Depth dose curves

When comparing the two different types of radiation, it is insightful to compare their depth-dose profiles. As discussed in 2.1.1.4, photons and protons deposit energy in the tissue very differently, due to how they interact with the atoms in the tissue and their respective LET values.

The depth-dose curve for a type of radiation is dependent on the charge, mass, and energy of the radiation (Podgorsak, 2010). Photons, that have no mass nor charge, will deposit most of its energy in the beginning of the material it interacts with (Podgorsak, 2010). Heavy charged particles, like protons, will travel further into the material, and deposit most of its energy by the end of its track, as described in 2.1.1.3. The depth-dose curves for charged particles can also be manipulated. By varying the energy of the proton beam, the Bragg peak can be spread out to cover a larger area. This is especially beneficial for covering the whole tumor volume in proton therapy (Tian et al., 2018). The depth dose curves for photons and protons, including a spread-out Bragg peak, are shown in Figure 6.

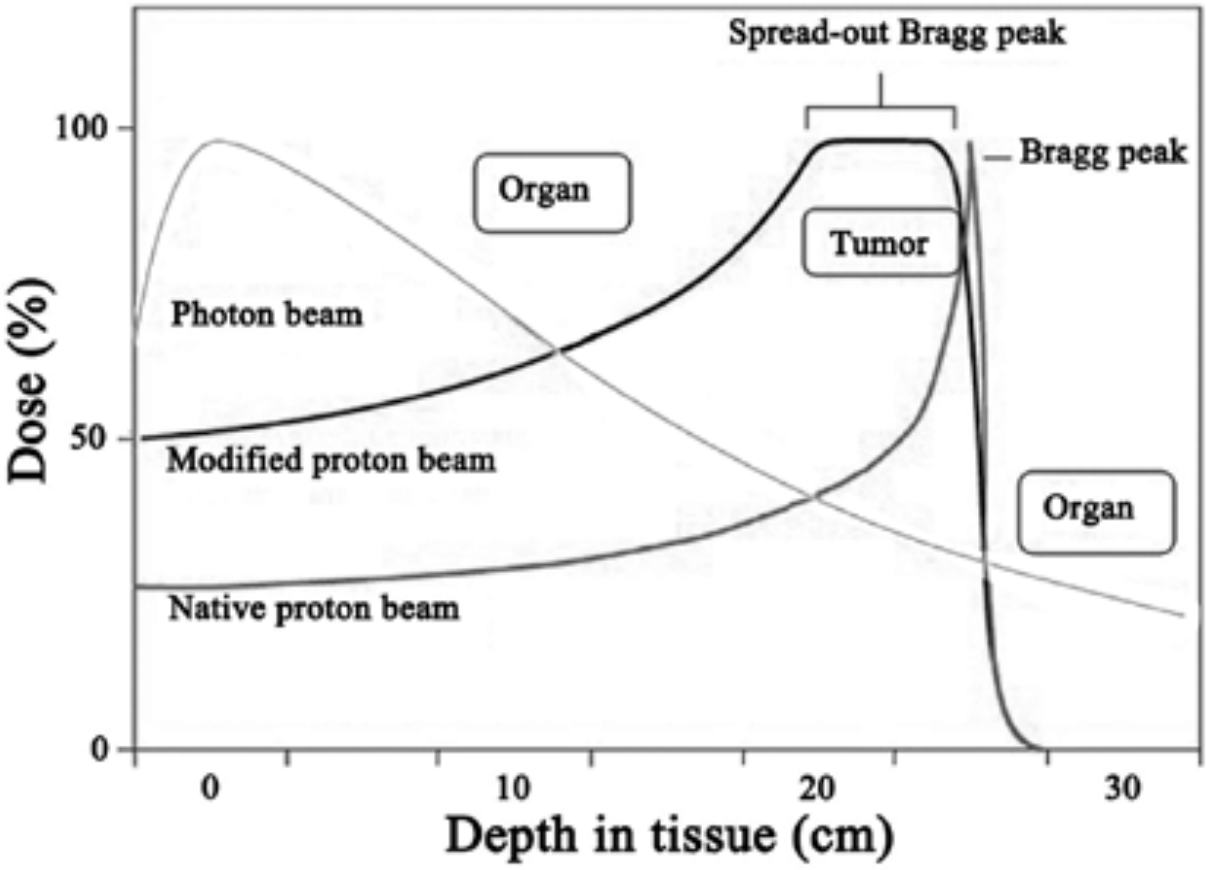

Figure 6: The depth dose curves for photons and protons. The photons deposit most of the dose in the surface of the tissue and a lower percentage deeper in the tissue. The protons deposit a low percentage of its dose in the beginning of the tissue and the biggest percentage of its dose by the end of its track, in the form of the characteristic Bragg peak. The proton beam can also be modulated by using beams with different energies to create a spread-out Bragg peak to cover a bigger volume. Figure borrowed from: The evolution of proton beam therapy: Current and future status (Review) (Tian et al., 2018).

2.1.1.6 Producing radiation

The following subsection is based on chapter 14 in Radiation Physics for Medical Physicists (Podgorsak, 2010).

X-rays

X-rays are produced in an x-ray vacuum tube, with the help of electrons. It is important that there is a vacuum inside the tube, to avoid collisions of electrons with other molecules in the air. The tube consists of an anode and a cathode, with a high voltage applied over the tube. When heated, the cathode starts to emit electrons. The electrons are accelerated towards the anode and Bremsstrahlung x-rays are produced through Coulomb interactions (2.1.1.2) with the atoms in the anode. A schematic representation of an x-ray tube is shown in Figure 7.

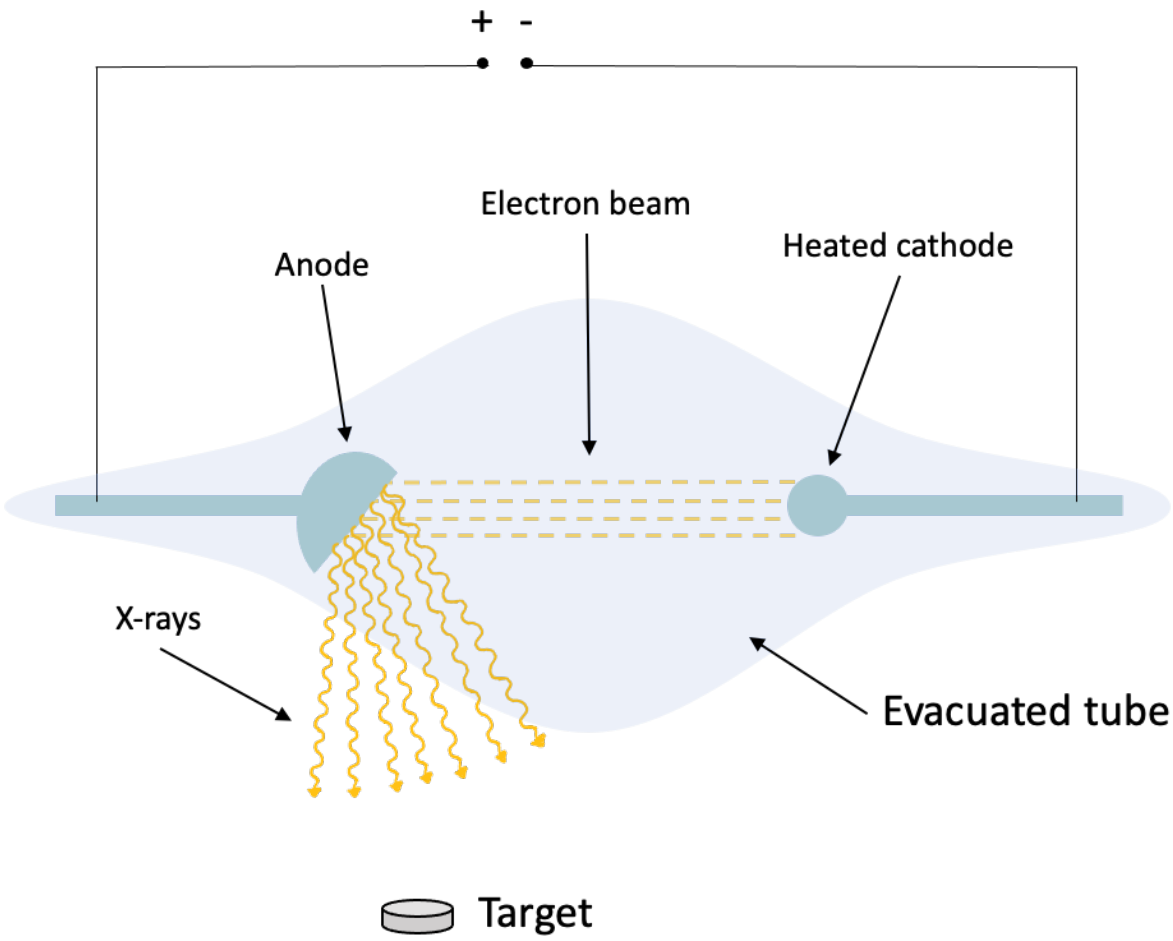

Figure 7: X-ray tube. The cathode is heated up and emits electrons. The electrons are accelerated towards the anode, by the voltage applied over the tube. The electrons interact with the atoms in the high Z-material in the anode and produce bremsstrahlung x-rays that travels towards the target.

When using an x-ray tube, there are two values that affect the x-rays produced. The first is the tube voltage. The voltage makes the negatively charged electrons accelerate from the negative side (cathode) to the positive side (anode). The higher the voltage, the higher the kinetic energy of the electrons. The kinetic energy of the electrons determines the energy spectrum of the emitted x-rays, as different fractions of the kinetic energy of the electrons are transferred to the x-rays produced. Thus, the maximum energy of the x-ray is given by the tube voltage and the average energy is around one third of this value. The second value is the tube current. The tube current determines the number of electrons being accelerated between the anode and cathode. An electrical current is responsible for heating the cathode, and increasing the current makes the temperature of the anode increase. This results in a higher number of emitted electrons. In summary, the tube voltage decides the energy of the x-rays and the tube current decides the quantity of x-rays.

Protons

A cyclotron is used to accelerate protons up to the desired kinetic energies. This is a type of circular accelerator that utilizes the charge of the particle to increase its velocity. It consists of two half cylindrical electrodes with a vacuum between them. These fill up the circular accelerator as two half circles and are called ‘Ds’ or dees due to their shape. Inside the dees there is no electric field, but there is an alternating electric field between the dees. This is illustrated in Figure 8.

The process starts by producing protons from an ion source into the center of the cyclotron. Then protons are guided in a semi-circular orbit by the magnetic field B. When the protons reach the edge of the dee, an electric field in the direction of the motion is applied and the protons are accelerated when crossing the gap between the two dees. The proton has now gained a bit more energy and will move through the next dee in a semicircular trajectory with a bigger radius. The proton gains a little more kinetic energy each time it passes over the gap. This is repeated until the proton has gained the desired kinetic energy, or the trajectory has the same radius as the dees.

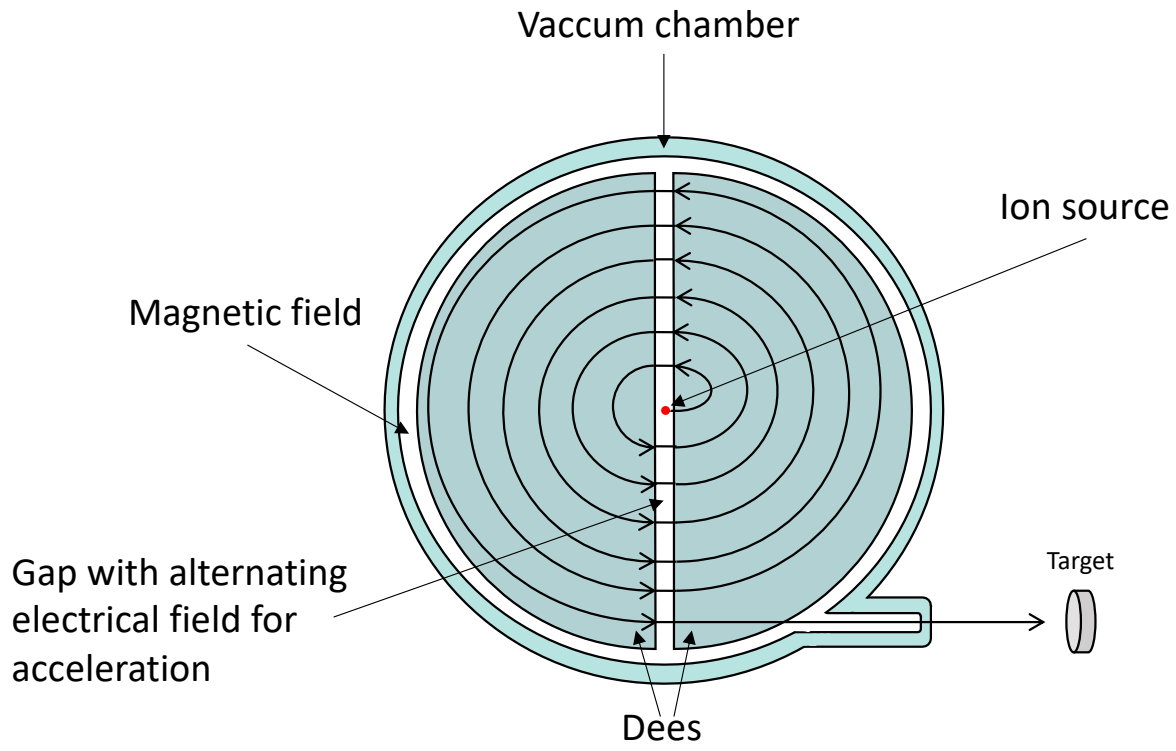

Figure 8: The protons are produced in the center of the cyclotron from an ion source. Then they are guided into the dee on the right, with the help of the magnetic field. The magnetic field guides the proton in a semi-circle before it exits the dee. Here an electrical field in the direction of the motion will accelerate the protons into the dee to the left. This increases the kinetic energy of the proton, and it will travel through the dee in an orbit with a higher radius. This is repeated until the kinetic energy of the proton is sufficient. Then the protons are guided outside the cyclotron, towards the target.

The force F needed to keep the particle in a circular orbit is equal to the centrifugal force given in equation 5.

$$F = qvB = \frac{mv^2}{r} \tag{5}$$

Where q is the charge of the particle, v is the velocity of the particle, B is the magnetic field, m is the mass of the particle and r is the radius of the particles orbit during one revolution. When equation is solved for $\omega = \frac{v}{r}$, and for r, it results in equation 6 and 7.

$$\omega = \frac{qB}{m} = 2\pi f = \frac{2\,\pi}{T} = \omega_{cyc} \tag{6}$$

$$r = \frac{mv}{qB} = \frac{p}{qB} = \frac{\sqrt{2mE_K}}{qB} \tag{7}$$

Where p is the particle momentum, f is the frequency of the orbit and E_K is its kinetic energy. The ω_{cyc} denotes the cyclotron frequency of the charged particle. Equation 6 shows that the frequency is not dependent on the velocity of the particle in a constant magnetic

field. Equation 5 shows that the radius is dependent on the velocity. Thus, slow particles move in orbits with a small radius, and fast particles move in orbits with bigger radius, but all the orbits need to finish their revolution within the same period T inside the magnetic field.

The kinetic energy of the accelerated particle is dependent on the radius of the dees, R. The velocity of the particle during the last acceleration is given in equation 8.

$$v = \frac{qBR}{m} \tag{8}$$

Using this velocity in equation 7, the final kinetic energy of the charged particle is given in equation 9.

$$E_K = \frac{mv^2}{2} = \frac{q^2B^2R^2}{2m} \tag{9}$$

2.1.2 Dose

The absorbed dose D is defined as the energy absorbed per unit mass of a material (Podgorsak, 2010), and can be written in terms of the energy imparted ϵ (Attix, 1986). This is a related stochastic quantity since the energy imparted is subject to uncertainty and random variation of radiation interactions (Attix, 1986). The energy imparted ϵ by ionizing radiation to a material with mass m in a finite volume V is defined in equation 10.

$$\epsilon = (R_{in})_u - (R_{out})_u + (R_{in})_c - (R_{out})_c + \Sigma Q \tag{10}$$

Where $(R_{in})_u$ is defined as the radiant energy of uncharged particles entering the volume V, $(R_{out})_u$ is the radiant energy of uncharged radiation leaving the volume V, $(R_{in})_c$ is the radiant energy of the charged particles entering the volume V, $(R_{out})_c$ is the radiant energy of the charged particles leaving the volume V, and ΣQ is the total energy obtained in the volume from the interactions (Attix, 1986). Using this value, the absorbed dose D can be defined as equation 11.

$$D = \frac{d\epsilon}{dm} \tag{11}$$

The dose is given in the SI unit gray (Gy) and is defined as 1 Joule of energy absorbed per kg of material (Podgorsak, 2010).

2.2 Dosimetry

The following section and subsection about dosimeters are based on Introduction to Radiological Physics and Radiation Dosimetry (Attix, 1986)

Dosimetry is used to measure the absorbed dose in matter after the interaction with ionizing radiation. To measure and calculate the dosimetry, dosimeters are used. These are devices that can measure the absorbed dose deposited in a volume by the ionizing radiation. In this thesis, an ionization chamber was used to verify the doses given. This is the most used dosimeter for precise measurements.

2.2.1 Ionization chambers

One of the most common types of ionization dosimeters are the free air dosimeters. They typically consist of a sensitive volume of air, with an inner and outer electrode. A high voltage is applied over the electrodes. When this chamber is exposed to radiation, the molecules in the sensitive volume will be ionized. Due to the high voltage over the electrodes, liberated electrons will migrate towards the positive electrode, and a current is induced. The number of charges registered is proportional to the dose and is counted by a connected electrometer.

2.3 Radiobiology

Radiobiology is defined as the study of the effect that ionizing radiation has on living things (Hall & Giaccia, 2019). To better understand this effect and its consequences, this subsection will start with a short overview of the mammalian cell division and proliferation.

2.3.1 The mammalian cell

The following section about the mammalian cell is based on Molecular Biology of the Cell (Alberts, 2014) and Radiobiology for the Radiologist (Hall & Giaccia, 2019)

Characteristic for the eukaryotic cells, mammalian cells contain a nucleus, which is a membrane enclosed compartment containing the cells' most important molecule, DNA. The backbone of the DNA strands is composed of alternating sugar and phosphate groups with attached nitrogen-containing bases. There are four different alternatives for these bases; thymine (T), cytosine (C), adenine (A), and guanine (G) (Figure 9). The four bases bind intermolecularly through hydrogen bonds; A binds to T through double hydrogen bonds, while C binds to G through three hydrogen bonds, making their pairing specific (Figure 9A, Figure 9B). The hydrogen bonds stabilize the DNA strands to form a double helix (Figure 9C). The exception to this is during transcription of the DNA, when G will bind to an uracil (U) instead of a T. Due to the weak hydrogen bonds, the double helix can easily be separated for transcription and duplication.

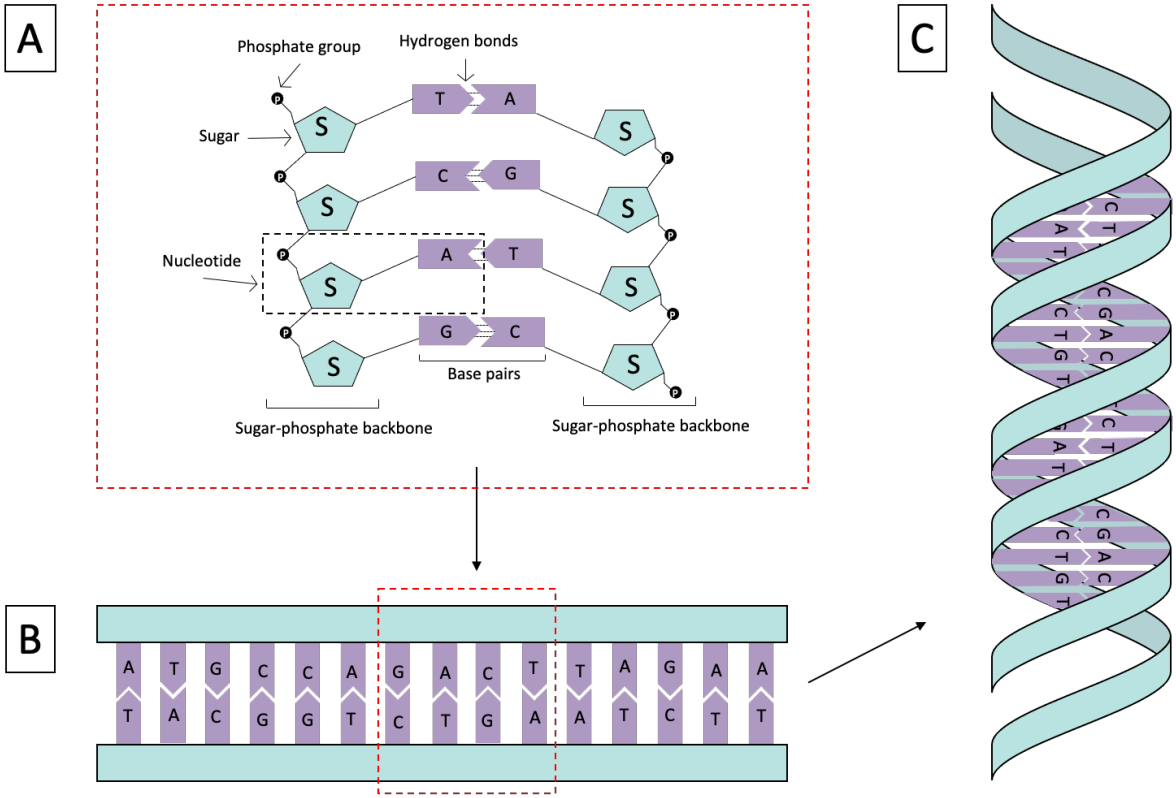

Figure 9: An illustration of how DNA is built up. A: The backbone of DNA is made up of sugar and phosphate groups, that are connected with bases. The bases bind specifically in pairs through hydrogen bonds, either two (A-T) or three bonds (G-C). A phosphate group, sugar and base make up a nucleotide. B: The DNA strand straightened out. C: The DNA in its correct form of a double helix. The figure is adapted from figure 4-3 and figure 4-4 in (Alberts, 2014).

Each DNA segment represents one gene, and each gene corresponds to a protein, a variant of a protein or an RNA molecule. Transcription is the process where the information from DNA is used as a template for making ribonucleic acid (RNA). These RNA strands are transported from the nucleus to the cytoplasm, where they are converted into proteins through translation. The synthesis of proteins is regulated by the cells, by adjusting the rate of translation and transcription of the different genes.

During cell division, the DNA is tightly coiled up in chromosome pairs, 23 pairs in human cells. Different proteins are involved in compressing the DNA that coils and folds the DNA into different levels of organization. The first level of organization is the DNA double helix, that is wrapped around the protein histones, creating a nucleosome. These are tightly packed together and folded into loops called chromatin fibers, that make up the chromosomes. An illustration of the different chromosome levels is represented in Figure 10.

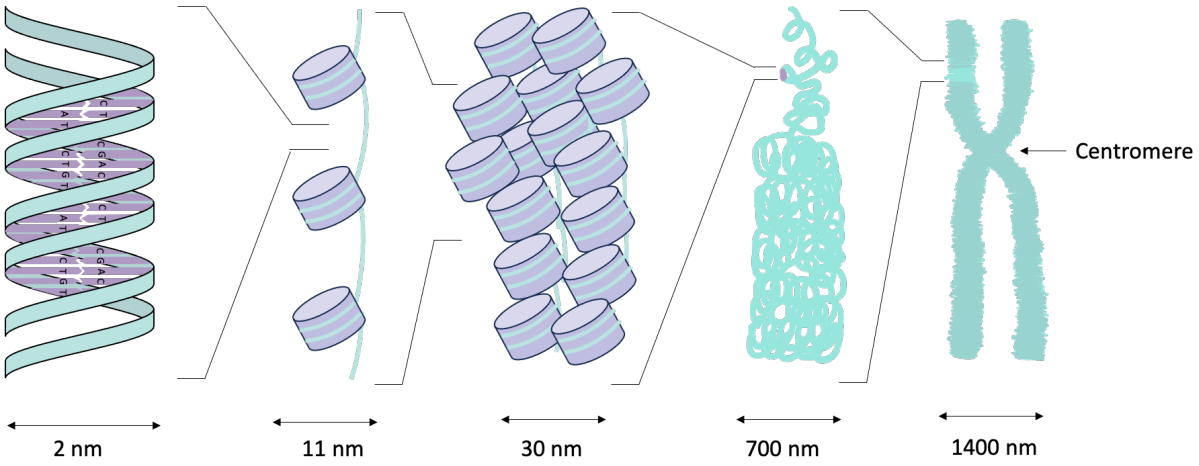

Figure 10: From DNA to Chromosome. The illustration shows some of the levels on how the DNA is packed to make up the chromosome, and the approximate sizes of each level. On the lowest level, it is the DNA double helix. The DNA is packed around a histone, making a nucleosome. These nucleosomes are tightly packed together to make chromatin fibers, that are folded into loops that make up the entire chromosome. The center of the chromosome is called the centromere. The figure is adapted from figure 4-61 (Alberts, 2014).

The cell cycle

Before a cell proliferates, it goes through a sequence of events to prepare it for cell division known as the cell cycle. This cycle is divided into 4 main phases: Gap phase 1 (G_1), S phase, Gap phase 2 (G_2) and M phase, that are controlled by a system of regulatory proteins. The three first phases are collectively known as interphase. Cell division requires the cell to copy and duplicate its entire DNA, which will happen during the two gap phases. There are checkpoints at the end of the two gap phases and in the middle of M phase, to ensure cell viability and suitable conditions to continue the cell cycle. In the G_1 phase, there is a specialized resting state, G_0, that the cells can remain in for up to years if the conditions are not suitable before continuing proliferation. When conditions become favorable and the cells are stimulated to start growing and dividing, the cells progress through the G_1 phase until the first checkpoint. Passed this point the cell enters the S-phase, where it has committed to start DNA replication and the chromosomes are duplicated, one for each of the daughter cells. The cell proceeds to G_2 phase, with a checkpoint to control that the DNA was correctly duplicated. The last phase of the cell cycle is the M-phase which consists of two parts, mitosis and cytokinesis. During mitosis the duplicated chromosomes are divided to each side of the cell by microtubules connecting to the center of the chromosomes (centromeres). Following this, the cell is then divided into two daughter cells through cytokinesis. Separating these two events is a checkpoint ensuring correct separation of the chromosomes. An illustration of the cell cycle is shown in Figure 11.

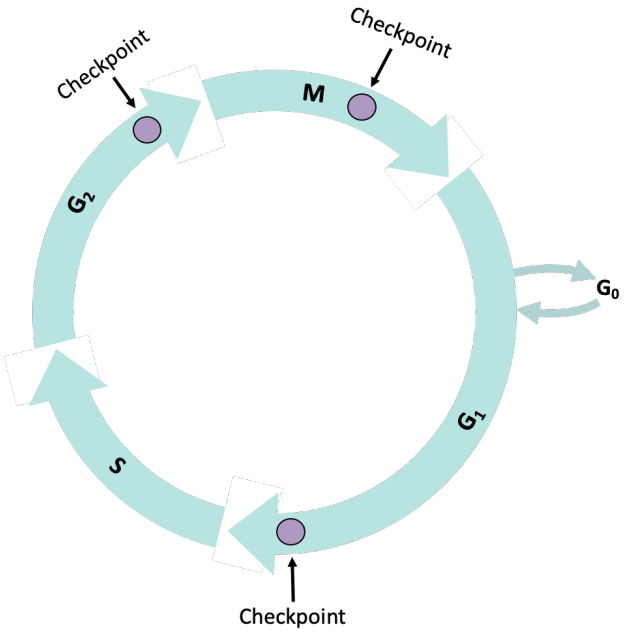

Figure 11: An overview of a typical cell cycle to a eukaryote cell. To proceed to the S-phase through the checkpoint, the conditions must be favorable, and the cell needs stimuli to start growing and dividing. In S-phase the DNA is duplicated before going into G_2. To proceed to M-phase, all the DNA must be duplicated, and the environment must be favorable to get through the checkpoint in G_2. In M-phase the duplicated DNA *is pulled to each side, and when this is confirmed in the last checkpoint, the cell proceeds to cytokinesis. The figure is adapted from figure 17-9 (Alberts, 2014).*

If an issue is detected during any of the checkpoints, the cell cycle will be paused until the issue is either resolved or if this is not possible, go through apoptosis.

Mutations

During DNA replication or repair, errors can occur that alter the nucleotide base sequence, known as mutations. There can be different outcomes of the mutations depending on the localization in the genome and type of mutation. In many cases, these mutations will cause no significant difference for the cell, as ~98.5% of the human genome does not code for proteins. A mutation may occasionally be beneficial for the cell and can cause an increased likelihood for reproduction. If the mutation occurs in genes that code for proteins which are crucial for the function of the cell, it can have big consequences for the following generation. These consequences are discussed in 2.4.

2.3.2 Radiation damage

The following sections are based on Radiobiology for the Radiologist (Hall & Giaccia, 2019).

When biological matter is exposed to ionizing radiation, it can cause either a direct or indirect effect to the critical cellular targets. Direct effects occur when radiation is absorbed through ionization and excitation, potentially causing biological damage. This process is dominant for radiation with higher LET. On the other hand, indirect effects occur when ionizing radiation interacts with atoms or molecules within the cellular environment.

This interaction can make the atoms or molecules become highly active free radicals, characterized by having unpaired electrons. These free radicals have the potential to diffuse over to the target, cause damage and potentially disrupt normal cellular function.

DNA as target

The most radiosensitive part of the cell is the DNA, often referred to as the target of the cell. As discussed in the previous section on DNA and its role in cellular function (2.3.1), the DNA contains the genetic recipe, in the form of the base-sequence. This is necessary for creating the proteins that are essential for cell function (Alberts, 2014). Therefore, any changes in the base sequence of the DNA can have fatal consequences for the cell.

Ionizing radiation can induce various types of DNA lesions, that will be discussed in more depth in section 2.3.3. While the cell can repair most of these lesions, some damages are too complex and can lead to cell death. The cell's response to DNA damage depends on multiple factors, including the dose and type of ionizing radiation, the specific type of DNA injury, the current cell cycle phase, and the reliability of the DNA damage repair (Rodríguez-Ruiz et al., 2018)

2.3.3 Damage in mammalian cells

The following sections are based on Radiobiology for the Radiologist (Hall & Giaccia, 2019).

The complexity of the damage resulting from ionizing radiation depends on the dose and the LET of the radiation (Rodriguez-Ruiz et al., 2020). Radiation damage to mammalian cells can be classified into three types.

1. **Lethal damage** is irreversible damage and cannot be repaired by the cellular repair mechanisms, ultimately leading to cell death
2. **Potentially lethal damage** has the potential to cause cell death if left untreated. This type of damage will not be immediately fatal but can progress to lethal damage if not sufficiently repaired
3. **Sublethal damage** is easily repaired by the cellular repair mechanisms. However, if another sublethal damage occurs in proximity, it can become cumulative and create a lethal damage

2.3.3.1 Damage on DNA level

The DNA sustains different types of damage from ionizing radiation, including double strand breaks (DSB) and single strand breaks (SSB). While additional types of damage exist, they fall outside the scope of this thesis and will not be discussed further.

A single strand break occurs when only one of the DNA strands is damaged. SSBs have a low chance of causing critical biological damage, as they are easily repaired by the cellular repair mechanism. The intact complementary DNA strand acts as a template, allowing the repair mechanism to accurately restore the damaged DNA strand.

The most significant damage in terms of biological damage are the double strand breaks. When both DNA strands are damaged, the repair process becomes more challenging and less accurate, increasing the risk of genomic instability. The complexity of the DSB repair depends on the physical characteristics of the break and the cell cycle phase. DSBs can lead to damage on a chromosomal scale, potentially causing problems during mitosis and eventually lead to cell death.

2.3.3.2 Damage on Chromosome level

When double strand breaks occur in the DNA, they can have significant consequences on the chromosome level, which become visible after the following mitosis. The broken ends of the DNA become sticky due to unpaired bases, and the way these sticky ends are rearranged determines the severity of the damage. There are three potential outcomes after DSBs:

1. The sticky ends can rejoin in the same position as before the DSB occurred. Apart from the loss of bases, this outcome does not lead to any severe consequences during mitosis
2. In some cases, the sticky ends may not rejoin at all, resulting in an aberration in the chromosome. Even though the cell progresses through mitosis, it becomes marked for deletion at the subsequent mitosis
3. Lastly, the sticky ends may rejoin with other sticky ends, and produce distorted chromosomes after mitosis. Specific examples of these situations are described below

There are two classes of aberrations that are observed at metaphase (a step in mitosis where the chromosomes are aligned in the middle of the cell): chromosome aberrations and chromatid aberrations. Chromosome aberrations occur when the damage occurs in early interphase, before the chromosome material has been duplicated, resulting in the same damage on both chromatin strands after duplication in S-phase. Chromatin aberrations, on the other hand, occur when the break happens in late interphase, after the chromosome has been replicated. Then the damage will not be identical across the two chromatin strands.

Chromosome aberrations

The formation of a dicentric and a ring are two chromosome aberrations that are lethal to the cell. The formation of a dicentric can occur when there are breaks in two separate chromosomes in proximity during in early interphase. The sticky ends will then rejoin and be replicated during S-phase. After DNA replication, the chromosome will have two centromeres, forming a dicentric chromosome, with two loose fragments (Figure 12A). These two fragments will likely be lost during mitosis, due to the lack of centromeres.

The second lethal chromosome aberration is the formation of a ring, which happens when there is a break in each arm of the same chromosome, early in the cell cycle. The sticky ends may then rejoin and form one ring and a fragment. After replication during S-phase, the fragment is doubled, resulting in two overlapping rings (Figure 12B). The loose fragments are most likely lost during mitosis, due to the loss of centromeres.

Chromatid aberration

An anaphase bridge is an example of a lethal chromatid aberration. This type of aberration occurs after the chromatids have been duplicated. A radiation-induced break can then happen in both chromatids of one chromosome. The sticky ends can rejoin to form a sister union, preventing cell division, since each centromere in the joined chromosome will stretch out across the cell (Figure 12C).

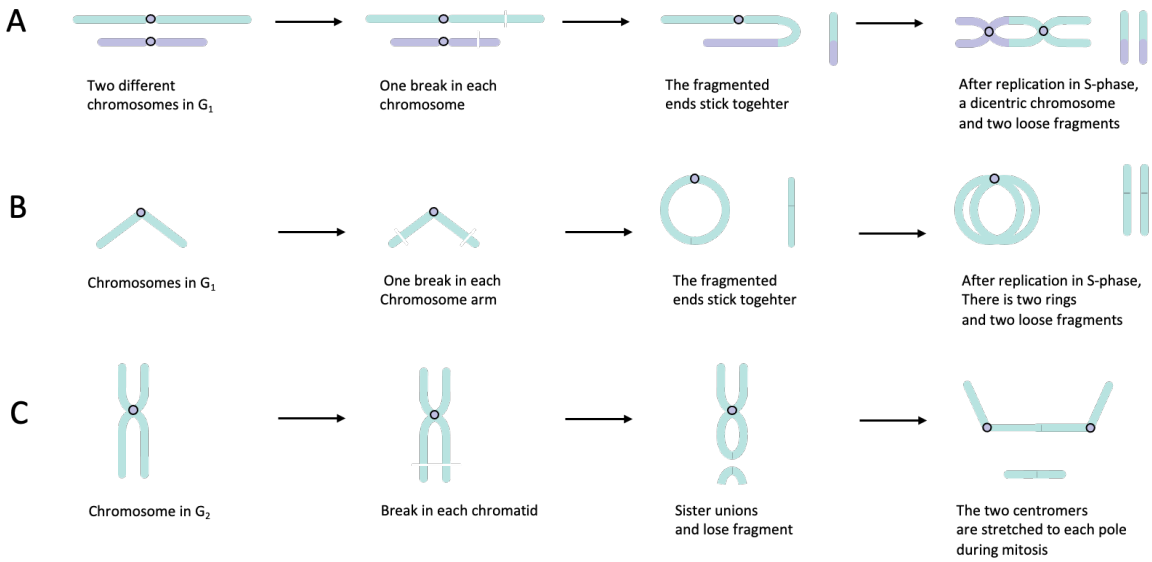

Figure 12: ***A:*** *Formation of a dicentric starts with irradiation induced breaks in two different chromosomes in G_1. The sticky ends rejoin, resulting in an interchange between the two chromosomes. After DNA replication, the chromosome will have two centromeres, forming a dicentric chromosome. The loose fragment will also be replicated and lost at the subsequent mitosis due to the lack of centromeres.* ***B:*** *Formation of a ring chromosome starts with an irradiation-induced break in each arm of the same chromosome. The sticky ends will rejoin and form a ring and a loose fragment. After DNA replication, there are two overlapping rings and a loose fragment, that are likely lost during mitosis due to the loss of centromeres.* ***C:*** *Anaphase bridge formation occurs when there is a break in each chromatid of the chromosome during G_2. The incorrect rejoining of the sticky ends creates a sister union and a loose fragment. At mitosis the centromeres will be stretched to each pole, and the separation of the cell will not be possible. The figure is adapted from figure 2.14 (Hall & Giaccia, 2019).*

After each of the three possible aberrations described in Figure 12, loose fragments are produced. These fragments are lost during mitosis since they lack centromeres to anchor them to one of the daughter cells. Consequently, large portions of the DNA sequences are lost, which could potentially be essential genes critical for cellular function.

2.3.4 Repair

The following section about the repair mechanism in mammalian cells is based on Radiobiology for the Radiologist (Hall & Giaccia, 2019) and The Molecular Biology of the Cell (Alberts, 2014).

Radiation damage to DNA initiates different repair mechanisms depending on the type of damage produced and the current stage of the cell cycle. Among the four main phases of the cell cycle, beginning of S phase, where the DNA is replicated, and M phase, where the cell is divided, are particularly sensitive to radiation-induced damage.

Repair of Single Strand Breaks

Two main pathways are involved in repairing single strand breaks: base excision repair and nucleotide excision repair. Base excision repair, target damage in one or multiple nucleotides by first removing the damaged or incorrect base(s). Then the complementary base on the opposite strand is read, and the correct base is placed and ligated to the damaged DNA strand. Nucleotide excision repair targets DNA lesions resulting from UV-radiation. It begins with identification and removal of the DNA lesion, followed by the use of the opposite strand as a template to synthesize the missing part of the strand, which is then ligated with DNA ligase onto the damaged DNA strand.

Repair of Double Strand Breaks

Double strand breaks in DNA are primarily repaired through two pathways: homologous recombination repair (HRR) and nonhomologous end joining (NHEJ). HRR performs near error-free repair by using the other intact sister chromosome as a template. Consequently, HRR is performed in late S or G_2 phase when an undamaged chromosome is available. In contrast, NHEJ is a more error-prone repair pathway compared to HRR. It repairs damage in the G_1 phase of the cell cycle when there is no intact sister chromosome to serve as a template. NHEJ begins by processing the broken ends of the DNA, before the ends are brought together and ligated with DNA ligase. This repair process often results in the loss of base sequences.

Defects in these repair pathways can lead to increased genomic instability and a higher risk of cancer (Rodríguez-Ruiz et al., 2018). Carcinogenesis (the formation of cancer cells) can occur when multiple mutations affect crucial regions of the DNA that are essential for cell proliferation and repair. These implications are discussed further in 2.4.

2.3.5 Cell death mechanisms

The following section about the cell death mechanisms is based on Radiobiology for the Radiologist (Hall & Giaccia, 2019) and The Molecular Biology of the Cell (Alberts, 2014).

The most severe damages mentioned in section 2.3.3 are irreparable and will lead to cell death. Several cellular mechanisms ensure that damaged or infected cells undergo cell death.

Apoptosis

Apoptosis, also known as programmed cell death, follows a sequence of molecular events that lead to the cell's self-destruction. This process begins with the cell stopping communication with its neighbors, resulting in the cell rounding up and detaching from its neighbors. The cell will eventually shrink due to water loss and protein crosslinking. The dying cell then fragments into several membrane-bound fragments. During apoptosis, the cell's surface chemistry changes, signaling to neighboring cells or macrophages to engulf the fragments.

Autophagic cell death

Autophagic cell death is a self-digestive process that degrades proteins and organelles, serving as a protective mechanism for cells to survive and generate nutrients and energy.

Necrosis

Necrosis occurs in response to acute trauma. Cells undergoing necrosis swell and burst, releasing their contents, and triggering an inflammatory response.

Mitotic cell death

Following ionizing radiation, mitotic cell death becomes the dominant mechanism for cell death. Mitotic cell death occurs when cells attempt to divide but die due to chromosomal or chromatid aberrations (2.3.3). This can happen either during the first or the second division after radiation.

Senescence

Cellular senescence occurs in response to the accumulation of damage in the cell. Senescence leads to an irreversible cell cycle arrest due to activation of proteins that silence genes necessary for the transition from G_1 to S phase. This will stop the cell proliferation and is considered as a cell death mechanism for cancer cells. Thus, senescence acts as a tumor suppressor mechanism, hindering excessive cellular divisions in response to excessive growth signals arising from cells with accumulated DNA damage.

Numerous types of cell death mechanisms exist beyond those mentioned in this section. One such mechanism is immunological cell death, which is associated with the immune response and induced due to damage-associated molecule pattern (DAMPs) released by the cells after irradiation (Rodríguez-Ruiz et al., 2018). This specific cell death mechanism is of special interest in this thesis and will be described in more depth in section 2.5.1.

Bystander effect

The bystander effect demonstrates that biological effects are induced in cells that are in proximity to irradiated cells but have not received direct irradiation. Studies investigating this phenomenon, suggest that irradiated cells secrete specific molecules with the potential to induce cell death in non-irradiated cells.

2.3.6 Relative Biological Effectiveness

This section and the following subsection are based on Radiobiology for the Radiologist (Hall & Giaccia, 2019).

The relative biological effectiveness (RBE) describes the biological effect of a dose compared to photon radiation, which serves as the standard. RBE is the ratio between the dose of test radiation and the dose of photon radiation, where both doses produce the same biological effect.

The biological effect of a dose is dependent on the Linear Energy Transferred (2.1.1.4) of the chosen radiation. When the LET increases, the radiation produces a higher ionization density and leads to more closely spaced ionizing events. As the LET of the radiation increases, the ability to produce biological damage also increases (Podgorsak, 2010). The RBE reaches its maximum at an optimal LET of 100 keV/μm, corresponding to an average separation of 2nm between ionizing events, which aligns with the diameter of the DNA double helix. This ionization density gives the highest probability of double strand breaks, which are crucial for biological damage. Radiation with higher LET, will have average ionizing events closer together than 2 nm. Although this also produces DSBs, the energy is wasted as the ionizing events are too close and do not produce additional damage. Consequently, for LET above 100 keV/μm, the RBE decreases. The RBE as a function of LET, and corresponding ionization density compared to the size of DNA, is shown in Figure 13.

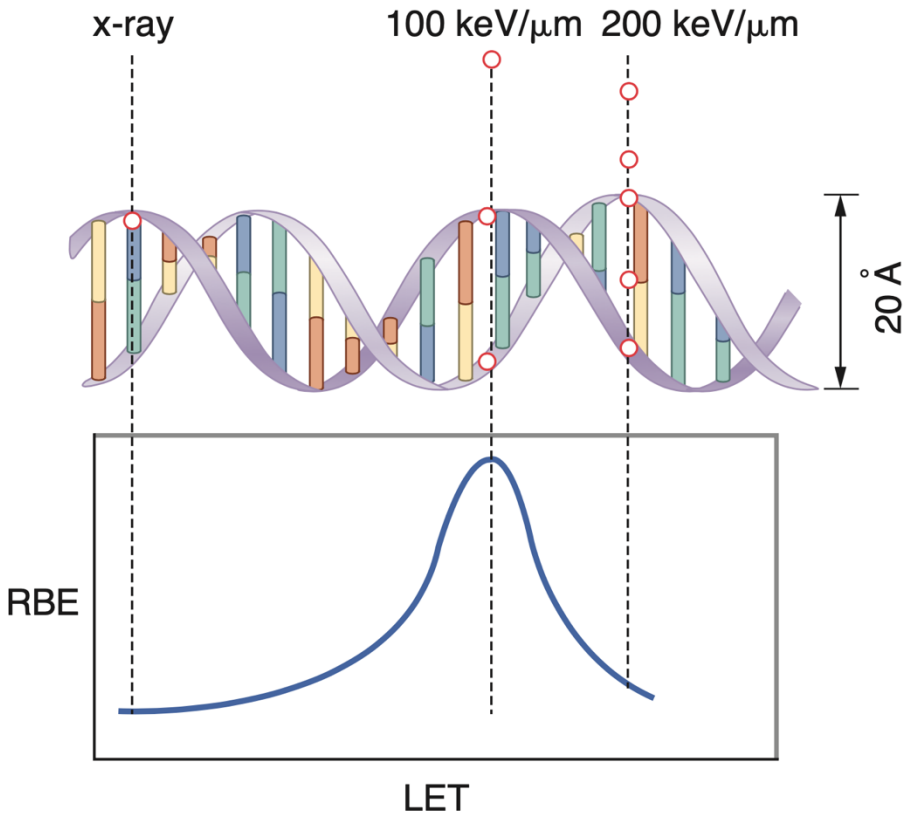

Figure 13: The RBE as a function of LET, with the corresponding average distance between ionization events compared to the size of the DNA. The optimal RBE is at a LET of 100 keV/μm, since this type of radiation has an average distance of ionizing events at 2 nm (20 Ångstrøm). This coincides with the diameter of the DNA double helix and gives a higher probability of double strand breaks and therefore a higher biological effect. Figure is borrowed from Radiobiology for the radiobiologist (Hall & Giaccia, 2019).

Other factors that impact the RBE include the dose, dose rate, type of target cell/tissue, number of dose fractions, and chosen end point. When the total dose is delivered in smaller fractions over a period, the RBE is higher compared to when the same dose is given as a single dose. This occurs because the cells have time to repopulate and repair sublethal damage.

2.3.6.1 Fractionated Radiation

When the radiation dose is delivered in multiple equal fractions, with sufficient time in between each fraction for the repair of sublethal damage (2.3.3), it results in higher cell survival rates. Fractionation can be divided into two different strategies: hypofractionation and hyperfractionation. Hypofractionation delivers higher doses in fewer fractions and hyper fractionation delivers smaller doses in many fractions. The effective dose survival curve, where the logarithm of the survival is plotted against the dose, exhibits a characteristic shape known as ‘shoulders’, presented in Figure 14.

When comparing curve A, which represents a single high dose, and curve B, representing an ideal fractionation scheme, curve B shows a higher surviving fraction for the same total dose. The fractionation scheme introduces a shoulder for each fraction, indicating the proliferation due to damage repair, and this shoulder is repeated multiple times. As a result, the overall cell survival fraction is higher in the fractionation scheme, leading to an increased RBE.

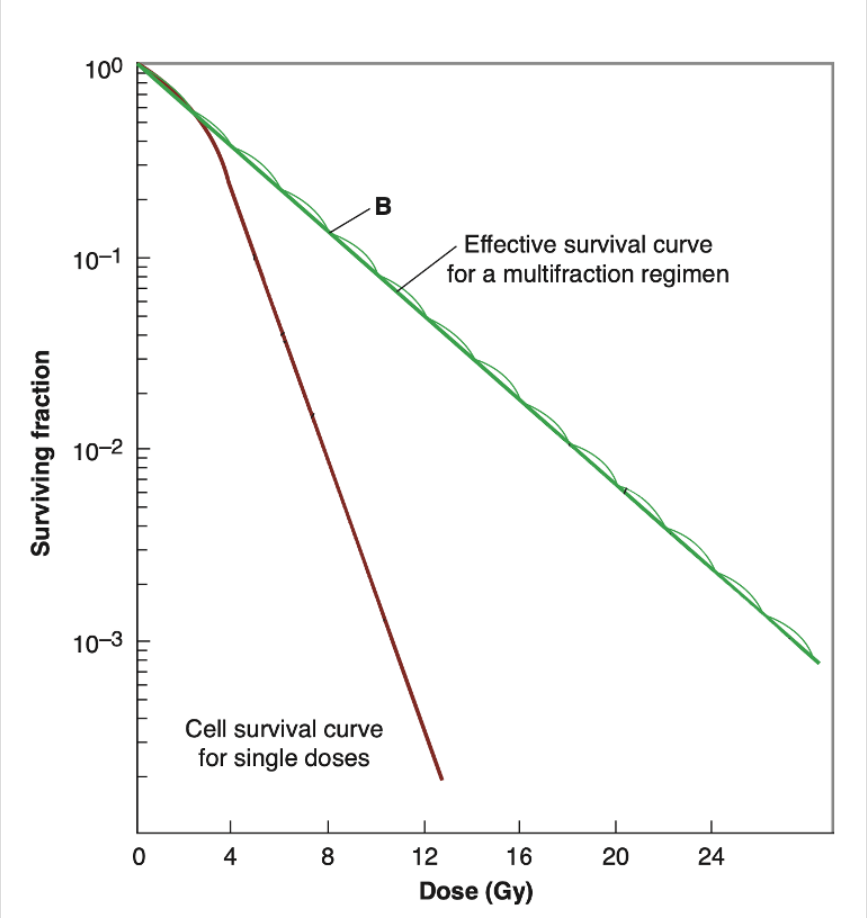

Figure 14: A comparison between the survival curve of a single high dose (A) and the survival curve for a multi-fraction scheme (B). The fractionation scheme, with multiple equal fractions of radiation and time in between for sublethal damage repair, shows repeated shoulders in the curve leading to a higher overall survival fraction. The figure is modified and borrowed from (Hall & Giaccia, 2019).

This shoulder effect is more pronounced in normal tissue compared to tumor tissue. Consequently, a greater survival rate is observed in normal tissue in comparison to tumor tissue, effectively leading to a protective effect for the healthy tissue while still getting an effect in the tumor.

In summary, fractionated radiation, with sufficient time intervals for cellular repair between each fraction, leads to a shoulder effect in the effective dose survival curve, that is more prominent for healthy tissue compared to tumor tissue, resulting in enhanced cell survival compared to a single high dose. This phenomenon contributes to an increased RBE in the fractionation scheme.

2.4 Cancer cells

The following sections about cancer cells is based on the book The Immune System (Parham, 2021)

The human body depends on cell division to grow, repair damaged tissue, and protect itself from foreign pathogens. It is estimated that approximately in the order of 10^{16} cell divisions occur during a lifetime. To maintain normal cell proliferation in the tissue, it is crucial that the mechanisms for cell division and apoptosis are in place. These control mechanisms are regulated by three groups of genes: proto-oncogenes, tumor suppressor genes and DNA stability genes. Proto-oncogenes act as growth regulators, tumor suppressor genes act as negative growth regulators, and DNA stability genes are involved in monitoring and maintaining the integrity of the DNA.

Despite these mechanisms being in place, errors can occur, resulting in deviations from the original base sequence, known as mutations (covered in 2.3.1). If multiple mutations occur in genes that play a critical role in cell division and survival, the cell can start to proliferate uncontrollably, and in the worst case, disrupt the body's physiology and organ function. This disease is collectively called cancer, and when it spreads to other parts of the body, it is defined as metastasis.

Cancer cells share seven characteristics that give them the ability to develop. They stimulate their own growth, ignore growth-inhibiting signals from neighboring cells, avoid apoptosis, develop a blood supply, metastasize, proliferate uncontrollably to increase their numbers, and they evade and hide from the immune system.

2.5 Immune system

The following sections about the immune system is based on the book The Immune System (Parham, 2021)

The immune system serves as the body's defense against infectious agents and is responsible for eliminating all foreign materials. This complex system consists of different cells and molecules that work together. Among these components are antibodies, which play a vital role and are produced by a subgroup of immune cells. Antibodies recognize microbial antigens and target microbes for elimination through various effector mechanisms. Over the past century, cancer immunologists have tried to engage the patient's own immune system to enhance the efficacy of the conventional therapies (Alberts, 2014).

The immune system is divided into two main mechanisms: Innate and adaptive immunity. Innate immunity serves as the initial defense against infections, while adaptive immunity develops after an infection and provides protection if the infection returns.

The innate immunity

Innate immunity is the part of the immune system that vertebrates are born with, providing an immediate response when an infection is present. This primary response consists of two parts. Firstly, it involves the detection of pathogens, which are organisms with the potential to cause an infection. This task is performed by soluble proteins called cytokines. Additionally, cell-surface receptors can bind to the pathogen or its products, as well as to the cells and serum proteins altered due to the pathogen. When a pathogen is detected, the second part of the innate immune response is initiated and responsible for the destruction and elimination of the pathogen. Effector cells are the main driving force behind this response, and accomplish this by engulfing bacteria, killing virus infected cells and attacking parasites.

The most important cells of the innate immune response and their responsibilities are as follows:

- Phagocytic cells specialize in capturing, engulfing and killing microorganisms
- Macrophages, a larger type of phagocytic cells, secrete cytokines to recruit other phagocytic cells to the infected area
- Dendritic cells have similar properties to macrophages but play a unique role in calling upon the adaptive immune response when needed
- Natural killer (NK) cells contribute to stopping the spread of the infection by eliminating virus-infected cells in the infected tissue and secrete cytokines that inhibit viral replication

The adaptive immunity

Adaptive immunity is distinct from innate immunity as it develops in response to pathogens that outrun the innate immune response. With each exposure to the same pathogen, the adaptive immunity increases in magnitude and defense capabilities primarily due to memory cells that ‘memorize’ the specific pathogen. Lymphocytes, with specific cell-surface receptors, play a crucial role in this process by recognizing and binding to the specific pathogen when an infection is present. Consequently, only these specific lymphocytes with the appropriate receptors can initiate the immune response against the pathogen involved, leading to clonal selection and clonal expansion of effector cells specifically targeting the pathogen. The main components of adaptive immunity are the small lymphocytes. These lymphocytes have several sub-lineages that can be distinguished by their cell-surface receptors and functionality. The most vital sub-lineages are B-lymphocytes (B-cells) with immunoglobulin as surface receptors, and T-lymphocytes (T-cells) with surface T-cell receptors. B-cells are specialized in producing antibodies, while T-cells play various roles, including cytotoxic, regulating and helper functions.

Any molecule, macromolecule, virus, or cell that has a structure recognized and bound by an immunoglobulin or T-cell receptor is called the corresponding antigen. When a B-cell or T-cell encounters an antigen, it differentiates into an effector cell. B-cells differentiate exclusively into effector B-cells, which secrete soluble immunoglobulins known as antibodies. Conversely, T-cells differentiate into various effector cells, including cytotoxic T-cells (CD8 T-cells) responsible for eliminating infected cells, helper T-cells (CD4 T-cells) that secrete cytokines to activate other immune cells, and regulatory T-cells. The latter controls the activities of cytotoxic T-cells to prevent unnecessary damage to the healthy tissue and halt the immune response once the pathogen has been successfully neutralized.

The adaptive response is highly specific due to small differences in the regions of the binding sites on immunoglobulins and T-cell receptors. These differences create a variety of binding sites specific for different pathogens, allowing the immune system to respond exclusively to the exact pathogen encountered.

2.5.1 Immunologic cell death

Ionizing radiation has the potential to activate an immunogenic variant of regulated cell death by engaging the immune system (Vaes et al., 2021). This form of cell death, known as immunogenic cell death, induces an immune response by releasing specific molecules collectively referred to as danger-associated molecular pattern (DAMPs) (Vaes et al., 2021). DAMPs are endogenous molecules that are produced and released by damaged and dying cells (Rodríguez-Ruiz et al., 2018). Upon release, these molecules bind to pattern recognition receptors, stimulating the immune response (Rodríguez-Ruiz et al., 2018). Dying cells can release DAMPs such as protein high-mobility-group Box 1 (HMGB1) and membrane-exposed calreticulin, which acts as a signal to promote phagocytosis by dendritic cells (Lhuillier et al., 2019). Additionally, ionizing radiation induces the release of other DAMPs, including extracellular ATP, heat shock protein 70 and 90, uric acid (Dahl et al., 2019), and micronuclei in the cytosol can cause immunological cell death through the cGAS-STING pathway.

The cGAS-STING pathway

The DNA damage caused by radiation can lead to the accumulation of micronuclei in the cytoplasm of the cell (Vaes et al., 2021). Micronuclei are membrane-enclosed chromosome fragments that are formed after cell division (Lhuillier et al., 2019). Since DNA is normally confined within the nucleus, its presence in the cytoplasm acts as a DAMP, signaling potential cellular damage through the cGAS-STING pathway (Vaes et al., 2021).

At the core of the cGAS-STING pathway is the cyclic guanosine monophosphate-adenosine monophosphate (cGAMP) synthase (cGAS), an enzyme that functions as a sensor to detect cytoplasmic DNA (Vaes et al., 2021). When cGAS identifies the micronuclei floating in the cytosol, it triggers the production of cGAMP, a critical secondary messenger (Vaes et al., 2021).

The cGAMP, in turn, activates the stimulator of interferon genes (STING) (Lhuillier et al., 2019). Once STING is activated, it initiates the production of interferon type I that can initiate an inflammatory response (Vaes et al., 2021).

Through the cGAS-STING pathway, dendritic cells are activated, and cytotoxic T-cells are primed, contributing to the immune response (Dahl et al., 2019). This cascade of events plays a crucial role in enhancing the immune system's ability to recognize and respond to cancer cells and other cellular threats triggered by ionizing radiation (Vaes et al., 2021). The cGAS-STING pathway represents an essential mechanism by which ionizing radiation-induced DNA damage can activate immunological cell death, promoting an immune response against cancer cells and contributing to more effective cancer treatments (Vaes et al., 2021).

2.5.2 Immunosuppressors

Growing evidence suggests that radiotherapy functions as a 'double-edged sword', capable of inducing both immunogenicity and immunosuppression (Donlon et al., 2021). The immunosuppressor effects can be decreased cytotoxicity of CD8 T-cells and NK cells, dysfunctional antigen-presenting cells and induction of immunosuppressive cells, which is critical for tumor growth (Jin et al., 2023).

These effects occur from a complex interplay of mechanisms, some of which are probably still undiscovered. In this thesis, two specific mechanisms are investigated. The first mechanism is the upregulation of the programmed death ligand 1 (PD-L1), and the second mechanism is the release of the inhibitory DAMP (iDAMP) PGE_2. iDAMPs counteracts the action of the DAMPs (Hayashi et al., 2020).

The PD-1/PD-L1 pathway

Programmed death ligand 1 (PD-L1) is the main ligand to the transmembrane protein programmed death 1 (PD-1). PD-1 is found on the surface of various immune cells, such as T-cells, B-cells and dendritic cells, while PD-L1 is expressed on tumor cells (Alsaab et al., 2017). The PD-1/PD-L1 pathway plays a crucial role in regulating T-cell activation during inflammatory responses to limit the risk for autoimmunity (Pardoll, 2012).

Upon recognition of the PD-L1 protein on target cells, T-cells produce inflammatory cytokines that upregulate membrane-bound PD-L1 on these cells. This upregulation enables PD-L1 to interact with PD-1 on T-cells (Alsaab et al., 2017). Consequently, the PD-1/PD-L1 pathway induces apoptosis in cytotoxic T-cells, promotes the differentiation of helper T-cells into regulatory T-cells, and impairs the activation of natural killer cells (Alsaab et al., 2017). These collective effects contribute to immune tolerance, whereby immune cells are inhibited from taking any action against the target cells (Alsaab et al., 2017).

Overexpression of PD-L1 is a mechanism the cancer cells use to protect itself from cytotoxic T-cell killing (Alsaab et al., 2017). By evading the immune system's surveillance and suppressing T-cell activity, cancer cells can evade destruction and continue to proliferate and grow as tumors.

The COX-2/PGE_2 pathway

Cyclooxygenases (COXs) are membrane bound enzymes primarily located on the nuclear membrane and endoplasmic reticulum. COX are categorized into COX-1 and COX-2 (Jin et al., 2023). COX-1 is expressed at basal levels in many cells and generates a low level of prostaglandins to maintain body homeostasis. COX-2 on the other hand, is normally absent in cells but is induced in response to stimuli like growth factors and cytokines (Finetti et al., 2020). A main product from the COX-2 activity is Prostaglandin E_2 (PGE_2), that belongs to the prostanoid family of lipids, and holds an essential role in inflammation regulation under both physiological and pathological conditions (Finetti et al., 2020).

In physiological processes, PGE_2 contributes to regulate fever, pain and inflammation. However, in pathological conditions, such as cancer, PGE_2 can enhance tumor cell proliferation and survival, and even contribute to induce metastasis (Finetti et al., 2020).

Following the synthesis of PGE_2, its activity is regulated through four transmembrane receptors, known as the EP receptors. When PGE_2 activates the EP1 receptor, intracellular calcium ion concentrations are upregulated. When activated, EP2 and EP4 receptors upregulate cAMP that will activate the PKA pathway, β-catenin pathway, NF-κB pathway and the PI3K/AKT pathway, which can promote tumor growth. When PGE_2 binds to the EP3 receptor, the cAMP levels are downregulated. This is illustrated in Figure 15. The communication and response to PGE_2 are dependent on the cell type, tissue and location. These responses may vary in cancer cells, which can influence the overall impact of PGE_2 on tumor microenvironment (Finetti et al., 2020).

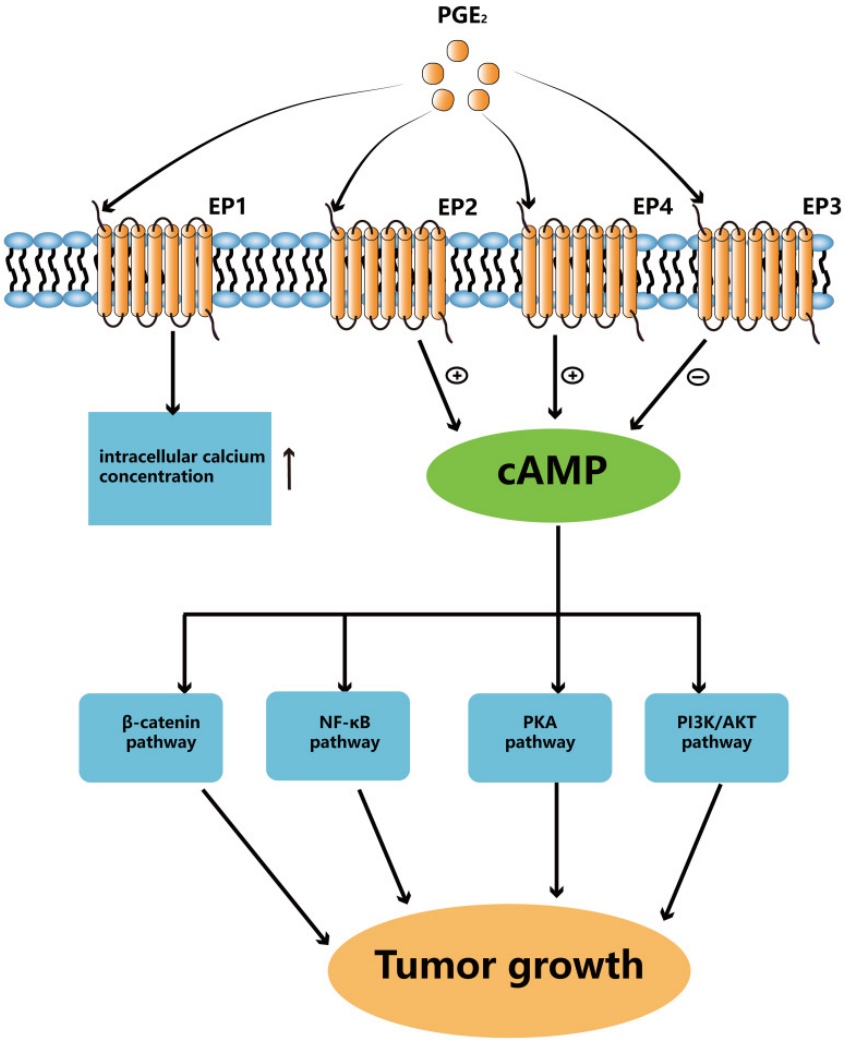

Figure 15: PGE_2 can bind to four different EP receptors, that will activate different downstream signaling pathways. EP1 can when activated upregulate the intracellular Calcium ion concentrations. EP2 and EP4 can upregulate cAMP that will activate the PKA pathway, β-catenin pathway, NF-κB pathway and the PI3K/AKT pathway which can promote tumor growth. When PGE_2 binds to the EP3 receptor, the cAMP levels are downregulated. Figure is borrowed from the article Cyclooxygenase-2-Prostaglandin E2 pathway: A key player in tumor-associated immune cells (Jin et al., 2023)

Necrotic tumor cells can release high levels of PGE_2 that suppress the immunostimulatory activity of DAMPs (Hangai et al., 2016). The tumor microenvironment can also experience considerable impact from PGE_2, where it contributes to immune suppression by inactivating CD8 T-cells and NK cells. Therefore, PGE_2 regulates tumor evasion, ultimately contributing to increased tumor progression (Finetti et al., 2020).

2.5.3 Cancer treatments utilizing the immune system

Cancer cells share similarities with virus-infected cells, as both are normal cells with interior alterations. When cancer cells are detected, the immune system initiates a response similar to eliminating infected cells. However, cancer cells can develop mechanisms to evade the immune systems and become immunosuppressive, allowing them to grow into tumors (Parham, 2021).

Understanding and exploiting these suppressor mechanisms is a primary focus in tumor immunology, with the aim of developing more effective cancer treatments (Parham, 2021). In section 2.5.2 two of these mechanisms are described.

To enhance the efficacy, immunotherapy is introduced as a part of cancer treatment. This could consist of drugs that inhibits the enzyme activity (Jin et al., 2023), or immune checkpoint inhibitors to inhibit interactions between checkpoints (Dahl et al., 2019). These inhibitors consist of specific antibodies that bind to the protein on the cancer cells, preventing the tumor cells from engaging with the immune cells (Alberts, 2014). By blocking the immune suppression caused by cancer cells, the immune system is better equipped to fight the cancer cells effectively. An approach to fight cancer is to block the PD-1/PD-L1 pathway, which has proven effective in treating different types of cancers (Caldwell et al., 2017), as illustrated in Figure 16.

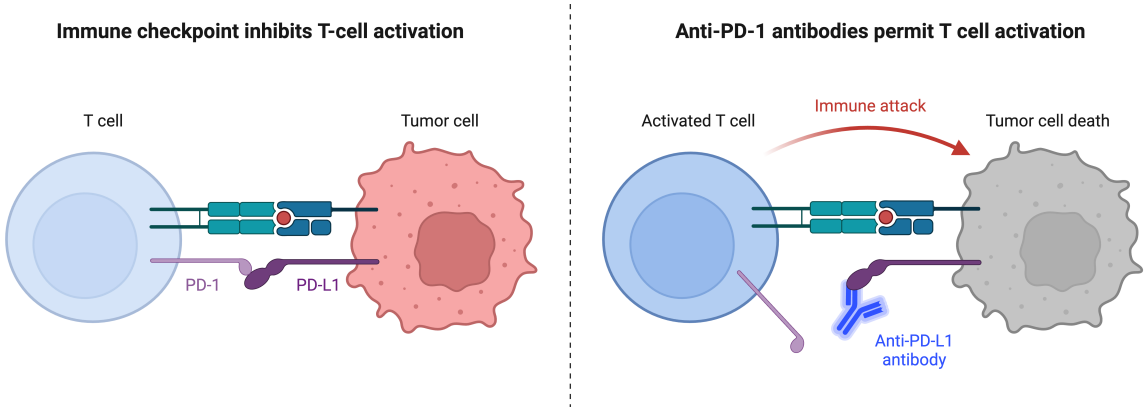

Figure 16: The principle behind immune checkpoint inhibition with anti-PD-L1-antibodies. When the PD-1 on a T-cell binds to the PD-L1 on the cancer cell, the T-cell activation is inhibited, and the tumor cell escapes the immune response. If the PD-L1 on the tumor cell is blocked by an anti-PD-L1 antibody, it cannot bind to the PD-1 on the T-cell. This leads to the activation of the T-cell and the tumor cell is destroyed. The figure was created with BioRender.com.

However, there are risks associated with stimulating the immune system, as cancer cells share a significant amount of DNA with heathy cells. Provoking the immune system to target cancer cells can trigger autoimmune responses that attack healthy cells (Alberts, 2014). Blocking immune checkpoints disrupts the equilibrium between autoimmunity and immune tolerance (Alsaab et al., 2017).

2.6 Analysis

2.6.1 Flow cytometry

The following section on flow cytometry is based on the article Flow cytometry: An Overview (Mckinnon, 2018)

Flow cytometry is a versatile and widely used tool with application in various fields including immunology, molecular biology and cancer biology. It enables the analysis of cell populations based in their fluorescent and light scattering characteristics, utilizing florescent reagents like fluorescently conjugated antibodies and viability dyes. In flow cytometry, lasers serve as light sources to generate scattered and fluorescent lights signals from single cells in a solution, which are then detected by photodiodes and photomultipliers tubes (PMT).

Traditional flow cytometers consist of three main systems. The fluidics system delivers and focuses the sample to the interrogation point for analysis. The optical system includes lasers, PMTs and photodiodes, generating visible and fluorescent light signals used for analysis. The electrical system converts the detector signal into digital signals read by a computer. Newer and more advanced cytometers use ultrasonic waves for improved cell focusing before the laser interrogation point, known as acoustic focusing, allowing faster sample analysis and less clogging.

During flow cytometry analysis, single cells suspended in a buffered salt-based solution are prepared for fluorescent measurement. This preparation can involve staining with fluorescent dyes such as propidium iodine or immunostaining with fluorescently conjugated antibodies. The prepared cells are then analyzed as they pass by one or more lasers and each cell is analyzed for visible light scatter and fluorescence parameters. The forward scatter (FSC) provides information about the relative size of the cell, while the side scatter (SSC) at 90 degrees indicates the cell's granularity.

2.6.2 ELISA

Enzyme-Linked Immunosorbent Assay (ELISA) is an assay used for detection and quantitative analysis of various substances, making it a valuable tool in biomedical research and medical diagnostics (Konstantinou, 2017). ELISA is based on the fundamental immunology concept that an antigen binds to its specific antibody, enabling the detection of small quantities of proteins, peptides, hormones or antibodies in a liquid sample (Konstantinou, 2017).

There are different types of ELISA with various modifications, but the main steps involve the direct or indirect detection of an antigen by adhering or immobilizing the antigen or antigen-specific capture antibody onto the surface of the well (Gan & Patel, 2013). For small antigens, a competitive version of ELISA is used, where a conjugate (analyte coupled to a detection regent) competes with the analyte for binding.

The more analyte contained in the sample, the less conjugate will be bound, and the lower the signal will be, illustrated in Figure 17. This specific type of ELISA is the focus of this thesis and is used to analyze the samples.

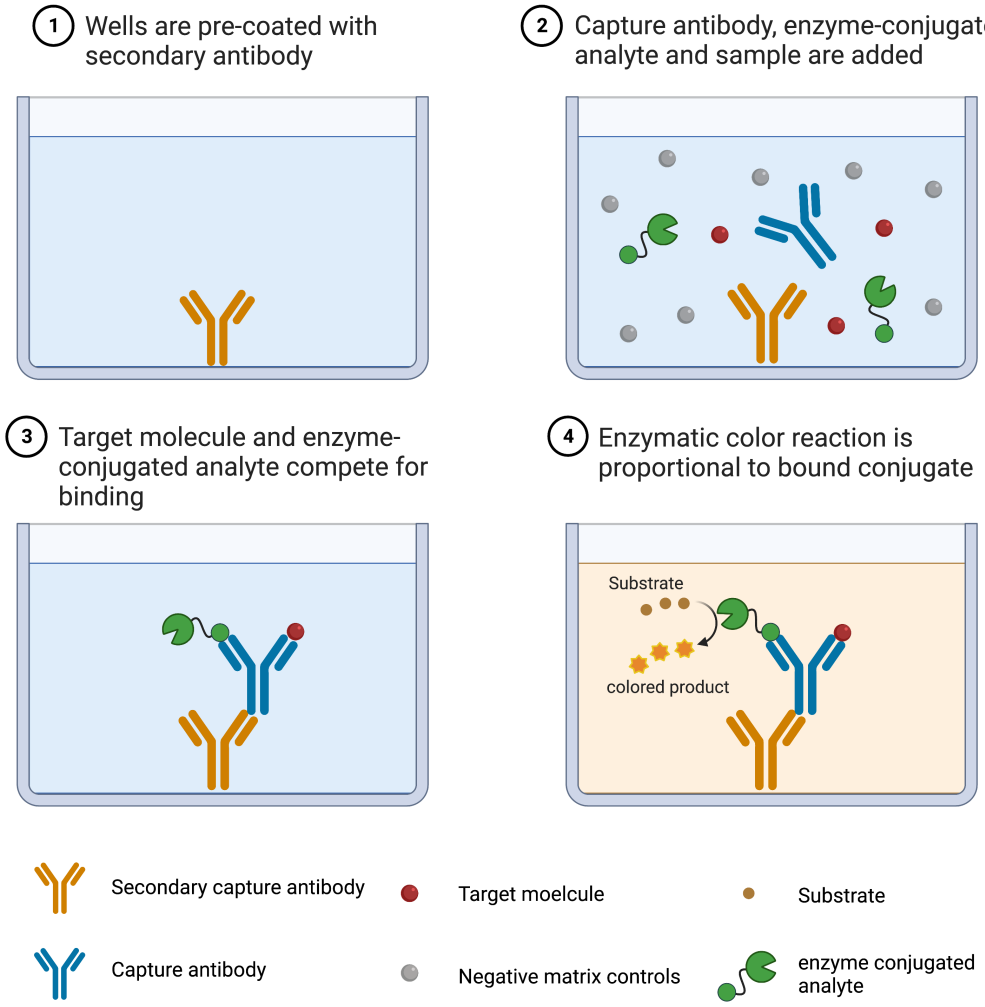

Figure 17: The principle behind competitive ELISA. 1: Each well is pre-coated with secondary antibodies. 2: The sample with the target molecule, enzyme-conjugated analyte and capture antibody is added to each well. Negative matrix controls are used as controls in the assay. 3: The target molecule and the enzyme-conjugated analyte competes for binding to the secondary antibody, 4: Substrate is added, and the enzymatic color reaction is proportional to bound conjugate. The figure was created with BioRender.com.

2.6.3 Welsh's t-test

The following section is based on the article: Why Welch's test is Type I error robust (Derrick & White, 2016)

The t-test is a statistical test used to compare the means of two independent samples and assess whether they are significantly different from each other. There are different t-test that can be used, where the type of data decides which test is a better fit. In this thesis the independent samples t-test with unequal variances was used (Welch's test). This test presumes that the data is normally distributed and that the variances are not equal.

The p-value generated from the t-test represents the probability of observing the data if the null hypothesis were true. A p-value greater than 0.05 (5%) indicates that our observation is not so unlikely to have occurred by chance, and the null hypothesis cannot be rejected. However, if the p-value is below 0.05 (5%), it suggests that there is evidence against the null hypothesis, and the difference in the samples is considered statistically significant. The t-value measures the size of the difference in samples relative to the variation in the sample data. A larger t-value indicates a larger difference between the two samples, which contributes to a smaller p-value and strengthens the evidence against the null hypothesis.

3 Method

3.1 Cell lines

In this thesis, three different cell lines were used to investigate the aims, one human cell line, A549, and two murine cell lines, MOC1 and MOC2. These were all adherent and immortalized cell lines. These cell lines were chosen because they are used in a project called ProGRID, which this thesis is a part of.

The A549 cells are lung carcinoma cells, originating from a 58-year-old Caucasian male. Murine Oral Cancer 1 (MOC1) and 2 (MOC2) cells originate from C57BL/6 mice. These cell lines were created for use in syngeneic mouse models and are used in ProGRID to gain insight into the effects of combining radiation therapy and immunotherapy in an animal model, but it is also very interesting to study *in vitro* responses. The MOC1 cells are characterized as having a high immunogenicity, while the MOC2 cells have a lower immunogenicity in comparison (Judd et al., 2012).

3.1.1 Mammalian cell culturing

The cell lines are immortalized, meaning that they will divide indefinitely given sufficient space and nutrients. When reaching ~80% confluence, a fraction of the cells should be subcultured into a new flask with fresh cell culture media to maintain optimal growth conditions (Segeritz & Vallier, 2017).

3.1.2 Flasks and dishes

The cells were grown and subcultured in tissue culture flasks, mainly T25 (VWR, USA). For the irradiation experiments/protocols, the cells were subcultured in 60mm Nunc Cell culture dishes (Nunc, Thermo fisher, Denmark).

3.1.3 Subculturing

The subculturing process was performed in BMF´s cell lab. An ordering system is established, where the senior engineer at the department is responsible for subculturing the available stock cell lines. When cells were needed for an experiment, they were subcultured from the requested cell stock by the senior engineer. This ensured constant cell availability for experiments. The stock cells were subcultured every Monday and Friday and supplemented with fresh medium every Wednesday. The cells were maintained at 37°C, 5% CO_2 and 90% humidity in Forma Steri-Cycle CO2 incubator (Thermo Fisher, USA).

The different cell lines were subcultured according to the following process: the growth medium was removed from the flask, followed by washing the bottom twice with 1 ml trypsin-EDTA 1x (ECM0920D, Euroclone, Italy) to remove any remains of cell medium. A few drops of the trypsin-EDTA were left in the flask, before it was incubated at 37°C, 5% CO_2 and 90% humidity. The incubation times were dependent on the cell line, 2-3 minutes for A549

and 10-15 minutes for MOC1 and MOC2. Trypsin is an enzyme that breaks down the protein cells used to adhere to the bottom of the flask and is activated by heat. To help the cells detach after the incubation time, the flask was firmly tapped against a flat surface. The detachment was confirmed under a microscope (Nikon TMS, Japan). Medium was then added to the flask to neutralize the trypsin. The amount of medium added depended on the growth rate of the particular cell line. The desired fraction of the cell suspension was then transferred to a new flask with appropriate amounts of growth medium, and incubated at 37^{o}C, 5% CO_2 and 90% humidity. For a T25 flask, this was usually 0.5 ml cell suspension and 4.5 ml of fresh medium. Prior to irradiation, the cells would be added to 60 mm Nunc Cell culture dishes, according to wanted confluence the day of irradiation.

3.1.4 Cell culture media

The cells grow in a cell line specific medium that contains everything needed to proliferate in an artificial environment. The cell culture medium used for MOC1 and MOC2 was IMDM nutrient mix (ECB2072L, Lonza, USA) supplemented with 5% fetal bovine serum (Biochrome AG, Germany), 0.5% streptomycin (Lonza,USA) and 0.1% insulin (5mg/ml, gibco, Thermo fisher, USA). The medium used for the A549 cells was DMEM/F-12(12-7195F, Lonza, USA), supplemented with 10% Fetal bovine serum (Biochrom AG, Germany) and 1% streptomycin (Lonza, USA).

3.1.5 Aseptic cell work

'Microbiological infections represent the main problem for the maintenance of cells in vitro' (Segeritz & Vallier, 2017). Compared to cell proliferation time, bacteria and fungus have higher doubling time and they will quickly outgrow the cells. These contaminations can alter the phenotype and genotype of the cultured cell line through competition for nutrients, synthesis of alkaline and acidic or toxic by-products. Ultimately, they are toxic to eucaryotic cells and can lead to cell death (Segeritz & Vallier, 2017).

The air is filled with particles that can have an infectious effect, and therefore a Laminar Air Flow Safe 2020 class 2 microbiological safety cabinet (Thermo Scientific, USA) was used for all cell work that needs to be aseptic. In a LAF bench, the air is filtered through a high-efficiency particulate absorbing (HEPA) filter before it is blown vertically in a laminar flow from the top. To avoid disturbance to the airflow, only necessary equipment should be brought into the LAF bench. Work in the bench was performed with nitrile gloves sprayed with 70% ethanol (Antibac, Norway). Prior to any work, 70% ethanol was sprayed on the surface and wiped. Equipment used for the experiment was also sprayed with 70% ethanol before transferred into the bench. Afterwards, Milli-Q water (Merck Millipore Milli-Q, Germany) was sprayed on the surface and wiped. Followed by Deconex (DuPont, UK) to disinfect the surface, and lastly everything was sprayed with 70% ethanol and left to evaporate.

3.2 Photon irradiation

The photon irradiations were performed with an x-ray machine, Pantak PMC1000 (Pantak, USA) using a tube voltage of 220 kV and tube current of 10 mA. The photons were filtered through a 1.52 mm aluminum plate and a 0.5 mm copper plate, before entering a 37°C heated chamber. In the chamber, cell dishes prepared as described in section 3.1.3 were placed on a shelf with a source surface distance (SSD) of 60 cm. The shelf was made of PMMA plastic as this material gives minimal back scattering during irradiation. An image of the x-ray chamber is shown in
Figure 18. The irradiation time needed for the specific doses is given in Table 1.

Table 1: Irradiation time for the different doses, with tube voltage of 220 kV, tube current of 10mA and an SSD of 60 cm.

Dose [Gy]	Time [mm:ss]
2	3:23
4	6:47
6	10:10
8	13:34
12	20:20

Preparation of cell dishes prior to irradiation

Prior to the irradiation, the cell dishes prepared in the first steps of the PD-L1 experiment (section 3.4) were wrapped in parafilm (Bemis, USA) inside a LAF bench. The parafilm was placed in thin strips around the dish, sealing the opening between the base and the lid. By using parafilm, the dishes would maintain approximately the same CO_2 levels and humidity during the time outside the incubator and be protected against contamination during transport and irradiation.

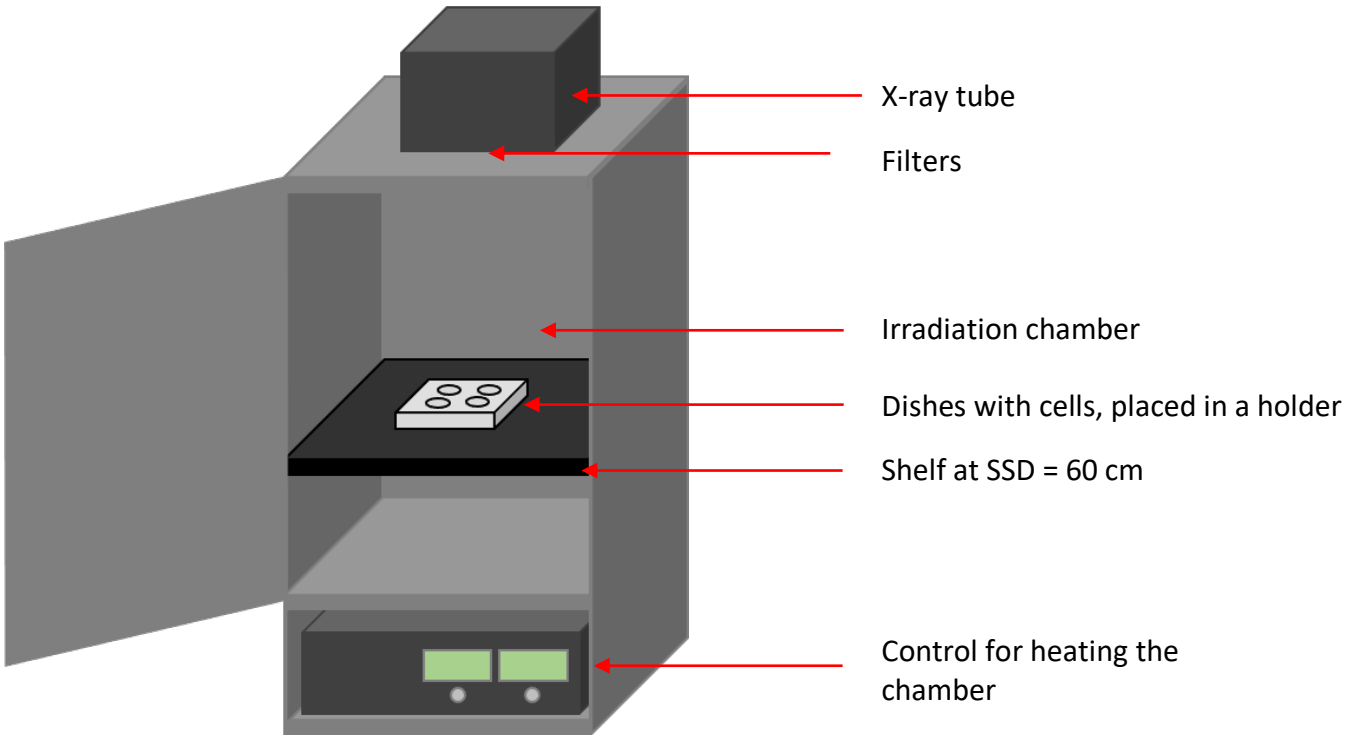

Figure 18: The x-ray chambers where the cells were irradiated. Photons are generated in the X-ray tube and filtered before entering the chamber. The cell dishes were placed in a holder on a shelf at SSD = 60 cm. The heating element at the bottom can be turned on to heat the chamber to approximately 37°C.

The irradiation process

A Styrofoam box disinfected with 70% ethanol was used to transport the wrapped dishes to a room at 37°C located close to the x-ray machine. The box was heated using flasks filled with warm water to maintain a stable temperature for the cells during transport. From here, the dishes were sequentially placed in a holder, shown in Figure 19, and transported to the x-ray chamber for irradiation, while the remaining dishes stayed in the room at 37°C. The holder can contain up to 4 dishes and is made from PMMA plastic. The placement of the dishes was aligned along a drawn grid to minimize the risk of experimental variation.

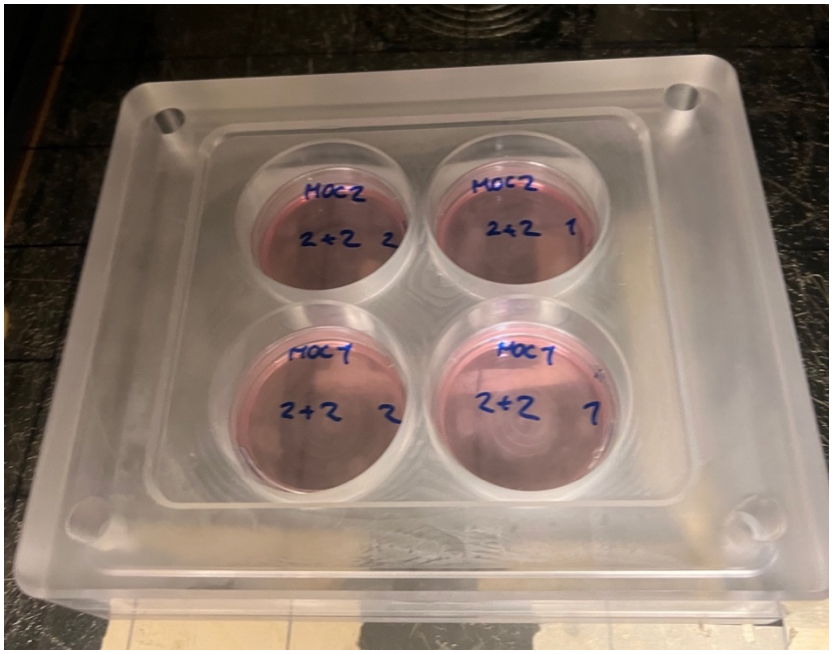

Figure 19: PMMA holder the cell dishes were irradiated in. The holder can contain up to 4 dishes.

After the irradiation of the first dishes, the holder was transferred back to the 37°C room, and reloaded with the next dishes to be irradiated. These steps were repeated until all the dishes had been irradiated. The dishes were then placed into the heated Styrofoam box and brought back to the cell lab. Inside the LAF bench, the parafilm was removed and any spillage between the lid and base was carefully cleaned with a sterile Q-tip before the cell dishes were placed back into the incubator. The cells were incubated for 24 hours at 37°C and 5% CO_2 until the next irradiation dose or the PD-L1 flow cytometry assay was performed.

3.2.1 X-ray dosimetry

The dosimetry performed on the x-ray chamber is done with a free air dosimeter (FC65-G, IBA, Germany) and a connected max 4000 electrometer (Standard Imaging, USA). To calculate the dose in the sensitive volume of air, formula is used with the number of charges (M_u) read from the electrometer (Waldeland et al., 2010).

$$D_w = M_u N_k k_u p_u k_{TP} \left(\frac{\overline{\mu}}{\rho}\right)_{air,water} \quad (12)$$

Where N_k is the air kinetic energy released per mass (KERMA) calibration factor for the beam quality, k_u is a correction factor for the change in response due to change in the spectral distribution of the beam between air and water (Waldeland et al., 2010). p_u corrects for perturbation and k_{TP} corrects for the temperature and air pressure, compared to the condition during the calibration of the dosimeter. The dosimeter registers the dose given to a volume of air, while the dose to water is the relevant dose for radiobiology,

as our cells consist of 70% water (Alberts, 2014). The factor $\left(\frac{\overline{\mu}}{\rho}\right)_{air,water}$ in equation 12 corrects for this with the ratio of the mass energy absorption coefficient of water and air, averaged over the photon spectrum. This is a tabulated value and was found for our experiments in table I in (Waldeland et al., 2010).

3.3 Proton irradiation

The proton irradiation was conducted at the Oslo Cyclotron Laboratory (OCL) using the Scanditronix MC-35 cyclotron (Scanditronix, AB, Uppsala, Sweden). The OCL facility is conveniently located close to the cell culture lab, in the basement of the Physics building at the University of Oslo. This following section describes the process of proton irradiation in two distinct positions along the Bragg peak.

In this thesis, the irradiation was performed on cell dishes in two different positions relative to the Bragg peak. In front of the Bragg peak, where protons have comparable to that of x-rays (LET~10 $KeV/\mu m$), and in the distal end of the Bragg peak with a higher LET (LET~40 $KeV/\mu m$) (Sankaya, 2022). In the clinical setting, the radiation in front of the Bragg peak is more representative with a RBE = 1.1. To investigate the impact of different LET values on inducing biological effects in cells, irradiation of MOC1 and MOC2 cells was conducted in front of and in the distal end of the Bragg peak using doses of 4 and 8 Gy.

Preparation of cell dishes prior to radiation

The prepared cell dishes were transported from the cell culture lab to the OCL facility in a heated Styrofoam box that had been disinfected with 70% ethanol. In the OCL facility, there is a lab space with an incubator (NuAire, UK) and a LAF bench (LabGard, NuAire, UK), where the preparation prior to the irradiation was performed.

The cells were maintained at a temperature of 37°C and 5% CO_2, in the incubator when they were not irradiated. Each cell dish had to be irradiated individually, with some preparations. Prior to the irradiation, the medium was carefully removed from the cell dishes in the LAF bench. Any residual drops were carefully removed with a sterilized Q-tip. The subsequent steps varied depending on the irradiation position.

For irradiation in front of the Bragg peak, a sterilized piece of Parafilm was used to seal the cell dish, acting as a lid. Conversely, in the distal end of the Bragg peak, the provided lid was used with a sterilized Parafilm to ensure a tight seal. The substitution of the lid with Parafilm for irradiation in the distal end of the Bragg peak was essential due to the lid's thickness, which would have caused the cells to be in the back of the Bragg peak.

The irradiation process

The sealed dishes were then placed within a specially made PMMA cell dish container, which had been pre-heated in the incubator. This container was transported from the laboratory to the experimental hall, where it was mounted vertically perpendicular to the beam line. During irradiation, the container was continuously rotated to prevent any residual medium from pooling at the dish bottom. This would give the radiation a different LET and a different dose to the cells behind this medium.

Once the desired dose was delivered, the container was transported back to the laboratory's LAF bench. The Parafilm was removed, fresh medium was added, and the cell dish was returned to the incubator. This process was repeated until all the cell dishes were irradiated. Finally, the cell dishes were transported back to the cell culture lab in a heated Styrofoam box disinfected with 70% ethanol. The average time for the cell dishes to be without medium was below 5 minutes.

3.3.1 Proton Dosimetry

Earlier work has established the initial proton energy of the proton beam at OCL to be 15.5 MeV (Dahle et al., 2017).

Dosimetry was performed each morning before conducting experiments to establish the position of the Bragg peak, since the mean intensity was not constant. When there was a change in position, the dosimetry process was repeated accordingly. During dosimetry measurements, a Marcus chamber dosimeter was placed in place of the cell dish container for monitoring.

To monitor the delivered dose to the cell dish, a transmission chamber was used. The required number of monitor units to achieve the desired dose had to be determined during initial dosimetry procedures for each position in the Bragg peak. The beam was manually stopped once the specified amount of monitor units was reached.

3.4 PD-L1 flow cytometry assay

The main analytical method used for this thesis was the PD-L1 antibody staining assay that was developed by Nina F.J. Edin. Immunostaining is a technique where the cells are incubated with an antibody conjugated with a fluorochrome that detects and attaches to a specific protein (Maity et al., 2013). The protein levels can then be quantified by detection of the antibodies using flow cytometry (2.6.1.).

The total duration of the PD-L1 experiment was between 3-5 days depending on the number of dose fractions (Figure 20). On day 1, the required number of cells were seeded into dishes (60 mm) from preordered T25 flasks using the subculturing conditions described in 3.1.3. The cells were seeded to achieve 70% confluence at the day of irradiation.

When the desired confluence was reached, the cells were irradiated according to section 3.2. The total dose was delivered in either one-, two- or three-fractions. When irradiated with one fraction, the cells would receive the total dose, according to Table 1, in one fraction followed by the PD-L1 flow cytometry assay 24 hours later. When the total dose was delivered in two fractions, the cells would be irradiated with half of the total dose, then the second half 24 hours later, and the PD-L1 flow cytometry assay was performed 24 hours after the final fraction. For three fractions, the cells were irradiated with 8Gy on three consecutive days, total dose of 24 Gy, and the PD-L1 flow cytometry assay was performed 24 hours after the final fraction. An overview of the timeline is shown in Figure 20.

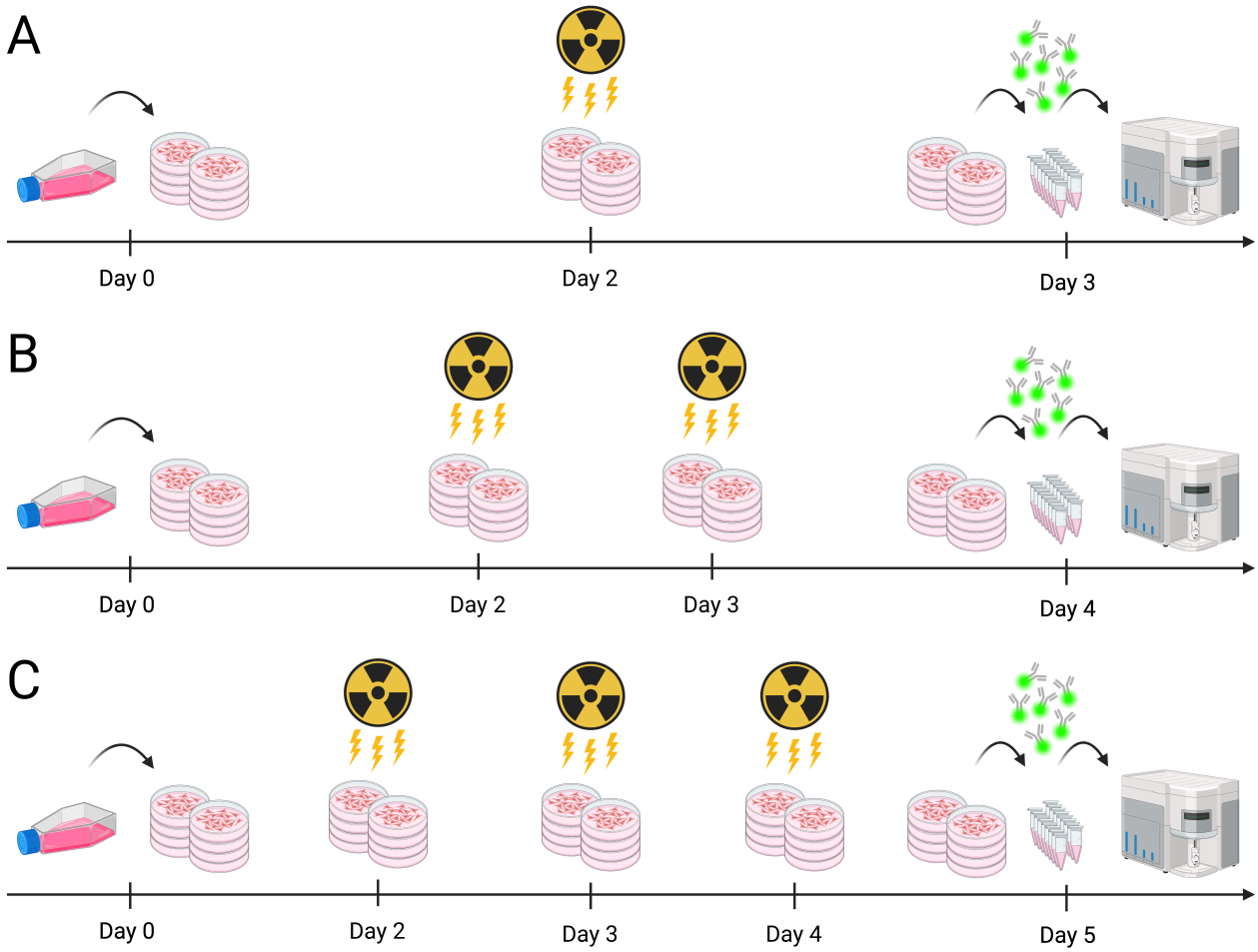

Figure 20: ***The timelines of the PD-L1 experiments dependent on type of fractionation scheme. A****: PD-L1 experiment with one fraction of radiation: Cells were seeded on day 0, irradiated on day 2 and the immunostaining and flow cytometry analysis was performed on day 3.* ***B****: PD-L1 experiment with two-fraction of radiation: Cells were seeded on day 0, irradiated on day 2 and 3, and the immunostaining and flow cytometry analysis was performed on day 4.* ***C****: PD-L1 experiment with three fractions of radiation: Cells were seeded on day 0, irradiated on day 2, 3 and 4, and the immunostaining and flow cytometry analysis was performed on day 5. Each day is a 24-hour time span. The figure was created with BioRender.com.*

The first step of the PD-L1 protocol was to detach the cells from the dishes and transfer them into 15 mL tubes (Sarstedt, Germany). The medium was removed, and the dishes were washed with 5 mL Phosphate Buffered Saline (PBS) x1 (Lonza, Belgium) to remove all remains of medium. The cells were detached by trypsination with TrypLE Express (12605-028, Gibco, USA) for 8-12 minutes, depending on the cell type. Compared to trypsin-EDTA used to subculture the cells (section 3.1.3), the trypLE does not contain EDTA, which is preferable for this assay because PD-L1 is located on the cell membrane. The cell suspension was transferred to 15 mL tubes, with 4 mL of the corresponding cell growth medium.
The tubes were centrifuged (Mega Star 600, VWR, USA) for 4 minutes at 200 g. For the rest of the assay, the cells were kept on ice to slow down the cell cycle. The supernatant was removed, and the cell pellet was resuspended in 2 mL PBS. The cell suspension was equally divided into two 1.5 mL micro tubes (Sarstedt, Germany), one sample and one control. The samples were centrifuged (Mega Star 600R, VWR, USA) at 4^{o}C for 4 minutes at 200 g, before prepared staining solutions were added: One sample was incubated on ice with the primary antibody for PD-L1 (FAB9078R, R&D systems, USA) mixed with PBS + 1% BSA and the control was incubated on ice with an isotype control (IC1051R, R&D systems, USA) mixed with PBS + 1% BSA. Both antibodies were conjugated with Alexa fluor 647 fluorescents. The isotype control is an antibody that will not bind to anything known on the cells and represents the amount of nonspecific binding in the sample (Maecker & Trotter, 2006). BSA was added to both samples to further decrease unspecific binding as BSA will occupy the non-specific binding sites instead of the antibodies. After 30 minutes of incubation, the samples were washed twice with 1 mL of PBS and centrifuged (Mega Star 600R, VWR, USA) at 4^{o}C for 4 minutes at 200 g, and then resuspended in 250 μL PBS. Before the analysis, 0.5 μL Propidium Iodine (PI) (Thermo Scientific, Germany) was added to exclude non-viable cells. This is because PI does not penetrate the plasma membranes of live cells but is able to stain the nuclei of broken, dead cells (Crowley et al., 2016). The dead cells can be filtered out from the data by exclusion of cells stained with this dye (Mckinnon, 2018). Lastly, the samples were filtered before analyzed with a Accuri C6 Flow cytometer (BD Biosciences, USA).

In the experiments performed after April 2023, the new Attune NxT Acoustic Focusing Cytometer (Thermo Fisher Scientific, Germany) was used to analyze the samples. To accommodate the new instruments, two adjustments had to be made to the protocol. In the final step before the analysis of the samples, the cells were resuspended in 750 μL PBS instead of 250 μL and 1.5 μL of PI was added instead of 0.5 μL.

3.4.1 Analyzing fluorescence signal from flow cytometry

In flow cytometry analysis, data obtained from the fluorescent and light scattering characteristic of cells were through two-parameter histograms, as shown in Figure 21. This presentation allows for visual representation of the relationship between different parameters and identifying distinct cell populations based on their characteristics (Maecker & Trotter, 2006). For each assay, setup controls specific to the fluorochromes and cells were

required (Maecker & Trotter, 2006). One of these controls is used to adjust the voltage of the PMT to ensure that all events are within scale. In this thesis this is only relevant the Attune NxT cytometer, as the settings for the Accuri instrument were all automatic. If the signals are too high and exceed the scale, the PMT voltage should be reduced and vice versa if the signals are too low (Maecker & Trotter, 2006).

Gating is an essential tool in flow cytometry and is used to determine the proportion of the cell population positive for a specific characteristic of interest (Maecker & Trotter, 2006). Defining a gate around the cells expressing the characteristic gives the possibility for specific cells to be selected for further analysis of other characteristics (Mckinnon, 2018). Gating is especially valuable when staining with multiple fluorochromes, where different florescent markers identify different cell populations simultaneously. For example, like in this thesis, using an antibody conjugated with a fluorochrome and a staining dye like PI, the staining dye can be gated on to exclude cells with broken membranes from the analysis, ensuring that the only population of viable cells, is considered (Mckinnon, 2018).

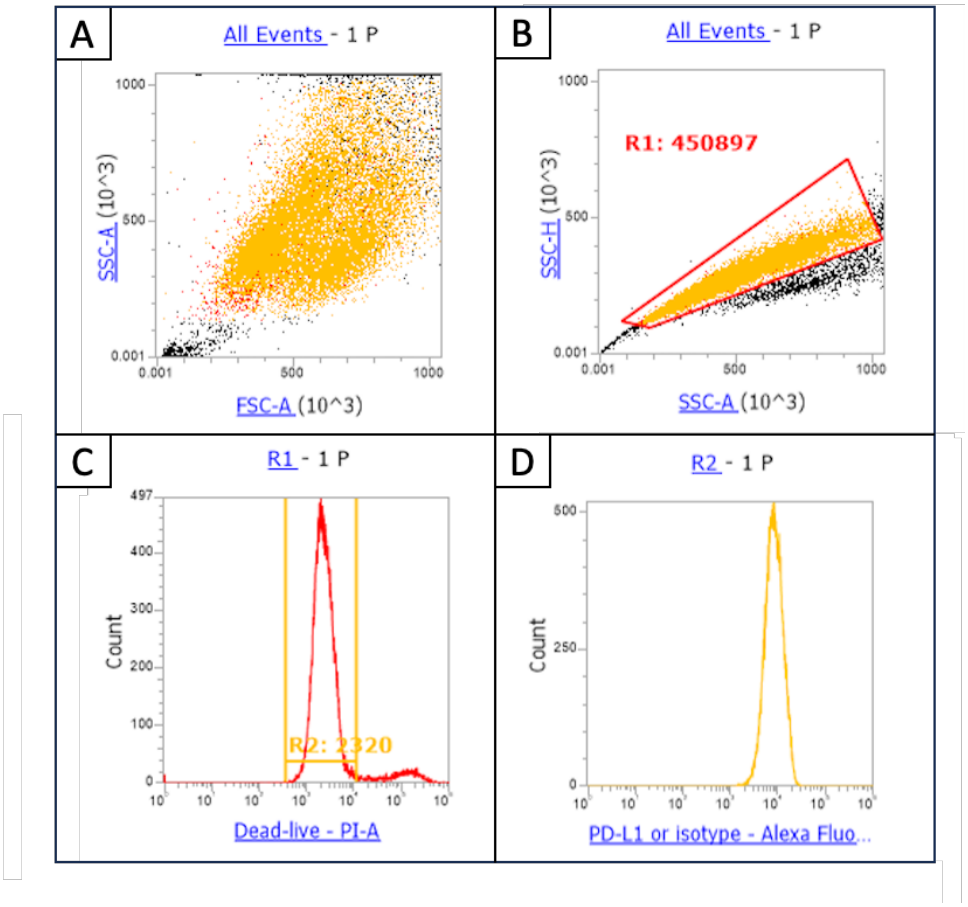

Figure 21: An example of how the data is presented after a sample is analyzed with the flow cytometer Attune NxT flow cytometer (Thermo Fisher Scientific, Germany). This specific analysis shows the data obtained from MOC1 cells irradiated with 8 Gy and incubated with anti-PD-L1 (1 biological replicate) from the PD-L1 assay performed on 28.05.2023. A: A two variable histogram of all the events. The side scatter (SSC) detected is plotted against the Forward scatter (FSC) detected. B: A two variable histogram of all the events. The side scatter is plotted against the side scatter and is used to gate for single cells. C. The florescent signal detected from the laser exciting propidium iodine and used for gating for membrane intact cells. D. The signal detected from the laser for the fluorochrome and is gated for the single cells and membrane intact cells.

The data obtained from the flow cytometer represents the median value of the fluorescent signal detected, which were gated for the wanted cell population. The values used in the further analysis were the median value of the curve shown in Figure 21D. This value was retrieved for all the samples run on the flow cytometer.

As mentioned in above, the cell suspension from each cell dish was divided into two samples. One sample was incubated with the anti-PD-L1 antibody, while the other sample was incubated with an isotype control. The isotype control was used as a reference for non-specific binding in the samples. To determine the signal from actual binding of PD-L1 of all the samples, equation 13 was used:

$$S = \frac{(P_s - I_s) - (\overline{P_c - I_c})}{\overline{I_c}} \quad (13)$$

where P_s represents the median value of the fluorescent signal detected in the sample incubated with anti-PD-L1 and I_s represents the median value of the fluorescent signal detected for the sample incubated with the isotype control. This value was subtracted by the average of the respective control values (cells that did not receive a dose) and divided by the mean of the signal from the isotype binding in the two controls. Signal S represents the normalized PD-L1 signal. To calculate the PD-L1 signal on unirradiated cells equitation 14 was used:

$$\frac{P_C - I_C}{I_C} \quad (14)$$

where P_C is the median fluorescent signal from the sample incubated with the anti PD-L1 and I_C is the median fluorescent signal detected from the sample incubated with the isotype control.

3.5 PGE_2 ELISA assay

The ELISA assay was used for analyzing the concentration of PGE_2 in the cell medium after irradiation. The kit Prostaglandin E_2 Parameter Assay Kit (KGE004B, R&D systems, USA) was used, which is a forward sequential competitive enzyme immunoassay (2.6.2). In a competitive ELISA, the important process is the competitive reaction between the antigen in the sample and the antigen bound to the wells with the primary antibody (Gan & Patel, 2013).

In this process, the PGE_2 in the sample competes with the horseradish peroxidase (HRP)-labeled PGE_2, for a limited number of binding sites on a mouse monoclonal antibody. During the first incubation, the PGE_2 in the sample binds to the antibody, and in the second incubation HRP-labeled PGE_2 binds to the remaining antibody sites. After removing the unbound components through washing, a substrate solution is added to the wells to

determine the bound enzyme activity. The color development is stopped by a stopping solution, and the absorbance is measured. The intensity of the color is inversely proportional to the concentration of the PGE_2 in the sample.

Sample and reagent preparation

Samples for analysis consisted of medium harvested from the cell dishes 24 hours after irradiation. Once extracted, the samples were frozen down in 1.5 mL tubes until the assay was performed. On the day of the measurements, the samples were thawed, vortexed and centrifuged for 5 minutes at 200g (Mega Star 600, VWR, USA) to remove particulates. According to instructions, the samples were diluted 1:3 with 150 µL of sample and 300 μL of Calibrator Diluent RD5-56, included in the assay kit.

Reagents such as wash buffer, substrate solution and PGE_2 standard were prepared according to the product datasheet. A 7-point dilution of PGE_2 standard was prepared for calibration. The Calibrator Diluent RD5-56 served as the zero standard (S_0).

Assay procedure

The kit contained a pre-coated 96-well plate where all the samples and standards (S) were added. To some wells only calibrator dilutant and not a primary antibody solution was added, representing the non-specific binding (NSB) control. Following the placement illustrated in Figure 39 in appendix section 8.2.1, 150 μL of the diluted samples and standards and 200 μL of Calibrator Diluent RD5-56 (NSB) were added to each well. Subsequently, 50 μL of primary antibody solution were added except for the NSB wells. The plate was sealed and incubated at room temperature on a horizontal orbital microplate shaker set at 275 RPM. Next, 50 μL of PGE_2 conjugate was added to each well, followed by a 2-hour incubation on orbital shaker. After incubation, the plate was washed four times, with the final wash followed by drying against a clean paper towel. 200 μL of the substrate solution was added to each well and incubated for 30 minutes on the tabletop protected from light. Finally, 100 μL of stop solution was added to each well, completing the preparation before measurements.

Data analysis

Optical density (OD) readings of each well were determined using a Ledetect 96 microplate reader (Dynamica, UK). The wavelength was set to 450 nm, with a reference filter at 595 nm to correct for optical imperfections in the plate. Before analysis, the plate was shaken for 5 seconds at medium speed. The OD readings were recorded and the average NSB optical density was calculated and subtracted from the OD of the other wells.

A standard curve was generated by fitting the OD data from the standard wells to a four-parameter logistic (4-PL) curve fit, described by equation 15, as instructed in the kit protocol. The curve_fit function from SciPy.Optimize library in Python3 was used.

$$y = d + \frac{a-d}{1+\left(\frac{x}{c}\right)^{b}} \tag{15}$$

The averaged readings from correspond samples were used with the standard curve to determine the concentration [pg/mL], which was then multiplied by the dilution factor.

3.6 Statistical analyses

The experimental data consisting of multiple independent experiments were evaluated with the Welsh's t-test described in section 2.6.3, to determine the statistical significance. The tests were performed by using the function ttest_ind from scipy.stats in Python3.

Uncertainty in the data are represented by error bars that represent the error of the mean, if not otherwise is stated.

4 Results

The objective of this thesis was to investigate the effects of radiation therapy on immunosuppressive mechanisms. In particular, the amount of PD-L1 expressed on the cell membrane and the concentration of secreted PGE_2 were examined. The effects were investigated in two cell lines with varying immunogenicity: MOC1 with high immunogenicity and MOC2 with lower immunogenicity (3.1). It was initially planned to include the human A549 cell line; however, due to the antibody being mouse specific, its inclusion was not possible. Further details regarding this are discussed in 4.2.2.

The following sections present the results of the experiments conducted. This includes the PD-L1 signal on cells irradiated with one, two, or three fractions of photon and one fraction of proton radiation, analyzed on a flow cytometer and the concentration of PGE_2 in the medium from irradiated cells analyzed with ELISA.

4.1 PD-L1 signal from unirradiated MOC1 and MOC2 cells

The PD-L1 signal on unirradiated MOC1 and MOC2 cells was calculated for all the control samples analyzed. This gives insight into the activity of the immunosuppressing mechanisms of the two cell lines when they are untreated. The average PD-L1 signal on unirradiated MOC1 and MOC2 cells is presented in Figure 22, and shows that MOC2 cells have a significantly higher PD-L1 signal than MOC1 cells.

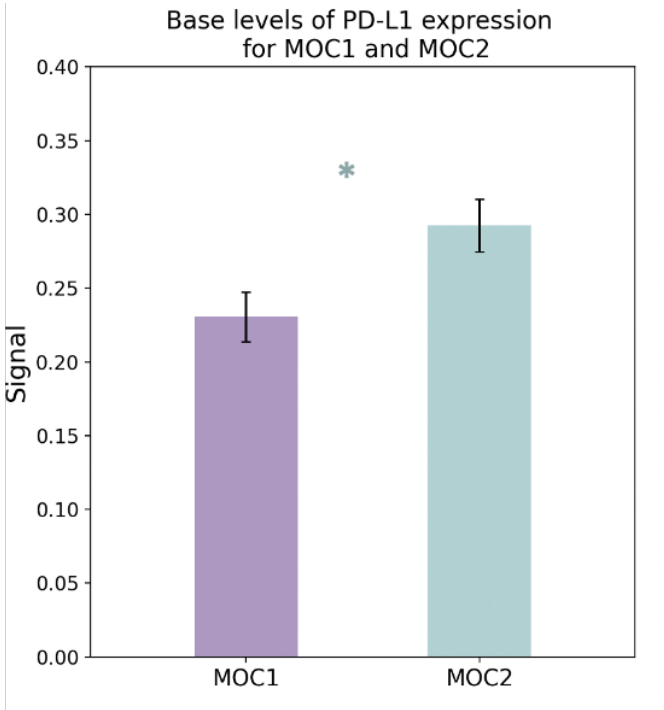

*Figure 22: **The PD-L1 signal of unirradiated MOC1 and MOC2 cells**. The signals are the average value of 44 analyzed samples of MOC1 cells and 42 analyzed samples of MOC2 cells, and the error bars represent the standard error of the mean. The raw data can be found in section 8.1.1 in Appendix. The * indicates a p-value below 0.05 from t-test comparing the PD-L1 signal between unirradiated MOC1 and unirradiated MOC2, that shows MOC2 cells have a higher PD-L1 signal than MOC1 cells (p-value=0.013).*

4.2 PD-L1 signal after one fraction of photon radiation

To investigate the change of PD-L1 signal in response to radiation, MOC1, MOC2 and A549 cells were irradiated with one fraction of photon radiation. Subsequently, the PD-L1 flow cytometry assay was performed 24 hours later. Details of the experiments performed, including the dates, radiation doses, cell lines, flow cytometer used, and additional comments are provided in Table 2.

*Table 2: **Overview of experiments with one fraction of photon irradiation**, including the dates, radiation doses, flow cytometer used, cell lines and additional comments.*

Date	Dose [Gy]	Cell lines	Flow cytometer used	Additional comments
02.02.2022	5 and 10	MOC1, MOC2	Accuri C6 Flow cytometer	Experiments were performed by Nina F. J. Edin
24.02.2022				
23.03.2022				
30.08.2022	4 and 8	MOC1	Accuri C6 Flow cytometer	
31.08.2022	4 and 8	MOC2		
04.10.2022	4 and 8	MOC1, MOC2		
04.11.2022				
19.03.2023				
28.05.2023			Attune NxT Flow cytometer	
17.11.2022	4 and 8	A549	Accuri C6 Flow cytometer	
24.11.2022				
02.12.2023				
03.04.2023 (morning)	12	MOC1, MOC2	Accuri C6 Flow cytometer	
03.04.2023 (afternoon)	12			One biological replicate of a MOC2 control sample was lost
08.05.2023	12		Attune NxT Flow cytometer	One biological replicate of MOC1 irradiated with 12 Gy was lost.
15.05.2023	12			
13.06.2023	12			

Note: The first three assays with doses 5 Gy and 10 Gy were performed by Nina F. J. Edin, prior to my involvement in this project. These data points were included to increase the dataset for analysis.

4.2.1 PD-L1 signal from MOC1 and MOC2 cells after one fraction of photon radiation

The normalized PD-L1 signal for MOC1 and MOC2 cells from each individual experiment is given in the top panels of Figure 23 (MOC1) and Figure 24 (MOC2). The bottom panels of Figure 23 and Figure 24 show the average normalized PD-L1 signal for MOC1 and MOC2 cells, respectively. A comparison between the average PD-L1 signal in response to dose for MOC1 and MOC2 cells is presented in Figure 25. The number of experiments performed for each dose is stated in Table 2, and in the relevant figure legends.

Two experiments encountered data loss that influenced the analysis. In the experiment performed on 03.04.2023 (afternoon), the first biological replicate for the MOC2 control sample, incubated with the primary antibody, was accidentally dropped. This resulted in broken cell membranes, detected during the flow cytometry analysis. Consequently, the signal was deemed non-representative, and control sample 1 was discarded for further analysis. The experiment performed 08.05.23 was the first experiment that used the new flow cytometer. By mistake, the first biological replicate of MOC1 cells that received 12 Gy incubated with the isotype-antibody was not saved after analysis. Consequently, for these two experiments, the values for control sample 1 for MOC2 and sample 12 Gy 1 for MOC1 represent only one sample, not the average between two biological replicates.

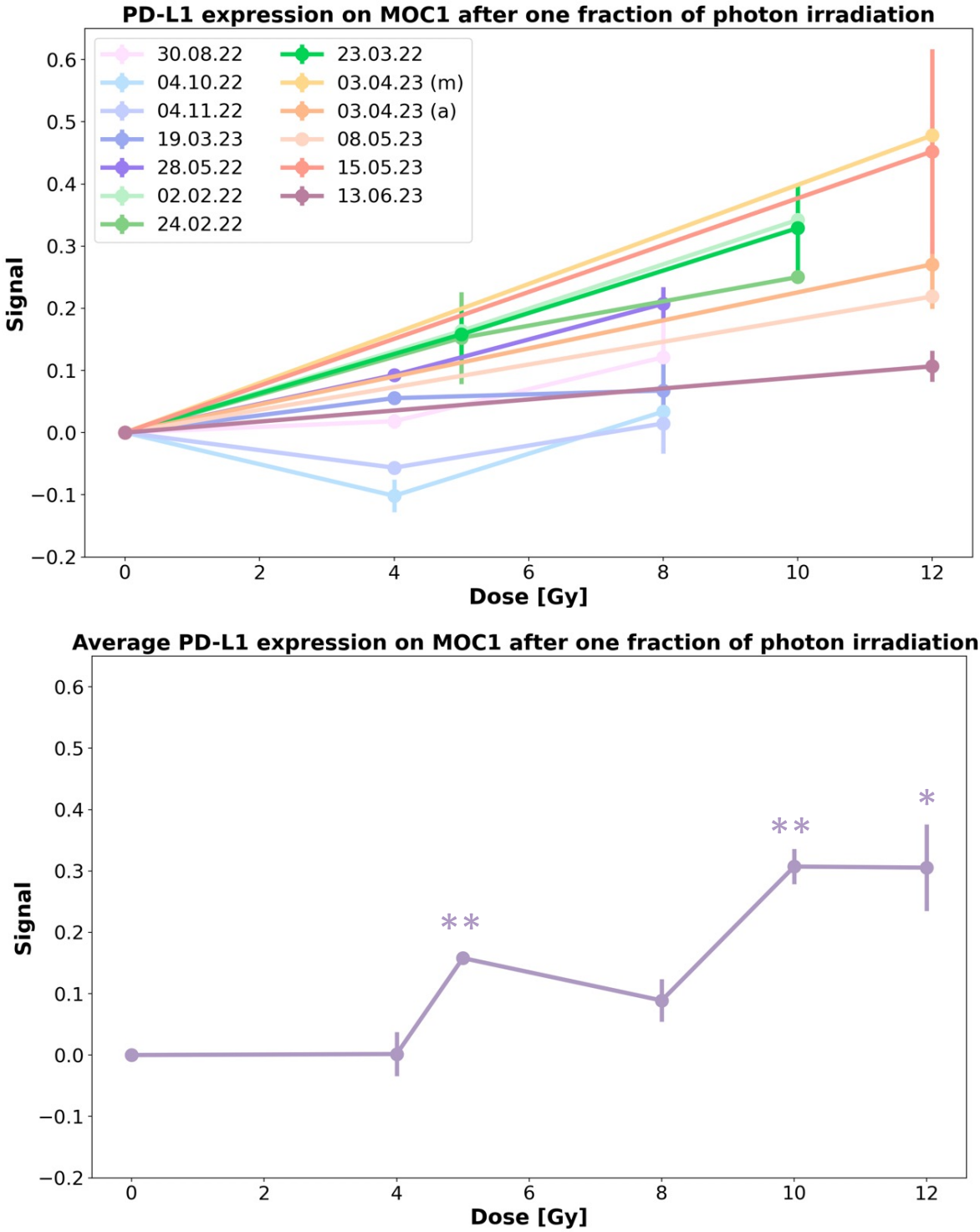

Figure 23: ***Normalized PD-L1 signal on MOC1 cells irradiated with one fraction of photon radiation.*** ***The top panel*** *shows the normalized median fluorescence from PD-L1 antibody on MOC1 cells from each experiment. The different doses tested were 4 Gy (n=6), 5 Gy (n=3), 8 Gy (n=6), 10 Gy (n=3) and 12 Gy (n=5), where 'n' represents number of experiments. The experiments conducted on 03.04.2023 include one in the morning (m) and one in the afternoon (a) and are considered two independent experiments. Error bars represent the standard error between the two biological replicates for each dose in the experiments. The experiment from 08.05.23 does not have an error bar due to the loss of one biological replicate for 12 Gy during analysis. The raw data can be found in section 8.1.1.1 in the appendix.* ***The bottom panel*** *shows the average normalized PD-L1 signal on MOC1 cells after one fraction, and the error bars represent the standard error of the mean. The * indicates a p-value below 0.05 and ** indicates a p-value below 0.01 from t-tests comparing the signal from irradiated to that from unirradiated cells. The p- and t-values generated from the t-test are stated in Table 24, appendix section 8.3.*

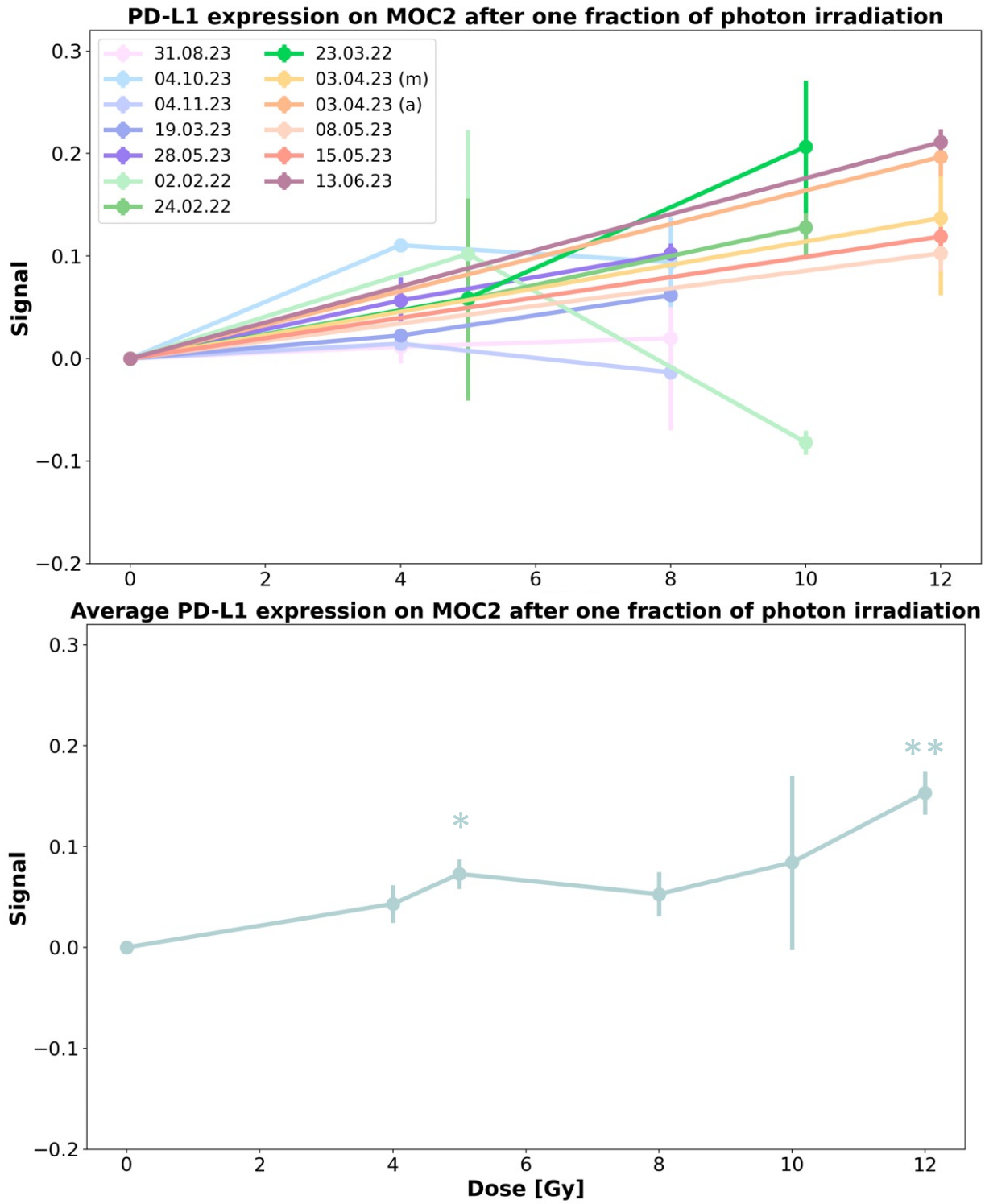

Figure 24: ***Normalized PD-L1 signal on MOC2 cells irradiated with one fraction of photon radiation.*** ***The top panel*** *shows the normalized median fluorescence from PD-L1 antibody on MOC2 cells from each experiment. The different doses tested were 4 Gy (n=6), 5 Gy (n=3), 8 Gy (n=6), 10 Gy (n=3) and 12 Gy (n=5), where 'n' represents the number of experiments. The experiments conducted on 03.04.2023 include one in the morning (m) and one in the afternoon (a) and are considered two independent experiments. Error bars represents the standard error between the two biological replicates for each dose in the experiments. The experiment from 03.04.2023 (a) lost one biological replicate for the control sample during analysis. The raw data can be found in section 8.1.1.2 in the appendix.* ***The bottom panel*** *shows the average normalized PD-L1 signal on MOC2 cells after one fraction, and the error bars represent the standard error of the mean. The * indicates a p value below 0.05 and ** indicates a p-value below 0.01 from t-tests comparing the signal from irradiated to that from unirradiated cells. The p- and t-values generated from the t-test are stated in Table 25, appendix section 8.3.*

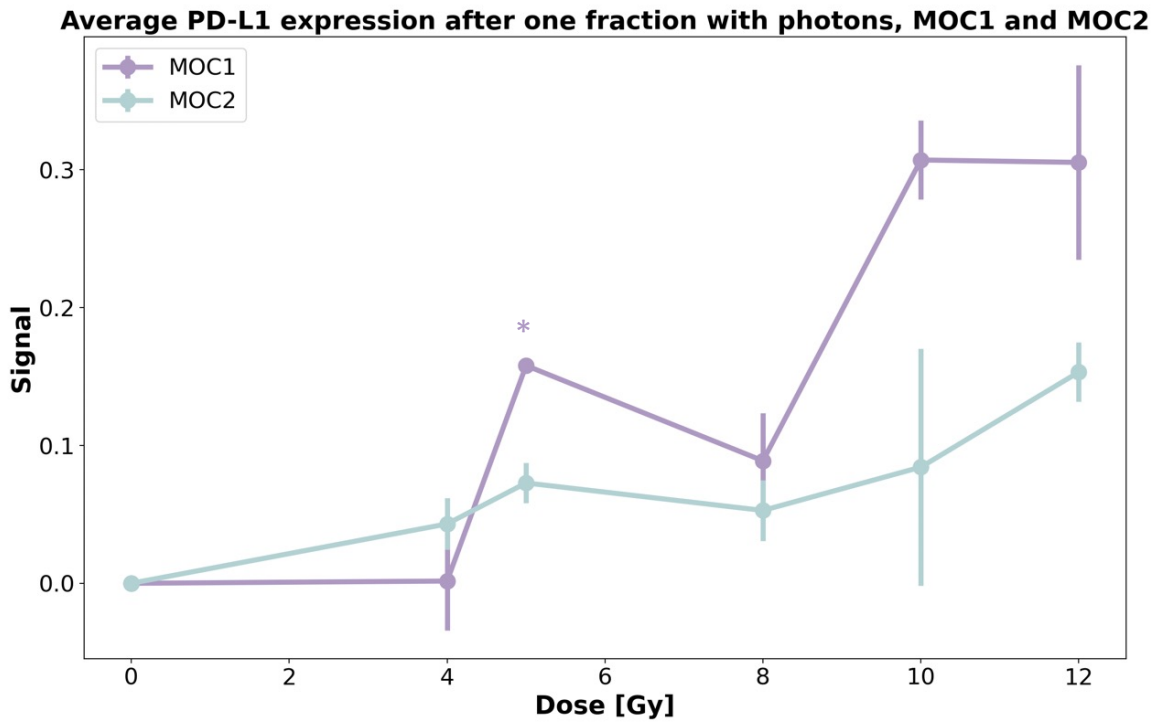

Figure 25: ***Comparison of PD-L1 signal between MOC1 and MOC2 cells irradiated with one fraction of photon radiation****. The average normalized signal of PD-L1 was analyzed after the radiation doses: 4 Gy (n=6), 5 Gy (n=3), 8 Gy (n=6), 10 Gy (n=3), 12 Gy (n=5), where 'n' represents number of experiments. Error bars represents the standard error of the mean. The comparison indicates an increased signal of PD-L1 on the surface of MOC1 cells compared to MOC2 cells for higher doses, which only is statistically significant for 5 Gy. The raw data can be found in section 8.1.1.1 (MOC1) and 8.1.1.2 (MOC2) in the appendix. The * indicates a p-value below 0.05 between the normalized PD-L1 signal from MOC1 and MOC2 cells. The p- and t-values generated from the t-test are stated in Table 26, appendix section 8.3.*

A comparison between the relative PD-L1 signal on the surface of MOC1 and MOC2 cells shows that there is an increased signal of PD-L1 on the surface in response to dose in both cell lines. The increase is however stronger in MOC1 compared to MOC2 cells (the difference between the cell lines is only significant for 5 Gy).

4.2.2 PD-L1 signal from A549 cells after one fraction with photon radiation

Three experiments were conducted with the PD-L1 assay on human A549 cells after receiving one fraction of photon irradiation. However, after performing the assays, it was discovered that the antibodies used were specific for mouse cells and did not work for human cells, rendering the obtained results meaningless for the intended analysis. The raw data are given in section 8.1.1.3 in the appendix.

4.3 PD-L1 signal from MOC1 and MOC2 cells after two fractions of photon radiation

To further investigate the change of PD-L1 signal in response to radiation, MOC1 and MOC2 cells were irradiated with radiation doses equal to those tested in 4.2, only the radiation was delivered in two fractions. This may provide information on the biological effect, as fractionation gives time for damage repair (2.3.6.1).

The normalized PD-L1 signal for each individual experiment is presented in the top panel of Figure 26 for MOC1 cells and in Figure 27 for MOC2 cells. The bottom panel in Figure 26 and Figure 27 present the average normalized PD-L1 signal on MOC1 and MOC2 after two fractions, respectively. The doses tested and number of experiments are indicated in Table 3 and in the figure legends.

Table 3: ***Overview of experiments with two fractions of photon irradiation on MOC2 and MOC2 cells****, including the dates, radiation doses and additional comments. Two separate experiments were conducted on 03.04.2023, one in the morning and one in the afternoon. These experiments were performed separately and are considered as two independent experiments.*

Date	Dose [Gy]	Comments
13.02.2023	2+2 and 4+4	
20.02.2023		
13.03.2023		
03.04.2023 (morning)	6+6	
03.04.2023 (afternoon)		One control sample for MOC2 was lost
08.05.2023		The new flow cytometer Attune Nxt was used

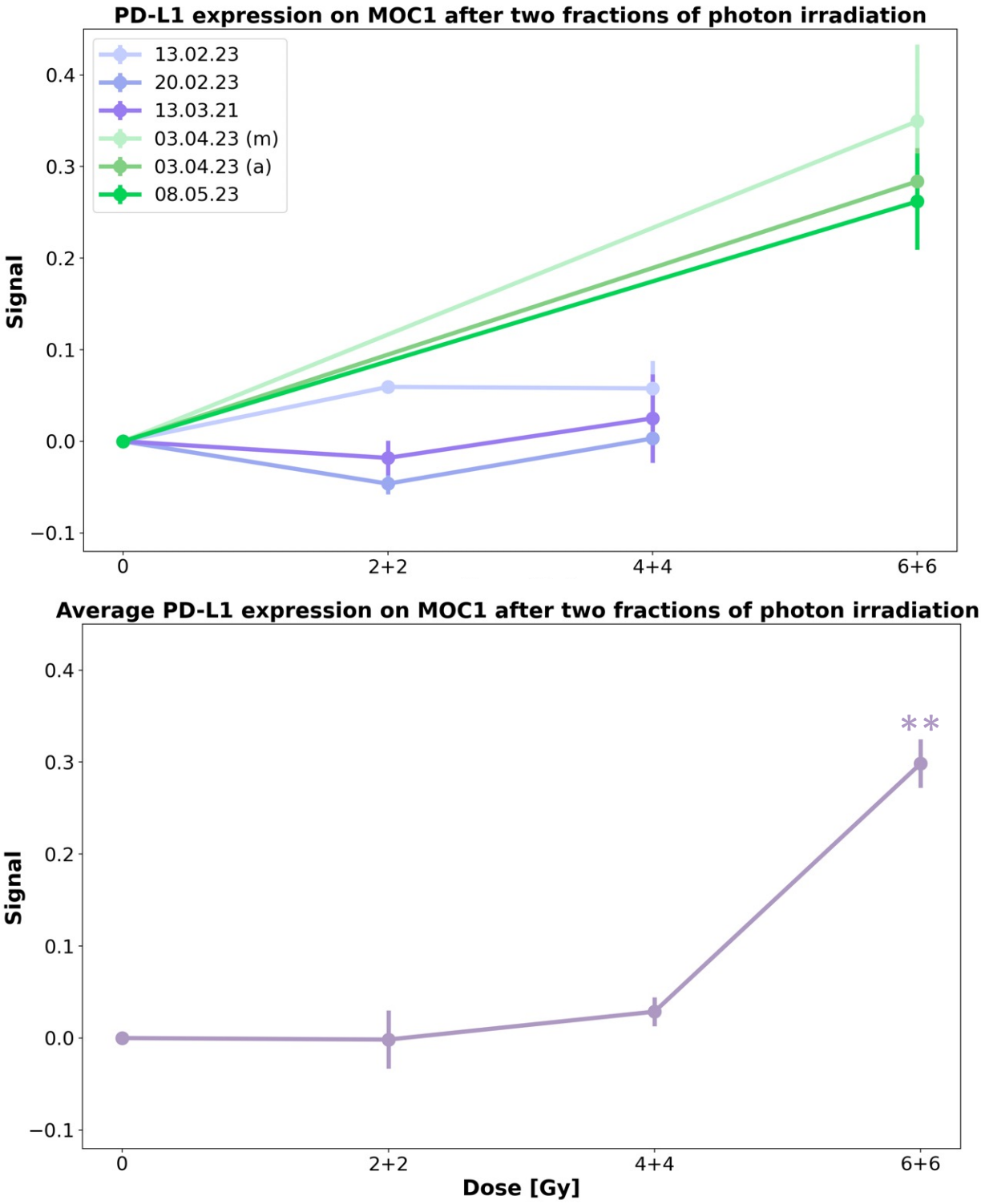

Figure 26: ***Normalized PD-L1 signal on MOC1 cells irradiated with two fractions of photon radiation*** ***The top panel*** *shows the normalized PD-L1 signal on MOC1 cells from each experiment with two fractions of photon irradiation, with 24 hours between each fraction. Three experiments were performed for each dose, with 2+2 Gy (total 4 Gy), 4+4 Gy (total 8 Gy) and 6+6 Gy (total 12 Gy). There were two experiments performed on 03.04.2023, one in the morning (m) and one in the afternoon (a,) and these are considered as two independent experiments. The error bar represents the standard error between the two biological replicates for each dose in the experiments. The raw data can be found in section 8.1.1.4 in the appendix.* ***The bottom panel*** *shows the average normalized PD-L1 signal on MOC1 cells after two fractions, and the error bars represent the standard error of the mean. The ** indicates a p-value below 0.01 from t-tests comparing the signal from irradiated to that from unirradiated cells. The p- and t-values generated from the t-test are stated in Table 27, appendix section 8.3.*

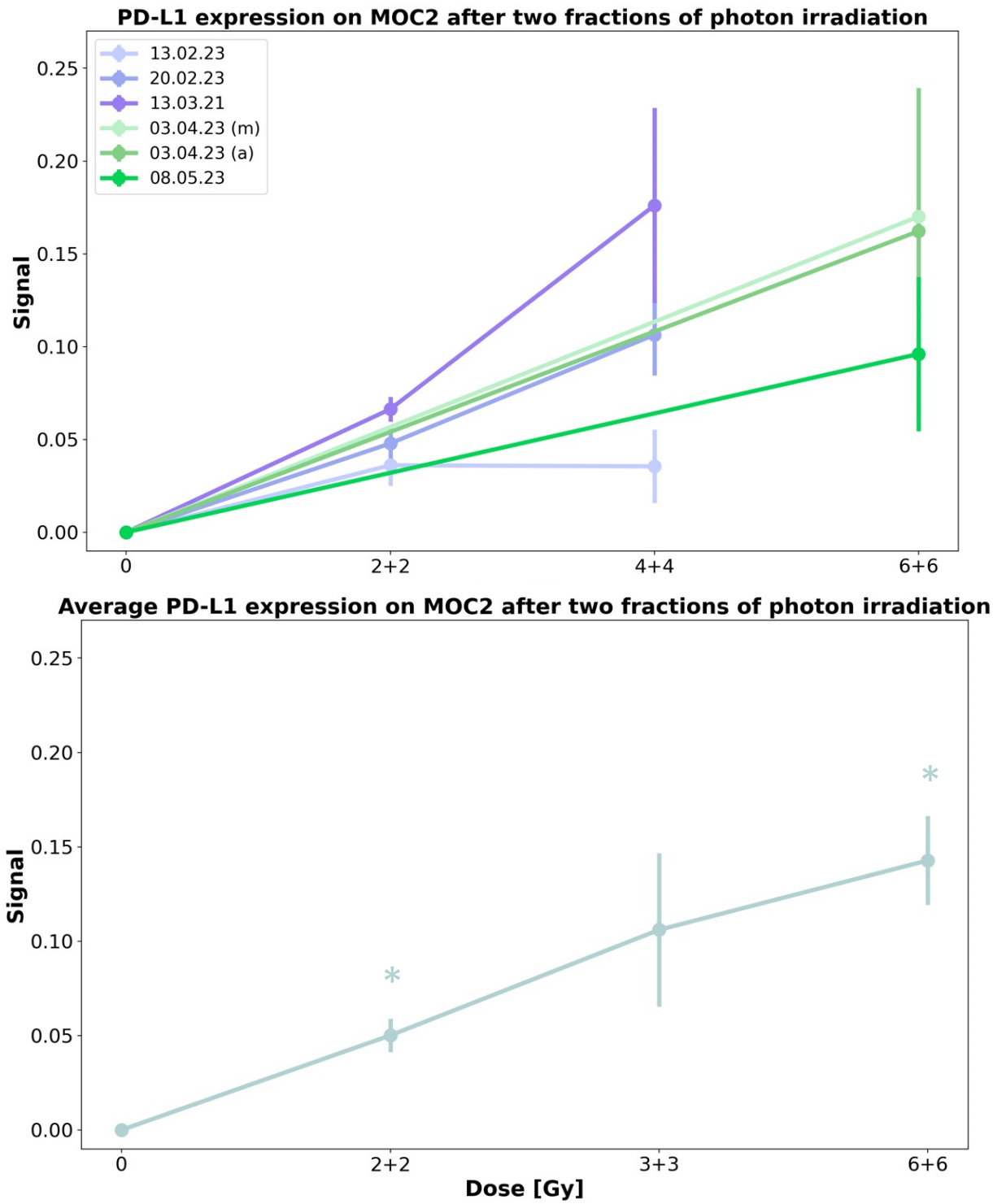

Figure 27: ***Normalized PD-L1 signal on MOC2 cells irradiated with two fractions of photon radiation.*** ***The top panel*** *shows the normalized PD-L1 signal on MOC2 cells from each experiment with two fractions of photon irradiation, with 24 hours between each fraction. Three experiments were performed with 2+2 Gy (total 4 Gy), 4+4 Gy (total 8 Gy) and 6+6 Gy (total 12 Gy). There were two experiments performed on 03.04.2023, one in the morning (m) and one in the afternoon (a), and these are considered as two independent experiments. The error bars represent the standard error between the two biological replicates for each dose in the experiments. The experiment from 03.04.23 (a) lost a biological replicate for the control during analysis. The raw data can be found in section 8.1.1.5 in the appendix.* ***The bottom panel*** *shows the average normalized PD-L1 signal on MOC2 cells after two fractions, and the error bars represent the standard error of the mean. The ** indicates a p-value below 0.01 from t-tests comparing the signal from irradiated to that from unirradiated cells. The p- and t-values generated from the t-test are stated in Table 28, appendix section 8.3.*

A comparison between the relative PD-L1 signal on MOC1 and MOC2 cells are presented in Figure 28. This comparison shows that there is an significantly increased signal of PD-L1 on the surface of MOC1 cells compared to MOC2 cells only for two fractions of 6 Gy.

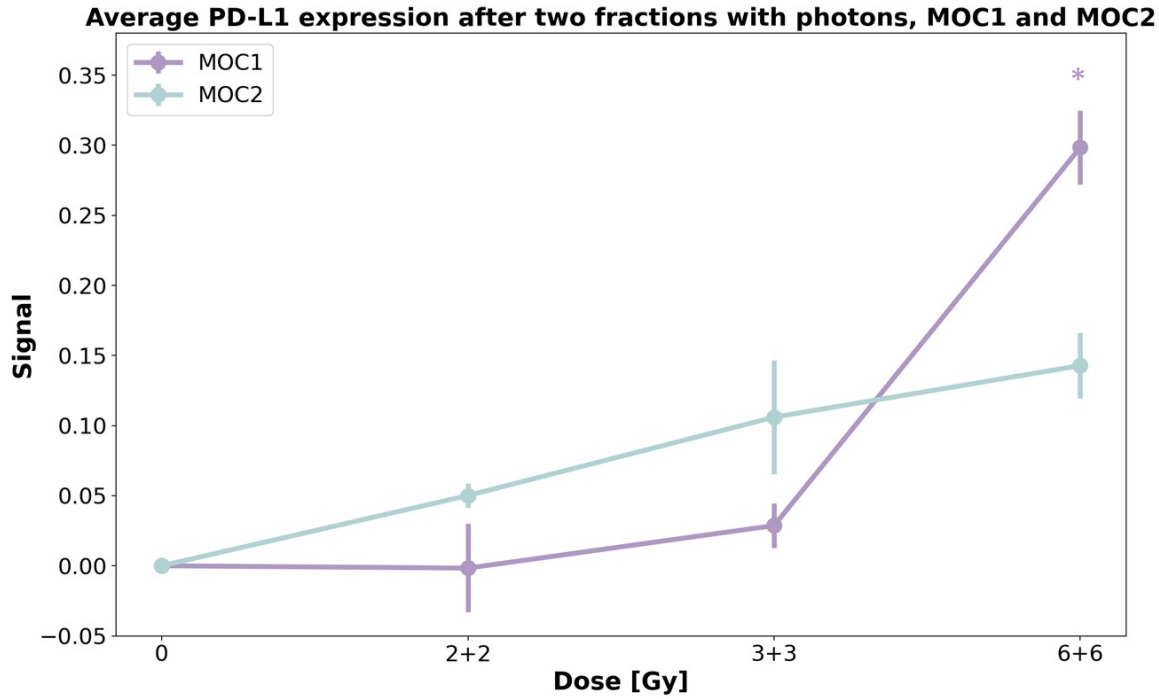

Figure 28: ***Comparison of PD-L1 signal between MOC1 and MOC2 cells after irradiated with two fractions of photon radiation (24 hours between fractions).*** *The average normalized signal of PD-L1 on the cell membrane of MOC1 and MOC2 cells with the doses 2+2 Gy (total 4 Gy), 4+4 Gy (total 8 Gy) and 6+6 Gy (total 12 Gy). Three experiments were performed for each dose. The error bars represent the standard error between of the mean. The raw data can be found in section 8.1.1.4 (MOC1) and 8.1.1.5 (MOC2) in the appendix. The * indicates a p value below 0.05 from t-tests comparing the signal from MOC1 and MOC2 cells. The p- and t-values generated from the t-test are stated in Table 29, appendix section 8.3.*

4.4 Comparison of PD-L1 signal on MOC1 and MOC2 cells after different fractionation schemes

To compare the biological effect on the PD-L1 immunosuppressor mechanism after the same total dose, delivered either in one or two fractions, the PD-L1 signal on MOC1 and MOC2 cells are plotted in Figure 29. The t-tests did not show any statistically significant difference in PD-L1 levels between the two fractionation schemes for either cell line.

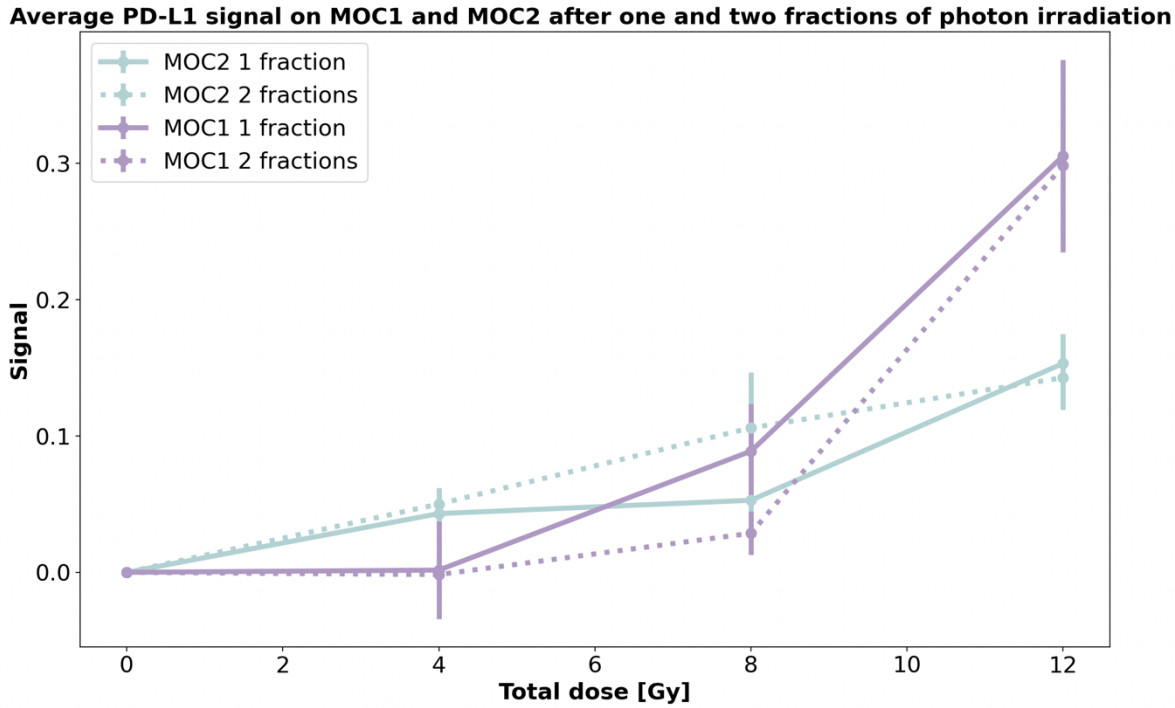

Figure 29: ***Comparison of the normalized PD-L1 signal on MOC1 and MOC2 cells after irradiated with one and two fractions of photon irradiation****. One fraction dose: 4 Gy (n=6), 8 Gy (n=6), 12 Gy (n=5), where 'n' represents number of experiments. Two fraction doses consist of three experiments with 2+2 Gy (total 4 Gy), 4+4 Gy (total 8 Gy) and 6+6 Gy (total 12 Gy). The error bars indicate the error of the mean. The raw data can be found in section 8.1.1.1 (MOC1, one fraction), 8.1.1.2 (MOC2, one fraction), 8.1.1.4 (MOC2 two fractions) and 8.1.1.5 (MOC2, two fractions) in the appendix. The p-values are stated in Table 33 (MOC1) and Table 34 (MOC2), appendix section 8.3.*

4.5 PD-L1 signal from MOC1 and MOC2 cells after three fractions of photon radiation

One of the most effective fractionation schemes in experiments investigating immunogenic response has been shown to be three fractions of 8 Gy (Lhuillier et al., 2019) (Dewan et al., 2009). We therefore wanted to test the PD-L1 expression for this dose regimen. The normalized PD-L1 signal from each individual experiment with after three dose fractions to the MOC1 and MOC2 cell line is shown in the left panel in Figure 30. The right panel in Figure 30 present the average normalized PD-L1 signal. The number of experiments is given in Table 4.

Table 4: ***Overview of experiments with three fractions of photon irradiation on MOC2 and MOC2 cells****, including the dates and radiation dose. Two separate experiments were conducted on 20.06.2023, one in the morning and one in the afternoon. These experiments were performed separately and are considered as two independent experiments. The flow cytometer Attune Nxt was used to analyze the samples.*

Date	Dose [Gy]
13.06.2023	8+8+8
20.06.2023 (morning)	
20.06.2023 (afternoon)	

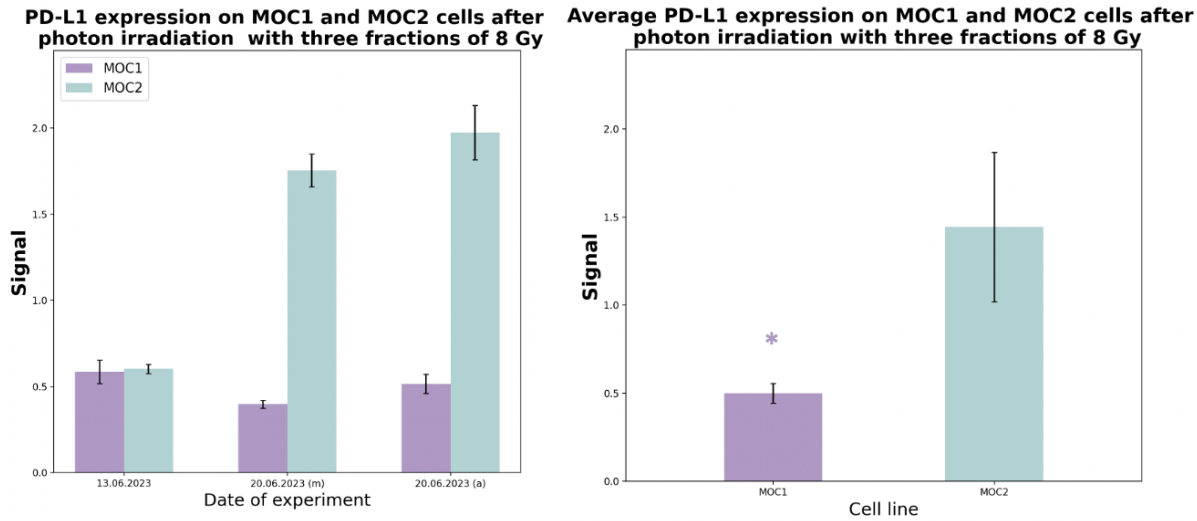

Figure 30: ***PD-L1 signal on MOC1 and MOC2 cells irradiated with three fractions of 8 Gy photon radiation, normalized to the controls.*** ***Left panel:*** *The normalized PD-L1 signal on MOC1 and MOC2 cells from each experiment with three fractions of photon irradiation. Three experiments were conducted with 8+8+8 Gy (total 24 Gy), with 24 hours between each fraction. There were two experiments performed on 20.06.2023, one in the morning (m) and one in the afternoon (a), and these are considered as two independent experiments. The error bar represents the standard error between the two biological replicates for each dose in the experiments. The raw data can be found in section 8.1.1.6 (MOC1), 8.1.1.7 (MOC2), in the appendix.* ***Right panel:*** *The average normalized PD-L1 signal on MOC1 and MOC2 cells after three fractions, where the error bars represent the standard error of the mean. The * indicates that the p-value is below 0.05 and ** indicates that the p-value is below 0.01 from t-tests comparing the signal from MOC1 and unirradiated MOC1 cells and MOC2 cells and unirradiated MOC2 cells. The p- and t-values generated from the t-test are stated in Table 30 (MOC1), Table 31 (MOC2) and Table 32 (MOC1 and MOC2), appendix section 8.3.*

The comparison of MOC1 and MOC2 (right panel Figure 30) indicates that there is an increased signal of PD-L1 on the surface of MOC2 compared to MOC1 after a three-fractionation scheme of 8+8+8 Gy. However, with an p-value = 0.093, due to the high uncertainties, there is not a statistically significant difference. The PD-L1 signal after three fractions is replotted in Figure 31 together with data for one and two fractions for comparison of the effects.

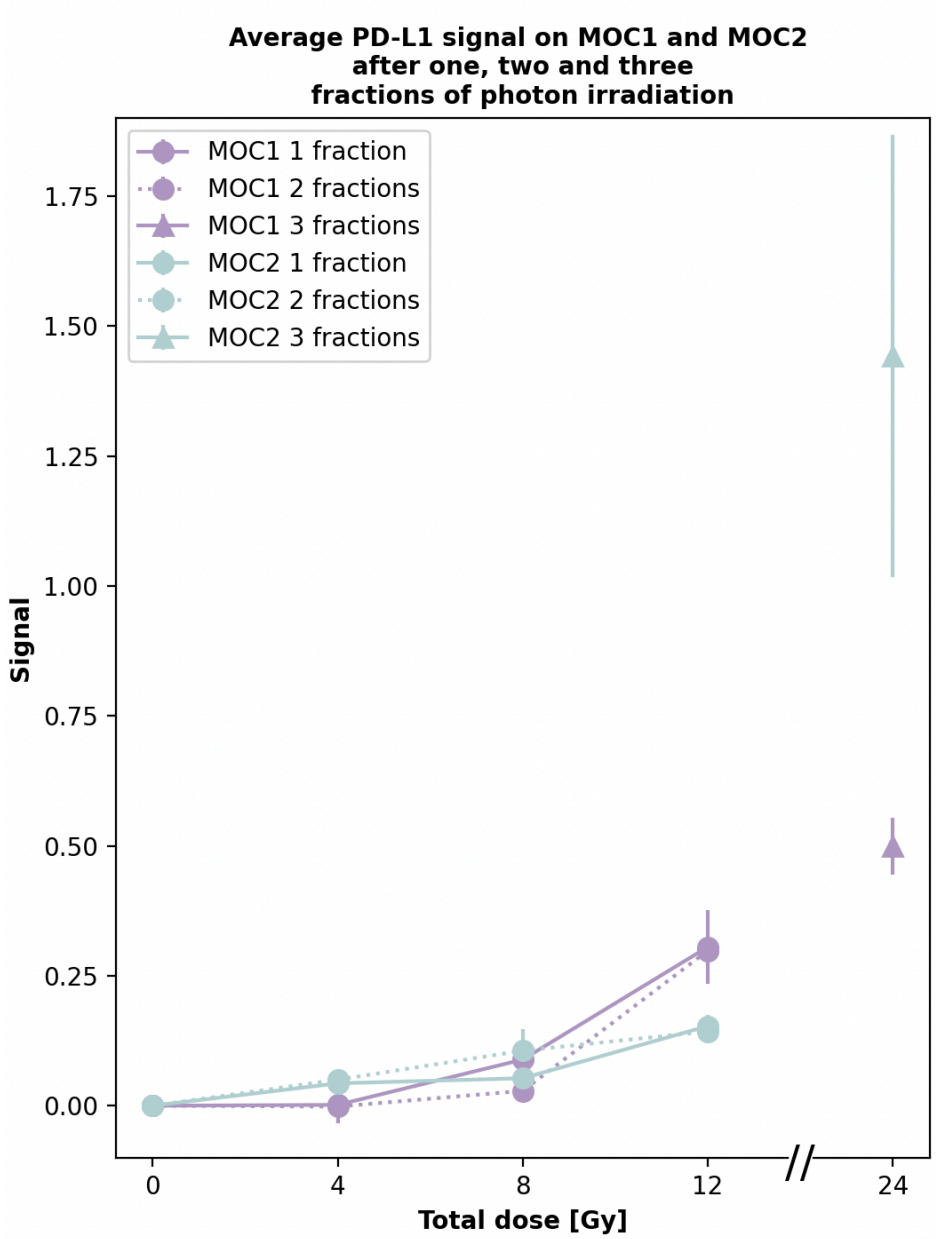

Figure 31: ***Comparison of the normalized PD-L1 signal on MOC1 and MOC2 cells after irradiation with one, two and three fractions of photon irradiation****. One fraction dose: 4 Gy (n=6), 8 Gy (n=6), 12 Gy (n=5), where 'n' represents number of experiments. Two fraction doses data consist of three experiments with 2+2 Gy (total 4 Gy), 4+4 Gy (total 8 Gy) and 6+6 Gy (total 12 Gy). Three fraction doses data consist of three experiments with 8+8+8 Gy (total 24 Gy). The error bars indicate the error of the mean. The raw data can be found in section 8.1.1.1 (MOC1, one fraction), 8.1.1.2 (MOC2, one fraction), 8.1.1.4 (MOC2 two fractions) and 8.1.1.5 (MOC2, two fractions), 8.1.1.6 (MOC1, three fractions), 8.1.1.7 (MOC2, three fractions) in the appendix.*

4.6 PD-L1 signal form MOC1 and MOC2 cells after one fraction of proton radiation

Due to cyclotron down time, only one experiment was performed for each cell line and an overview is given in Table 5. MOC1 and MOC2 cells were irradiated with 4 and 8 Gy, when positioned in front of and in the distal end of the Bragg peak. The normalized PD-L1 signals are plotted in Figure 32.

*Table 5: **Overview of experiments with proton irradiation**, including the dates, radiation doses and position in the Bragg peak. MOC1 and MOC2 cells were irradiated with one fraction of 4 Gy and 8 Gy of proton radiation, positioned in front of the Bragg peak (P1) and in the distal end of the Bragg peak (P5).*

Date	Dose [Gy]	Position in proton depth dose curve	Cell lines
08.09.2022 (morning)	4 and 8	P1	MOC1
08.09.2022 (afternoon)		P5	
14.09.2022 (morning)		P1	MOC2
14.09.2022 (afternoon		P5	

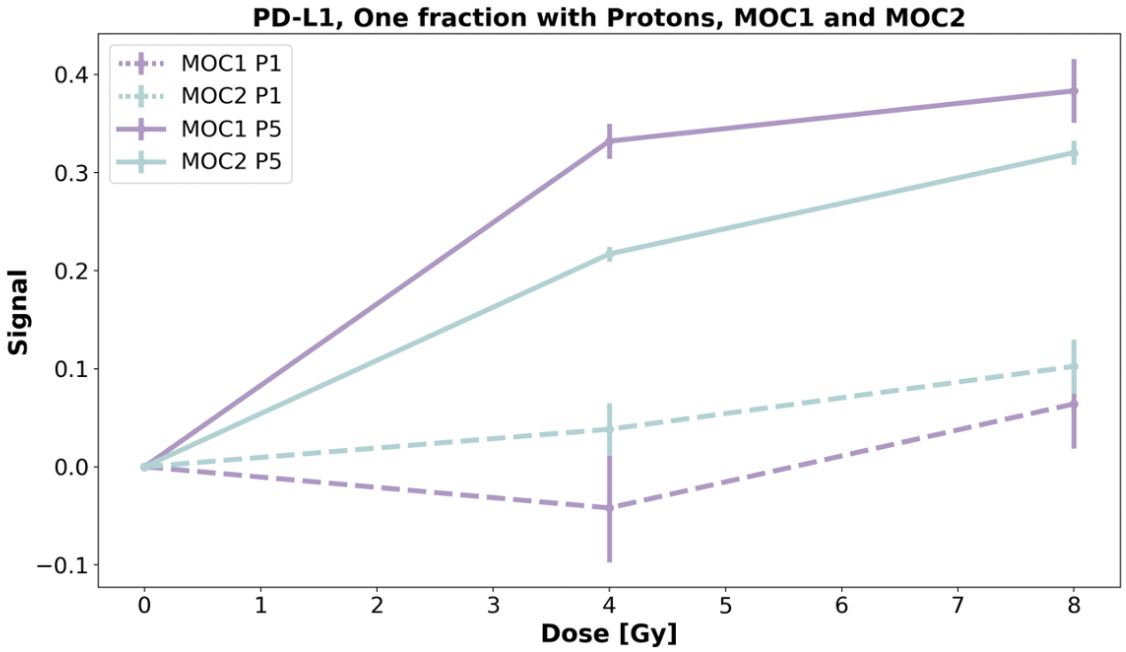

*Figure 32: **Comparison of normalized PD-L1 signal between MOC1 and MOC2 cells after irradiated with one fraction of proton radiation**. The normalized PD-L1 signal on MOC1 and MOC2 cells after one fraction of proton irradiation with the doses 4 Gy and 8 Gy, in front of the Bragg peak (P1) and in the distal end of the Bragg peak (P5). The error bar represents the standard error between three biological replicates. The raw data can be found in section 8.1.1.8 in the Appendix.*

The solid lines in Figure 32 represent the normalized PD-L1 signal on MOC1 and MOC2 cells irradiated in the distal end of the Bragg peak. The PD-L1 signal was higher in both MOC1 and MOC2 cells in this position, compared to the dotted lines representing the signal from MOC1 and MOC2 cells irradiated in front of the Bragg peak.

4.7 Relative unspecific binding of isotype antibody on MOC1 and MOC2 cells and cell size

Punnanitinont et al proposed a correlation between unspecific binding of isotype antibodies and cell size (Punnanitinont et al., 2020). Only data from the Attune Nxt flow cytometer were possible to use to investigate this correlation. The average normalized unspecific binding of the isotype antibody (I_s) in MOC1 and MOC2 cells are illustrated in Figure 33.

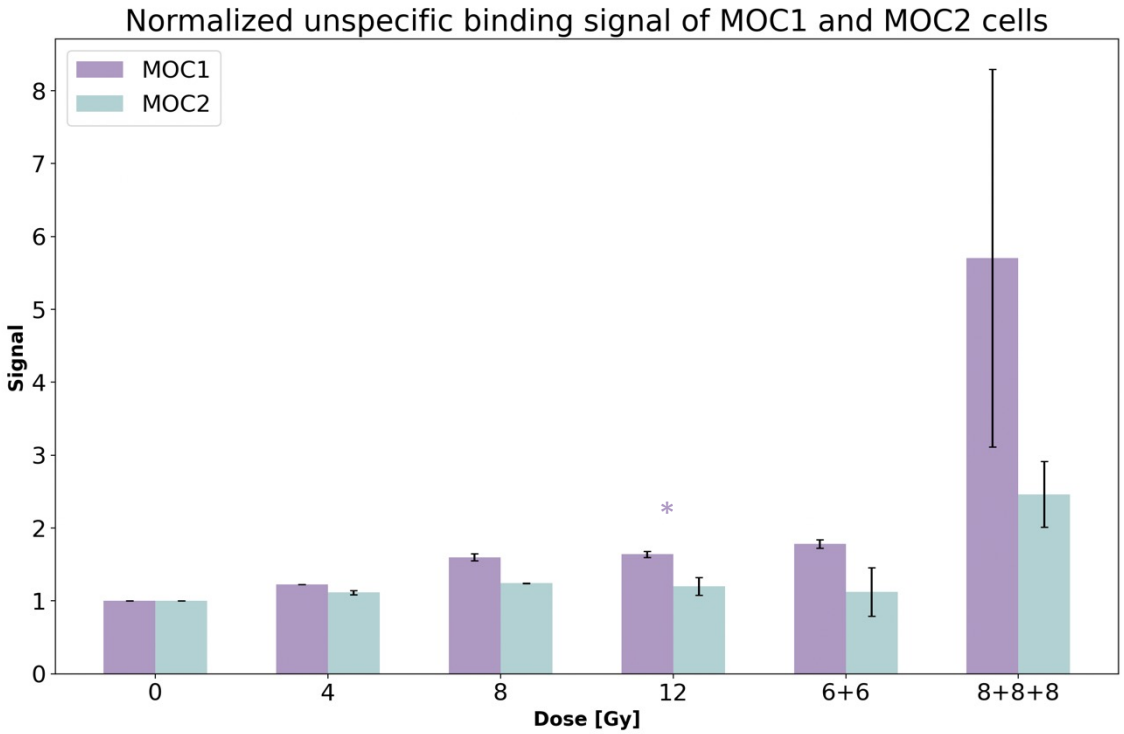

Figure 33: ***The average of the relative unspecific binding on MOC1 and MOC2 cells.*** *The cells were irradiated with one fraction of 4 Gy (n=5), 5 Gy (n=3), 8 Gy (n=5), 10 Gy (n=3) and 12 Gy (n=5), where 'n' represents the number of experiments. The error bars in the plot represent the standard error of the mean. The raw data can be found in section 8.1.1. The * indicates a p-value below 0.05 between the unspecific signal for MOC1 and MOC2. The p- and t-values generated from the t-test are stated in Table 38, appendix section 8.3.*

The sizes of irradiated MOC1 and MOC2 cells were examined by using the forward scatter (FSC) signal from the flow cytometer. In section 2.6.1, it was discussed that the FSC signal detected by the flow cytometer is dependent on the size of the cell. The forward scatter signal detected for unirradiated MOC1 and MOC2 cells shows that the unirradiated MOC2 cells are larger in size compared to MOC1, illustrated in Figure 34.

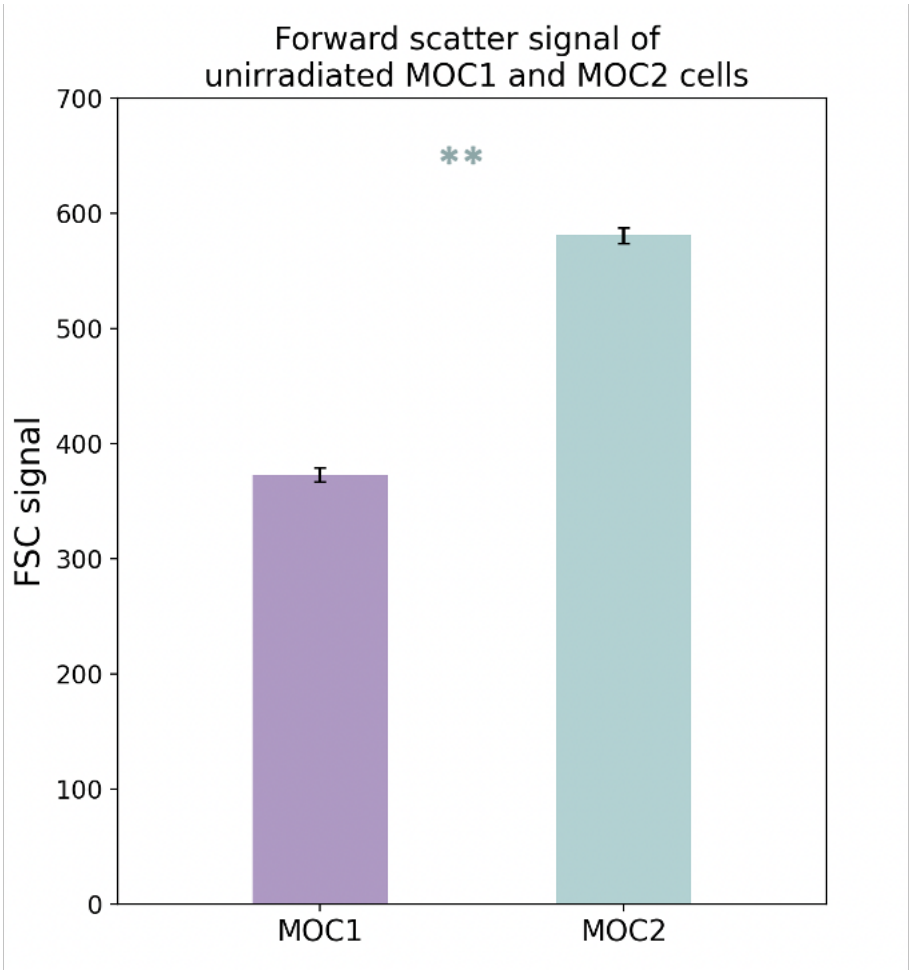

Figure 34: ***The forward scatter (FSC) signal detected for unirradiated MOC1 and MOC2 cells****. The FSC gives information on the size of the cell. The values are an average value of 16 analyzed samples for MOC1 and MOC2 cells. The error bars represent the standard error of the mean. The raw data can be found in section 8.1.2 in the Appendix. The ** indicates a p-value below 0.01, between the cell size for unirradiated MOC1 and MOC2 cells (p-value << 0.01).*

The FSC signal from each irradiated sample was first normalized against the control cells, then averaged across corresponding doses. Figure 35 shows the alteration in size for MOC1 and MOC2 cells in response to radiation doses, and shows that irradiated MOC1 cells increase in size, and have a higher increase compared to MOC2 cells.

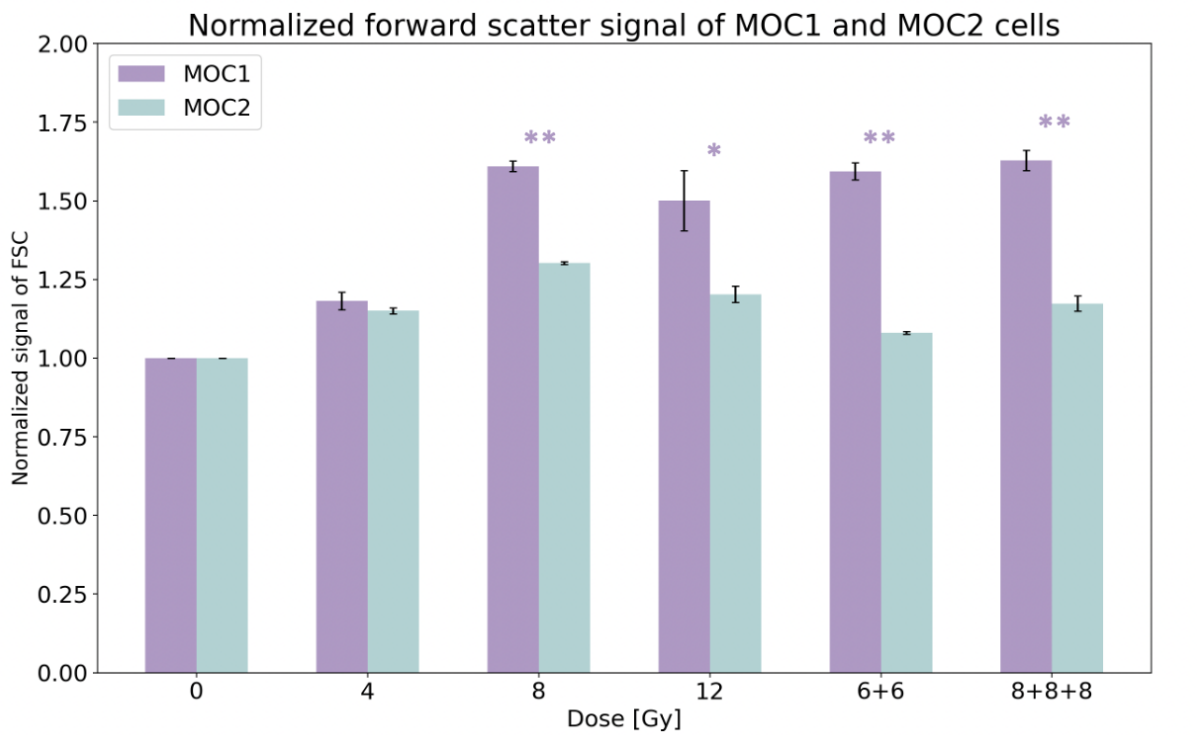

*Figure 35: **The normalized forward scatter (FSC) signal detected for MOC1 and MOC2 cells**. The cells were irradiated with one fraction of 4 Gy (n=4), 8 Gy (n=4), and 12 Gy (MOC1 n=11, MOC2 n=12), two fractions of 6 Gy (n=4) and three fractions of 8 Gy (n=12), where 'n' is number of samples. FSC gives information on the size of the cell. The error bars represent the error of the mean. The raw data can be found in section 8.1.2 in the Appendix. The * indicates a p value below 0.05 and ** indicates a p-value below 0.01 from t-tests comparing the forward scatter signal from MOC1 and MOC2 cells. The p- and t-values generated from the t-test are stated in Table 37, appendix section 8.3.*

4.8 PGE_2 secreted from MOC1 and MOC2 cells

The other immunosuppressor mechanism investigated in this thesis was the COX-2/PGE_2 pathway. To explore this, the concentration of PGE_2 in medium from irradiated cells were determined using ELISA (2.6.2).

4.8.1 PGE_2 standard curve

In the ELISA assay, a serial dilution of PGE_2 standard was added to one row of the sample plate. This dilution series was used to establish the standard curve, which represents the correlation between the optical density (OD) measured in each well and the concentration of PGE_2 in the sample. The OD values obtained from the standard wells were fitted to a four-parameter logistic (4PL) curve fit, given in equation 15. The parameters fitted to the experimental data were a = 0.422, b = 1.235, c = 852.754, and d = 0.003, with an R^2 value of 0.996. The standard curve is presented in Figure 36. The OD values from the ELISA measurements are plotted as dots and the model generated from the 4PL curve fit is plotted as a dotted line.

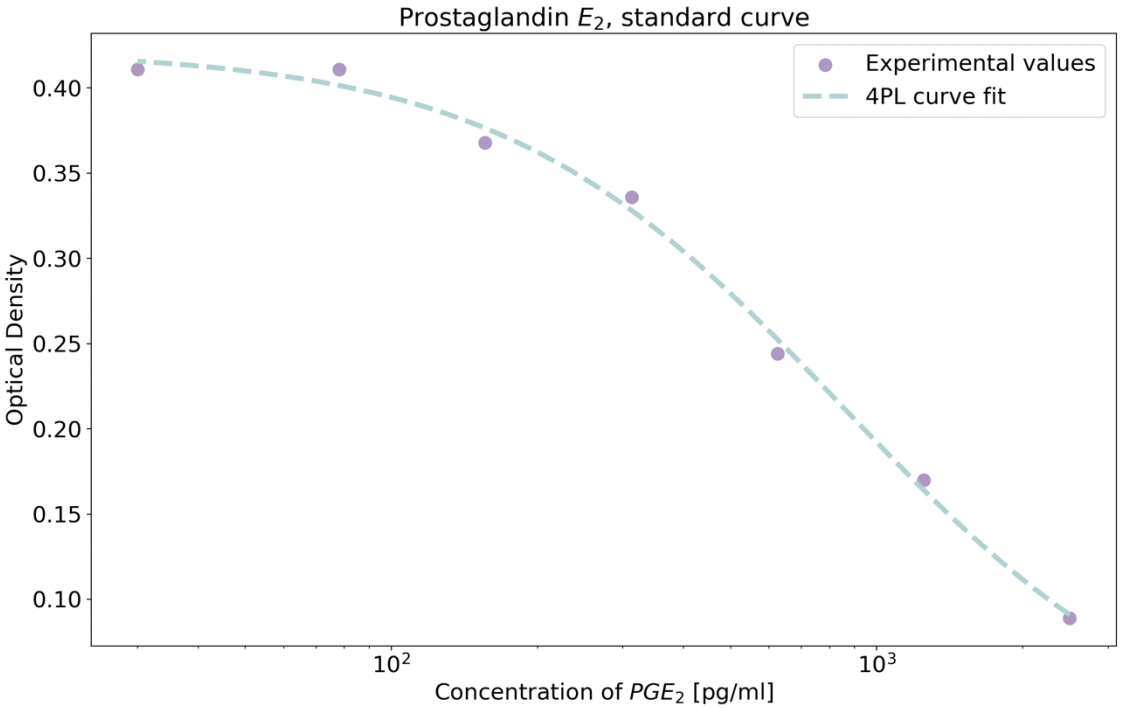

*Figure 36: **The standard curve generated from a serial dilution of PGE_2 standard in the ELISA assay**. The dots represent the experimental values, and the dotted line represents the model used to fit the data (Table 23). The data were fit to a four-parameter logistics curve fit with the values a = 0.422, b = 1.235, c = 852.754, and d = 0.003, with an R^2 value of 0.996. This standard curve is essential for quantifying the corresponding concentration of PGE_2 in the samples based on the detected optical density in the ELISA measurements.*

4.8.2 Concentration of PGE_2 detected in medium samples

The samples tested were collected from dishes containing MOC1 or MOC2 cells, 24 hours after irradiation. Table 6 provide an overview of the samples used in the ELISA analysis, including the date of sampling and the radiation doses. An overview over the placements of the samples, and the raw data from the analysis are given in Figure 39 and Table 23 in appendix section 8.2.1. Due to observations that PD-L1 signal increased mainly at the higher doses, the medium from these doses were prioritized for analysis, except for one experiment where the cells were irradiated with 4 Gy. Each dose point is represented by three experiments with two biological replicates each. Due to both time and cost constraints, only one ELISA analysis was performed.

The concentration of PGE_2 secreted by unirradiated MOC1 and MOC2 cells were 1262 [pg/ml] and 3314 [pg/ml] respectively, illustrated in Figure 37, showing that MOC2 cells secrete more PGE_2 compared to MOC1 cells (p-value = 0.00002).

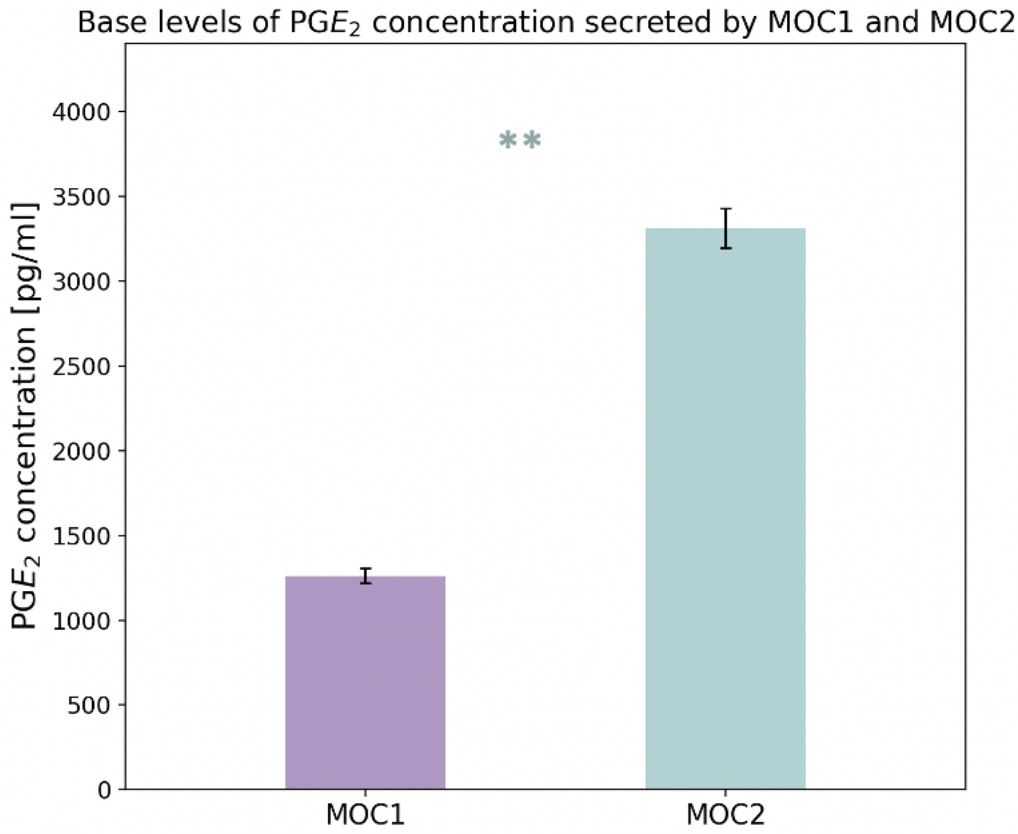

Figure 37: ***The concentration of PGE_2 secreted by unirradiated MOC1 and MOC2 cells.*** *The values are an average value of 18 analyzed samples for MOC1 and 17 analyzed sampled for MOC2 cells. The error bars represent the standard error of the mean. The raw data are given in Table 23 in appendix section 8.2.1. The ** indicates a p-value below 0.01 from a t-test comparing PGE_2 secreted from MOC1 and MOC2 cells.*

Some samples were discarded from the analysis due to their OD values being too high and exceeding the range of the standard curve. Specifically, the following samples were discarded:

1. Two biological replicates for MOC1 cells irradiated with 12 Gy, sampled on 13.06.23
2. Two biological replicates for MOC2 cells irradiated with 10 Gy sampled on 13.06.23
3. Two biological replicates for MOC2 cells irradiated with 8 Gy, sampled on 28.05.23
4. One biological replicate for a control sample of MOC2, sampled on 19.06.23 (a)

Discarding these samples was necessary to ensure the accuracy and reliability of the analysis. Despite these exclusions, the remaining data provides a good basis for analysis of MOC1 and MOC2 cells production of PGE_2 after different radiation doses.

Table 6: ***An overview of the samples of the medium used in the ELISA analysis.*** *The samples were collected from dishes with MOC1 or MOC2 cells, 24 hours after irradiation. The dates, doses and further comments for each experiment is given. There were conducted two experiments on 19.06.23 and 20.06.2023, one in the morning (m) and one in the afternoon (a). These were four separate experiments and are considered as independent. Some samples had to be discarded, since they had an optical density that exceeded the standard curve.*

Experiment	Date when medium was sampled	Dose [Gy]	Comments
E_1	13.06.2023	10, 12 and 8+8+8	The two biological replicates for 12 Gy MOC1 were discarded.
E_2	19.06.23 (m)	10 and 12	
E_3	19.06.23 (a)	10 and 12	One biological replicate for the control value for MOC2 was discarded. Two biological replicates for MOC2 cells irradiated with 10 Gy were discarded.
E_4	28.05.2023	4 and 8	The two biological replicates for MOC2 irradiated with 8 Gy were discarded
E_5	11.06.23	8	
E_6	18.06.23	8	
E_7	20.06.2023 (m)	8+8+8	
E_8	20.06.2023 (a)	8+8+8	

The optical density values obtained from the ELISA measurement were processed as follows: First, all samples were corrected for the background detected from the non-specific binding (NSB) wells, then the OD values from each sample were averaged between the biological replicates within each experiment. Next, these values were averaged with the corresponding doses. Then, the standard curve was used with these values to determine the corresponding PGE_2 concentration. Finally, the values were normalized against the control samples. The normalized PGE_2 concentrations are plotted in Figure 38. This approach was chosen as there was only one ELISA plate used in the analysis excluding assay related variations. The error bars indicated in Figure 38, were determined by using the standard error from the mean of the OD measurements for the different experiments with the assumption that the inter-experiment error was so much larger than the error for the curve fitting of the calibration data that the latter could be ignored. This was done by adding and subtracting the standard error to the mean OD, before using the standard curve to calculate the corresponding concentration. The higher and lower concentrations calculated give an indication of the potential error of the concentration values.

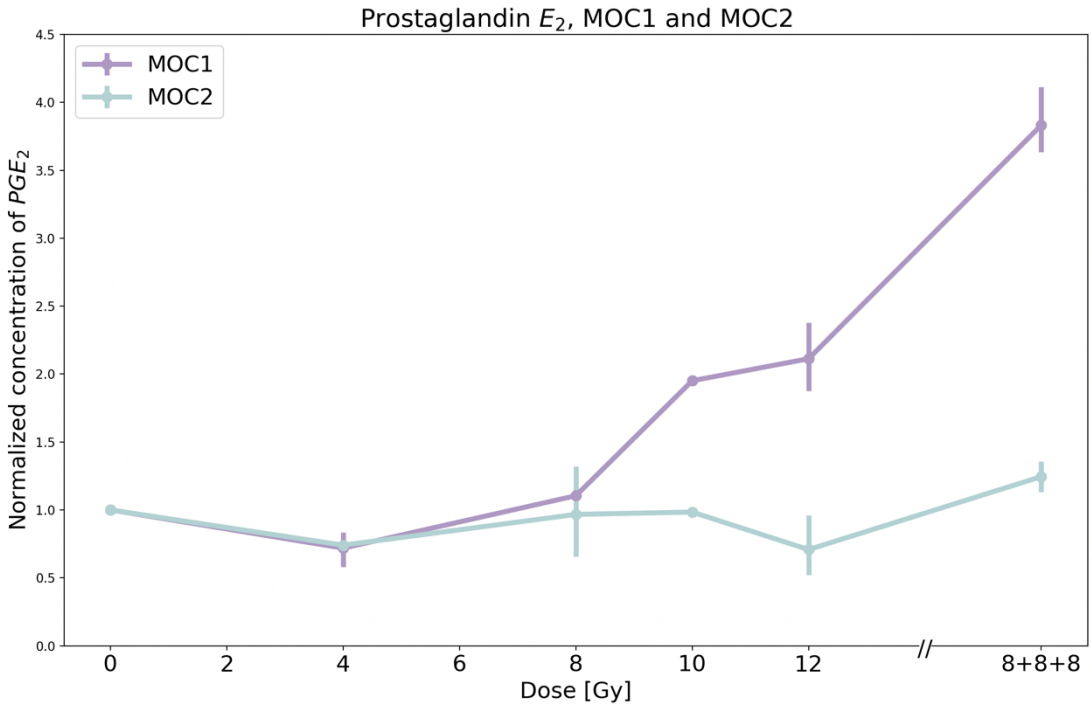

*Figure 38: **The normalized concentration of PGE_2 in the medium for irradiated MOC1 and MOC2 cells**. The doses of one fraction photon radiation were 4 Gy (n=1), 8 Gy (n=3), 10 Gy (n=3) and 12 Gy (n=2) for MOC1 and 4 Gy (n=1), 8 Gy (n=2), 10 Gy (n=2) and 12 Gy (n=3), where 'n' is the number of experiments. The three-fractionation scheme of photon radiation tested was 3x8 Gy. For both MOC1 and MOC2 cells, there were retrieved samples from three independent experiments. The error bars represent the concentrations calculated from the OD values added and subtracted with the standard errors. The raw data are given in Table 23 in appendix section 8.2.1.*

Figure 38 shows that the increase in PGE_2 concentration was higher for MOC1 compared to MOC2, in response to doses above 8 Gy. Due to the way that the signal was calculated, and the fact that it was all performed in one experiment, it was not possible to perform a hypothesis test. The highest PGE_2 concentration was measured for MOC1 cells after three fractions of 8 Gy, where the concentration was 6475.44 [pg/ml] compared to MOC2 cells with 5566.5 [pg/ml].

5 Discussion

5.1 Discussion of Method

5.1.1 Cell culture method

When performing biological experiments, there always exists a certain level of uncertainty. Numerous factors beyond the treatment itself can affect the results. In addition, cells themselves are not always predictable. The equipment used can introduce data uncertainty. In this thesis, two different flow cytometers were used, which could potentially yield different results. Manual performance of the assay will also contribute to the variability, and even within strict protocols, errors and variations can occur. It is important to acknowledge these potential errors and variations during data analysis and consider the uncertainties alongside the results.

While cells are the fundamental units of life, their ability to represent the real tumor environment is limited. Tumors and their environment are intricate systems shaped by numerous factors and interactions that are challenging to replicate within in vitro assays. This limitation is especially pronounced in experiments aiming to investigate immune responses. The immune system is a complex and delicately balanced system, characterized by complex interactions among numerous molecules and the recruitment of immune cells. This is best represented through mouse models, where the complete immune response can be assessed. However, in vitro models can be valuable in studying isolated cellular mechanisms and responses.

The focus of this thesis is to examine the fundamental characteristics of two different mouse tumor models in vitro. This analysis occurs within a controlled environment without any external influence of the immune system. This can provide information on the influence of irradiation on molecular responses and possibly contribute to a more comprehensive understanding of the complex tumor environment.

5.1.2 PD-L1 measurements and analysis

The PD-L1 signal on the cell membrane was measured by flow cytometry. In the following subsection, the limitations and features of the analysis that may influence the data are discussed.

5.1.2.1 Flow cytometer

Flow cytometry is an analytical method with many important applications. However, potential pitfalls exist that can lead to inaccurate, misleading, and contradictory results. Understanding the factors that influence the outcomes and knowing how to monitor and control them are crucial. Several features can influence the results obtained from flow cytometry analysis.

Fluidic system

Maintaining the instrument's fluidics system in optimal condition is essential. Accumulated debris can induce turbulence, increasing signal variability. If cells from the previous run still are in the tubing system, they may generate signals that affect the subsequent analysis. The Attune NxT flow cytometer (Thermo Fisher Scientific, Germany) was equipped with an effective system for cleaning between samples, to minimize the errors caused by this factor. The Accuri C6 flow cytometer (BD Biosciences, USA) did not have an automatic flushing procedure, but manual flushing was performed between each sample.

Flow rate

Flow rate influences the cell suspension velocity; a higher flow rate can lead to turbulence and increased variation in signal intensity, while lower flow rate increases the acquisition time. In our case, there was a need for as many events as possible within a reasonable amount of time as we work with live cells. Acoustic focusing was implemented in the new Attune flow cytometer, which allowed for a higher flow rate without sacrificing data quality. The Attune could easily register 50,000 events in the same time as the old Accuri instrument could register 10,000. Consequently, samples analyzed with Attune offered a stronger signal base for analysis.

Photodetector voltage

Analytical factors also contribute to accumulating uncertainties. The final image produced depends on the acquisition settings. These settings must be established before analysis and cannot be altered during the process. The Accuri flow cytometer was an analog device with fixed acquisition settings, while the Attune had a digital system allowing user-set acquisition settings. The electric signal intensity establishes the position of the population of interest on the plot axes. On the first experiment analyzed on the Attune, the photodetector voltage was set to a lower voltage, which was reflected in the data. On the second run, the voltage was increased resulting in much higher signals, making the signal more sensitive to differences (Tzanoudaki & Konsta, 2023).

Gating

Finally, gating plays a crucial role in achieving high-quality and reproducible results. Consistency in gating strategy is essential. The gating process cleans the data by excluding non-single cells and debris (with lower forward scatter values) and dead cells detected by viability dyes (such as PI). While the gating strategy remained consistent throughout experiments, software differences between the two flow cytometers could result in minor variations.

5.1.2.2 The cell preparation assay for the flow cytometry

Each irradiated dish with cells was divided into two samples. One sample was incubated with the primary antibody, while the other was incubated with an isotype control. This control functioned as an internal reference to assess non-specific signals from the cells in response to irradiation. Even though this type of control is widely used, there are some limitations associated with it. One limitation is that the individual antibody conjugate has various levels of background staining. This variance is dependent on the specificity, concentration, and fluorophore-antibody ratio, among others. Consequently, finding an isotype control that precisely mirrors the background staining of the primary antibody can be challenging, and could lead to errors when being used as a control. Even though there are some problems with this internal control, it is still used in most experiments using fluorochrome conjugated primary antibodies.

To quantify the presence of PD-L1 on cell surfaces, a direct immunostaining flow cytometry analysis was conducted. Cells were incubated with fluorochrome-conjugated anti-PD-L1 antibodies. This one-step staining procedure involved directly staining live cells with the antibody, as PD-L1 is located on the cell surface. Fixating the cells would have damaged the cell surface receptors. Given this, the cells were kept alive and not fixed prior to staining.

It is worth noting that using cultured cells with this assay and analysis is only one of the possible methods to investigate PD-L1 on the cell surface. PD-L1 analysis can also be performed after in vivo irradiation either by flow cytometry on cells from grinded tumors (Wu et al., 2016) or by immunohistochemistry on fixated tissue sections.

In this thesis, the analysis was performed 24 hours after the total dose was delivered. This was based on protocols found in the literature. However, other studies have found the highest effect of radiation induced PD-L1 signal on in vitro cells to be 48 hours (bladder cancer cells HT1197 after 6 Gy, lung cancer cells A549 after 10 Gy and osteosarcoma cells U2OS after 10 Gy) after the dose was delivered (Sato et al., 2017; Wu et al., 2016). In hindsight, it would have been interesting to do a time analysis of the induction of PD-L1 and compare the PD-L1 signal on MOC1 and MOC2 cells at 48 and 72 hours post irradiation, to see at what timepoint PD-L1 has the highest signal.

Seeding cells in dishes by confluence is the standard procedure at BMF for these kinds of experiments. While some slight variations in total number of cells can emerge between experiments, it is important to note that within each experiment, the cell number is close to the same as all the dishes were seeded from the same cell suspension. For better reproducibility, it would have been ideal to seed cells based on cell number rather than confluence in the dishes as was performed. This variation in cell seeding could introduce diversity between experiments in terms of both number of cells analyzed and cell staining. Implementing this adjustment may have contributed to a more standardized methodology

across experiments, simplifying the replication process for other researchers by providing precise cell seeding numbers instead of relying on confluence. However, the consistency within each experiment is high, which is the most important as we look at normalized values from each experiment.

5.1.2.3 Increase of signal unrelated to PD-L1 antibody binding

In both MOC1 and MOC2 cell lines, there was an observable increase in PD-L1 signal on the cell surface following irradiation. However, it is important to note that there was also a general increase in non-specific binding on the cells. This phenomenon is evident in Figure 33, where the average fluorescent signal from the isotype control samples increased in a dose-dependent matter.

This finding suggests that irradiated cells have a higher capacity for binding antibodies in comparison to non-irradiated cells. This effect has been observed in other studies as well. For instance, a study by Punnanitinont et al. demonstrated similar results in irradiated cancer cells. In their study, they noticed that irradiated cancer cells (8 different human cancer cell lines) had a larger cell surface area compared to non-irradiated cells, potentially contributing to the higher non-specfic antibody binding observed (Punnanitinont et al., 2020).

Increased cell surface of MOC1 and MOC2 cells

On the basis of this observation, an analysis of cell size was done on the MOC1 and MOC2 cells after different doses of irradiation. Consistent with the findings of Punnanitinont et al. both MOC1 and MOC2 cells showed a statistically significant increase in cell surface after irradiation. The increase in size normalized to the controls was greater for MOC1 cells compared to MOC2 cells (Figure 35). This aligns with the trend discovered for the non-specific binding.

Punnanitinont et al. discovered that the cells had larger nuclei, and were multi-nucleated, which is expected with radiation induced cell cycle arrest. By analysing the DNA content with fluorescence microscopy confirmed that the radiation treatment had induced G_2/M arrest. This was not confirmed for the analyzed MOC1 and MOC2 cells due to time constraints but could be a possible explanation for the larger size compared to unirradiated cells. The data would then indicate that more MOC1 cells were arrested in G_2/M phase compared to MOC2, as there was a considerable difference in average size between the two cell lines. MOC2 cells have been identified as a more aggressive cancer type in comparison to MOC1, and MOC2 cells grow faster and show a tendency to metastasize when implanted in mice (Rykkelid, 2023). These aggressive features might be caused by suppression of genes that would normally induce cell cycle arrest in MOC2. This is a typical cancer cells characteristic, as discussed in section 2.4, and could be a reason for MOC2 cells to continue through the cell

cycle despite radiation induced damage. This might explain why MOC2 cells do not show a comparable increase in cell surface after radiation, as was observed with MOC1 cells.

Autofluorescence

The higher observed signal may not only be caused by an increase in non-specific binding but also an increase in autofluorescence. Autofluorescence is fluorescence that originates from molecules in the cells themselves and has been observed to increase in various cell lines after radiation (Schaue et al., 2012), also in our group (Thingstad, 2019) (Ruud, 2020). This effect was discovered while attempting to quantify calreticulin on the cell surface of A549 and T98G cells after irradiation, also using live cells. Initial data gave unreliable results, deviating from the expected results. Further testing revealed that this was caused by an increase in the autofluorescence and not the antibodies, which overshadowed the effect investigated.

While this effect was not explored further in this thesis, it could be very insightful to investigate how large of an effect this had for the MOC1 and MOC2 cells, and how much of the signal increase was caused by this. The autofluorescence could be tested by irradiating MOC1 and MOC2 cells with the same doses and analyze them with the same laser as in the PD-L1 assay, in the flow cytometer without anti-PD-L1 or isotype control. This would give the increase in signal only due to autofluorescence. However, the use of isotype control also corrects for autofluorescence.

The increase in non-specific signal by irradiation could be caused by various factors, such as changes in cell membrane properties induced by radiation, the increased size due to cell cycle arrest in G_2 or by an increasing autofluorescence of the cells. If the observation is due to actual increase in binding on the surface, radiation-induced alterations might lead to more opportunities for antibody binding. It is very interesting to see that even though we do not know the exact reason for the increase in non-specific binding, the effect is different between the two cell lines, where the increase is higher for MOC1 compared to MOC2 cells. While these findings highlight the complexity of the cell's response to radiation, they also emphasize the importance of accounting for non-specific binding and autofluorescence when interpreting results related to PD-L1 signal and immunomodulatory effects. However, using an isotype control can correct for both of these effects. This may also have implications for the PD-L1 signal, that is further discussed in section 5.2.1.

5.1.3 PGE_2 measurements and analysis

Due to both time and cost constraints, it was only possible to perform the ELISA assay once. The protocol recommended testing each sample in duplicate (each sample is analyzed in two wells), accounting for potential human errors and analytical variations. However, given the limitations, it was prioritized to have a larger sample set over duplicated samples. While this approach gives a larger dataset, it came at the expense of potentially sacrificing some reliability.

The documentation provided from the manufacturer, gives insight into the intra-assay precision. The evaluation included testing three samples of known concentration twenty times on a single plate to assess precision. The observed coefficient of variation was 9%, 5%, and 6.1% for the mean concentrations 234, 895 and 1456 [pg/mL], respectively. These variations highlighted the assays' variability, and given the absence of duplicated samples, an alternative strategy was used to calculate the concentrations in the samples.

In the performed analysis, optical density data for each control and dose were averaged across replicated experiments. These averaged optical density values were then matched to the standard curve to determine the corresponding concentrations. Lastly, the concentrations were normalized to the control, forming the basis for the plot in Figure 38. An alternative method that may be more correct in other situations, involved calculating the concentration for individual samples, normalize the concentration to each experiment's control, and then averaging across experiment repetitions. This alternative method was explored and illustrated in Figure 40 for MOC1 and Figure 41 for MOC2 cells and combined in Figure 42 (Appendix 8.2.2). However, this method resulted in considerable variability and significant uncertainties, most likely due to the variation in the assay itself. Consequently, to minimize the impact of analytical variations, it was decided to average the optical density values for samples in the corresponding experiments that were subjected to the same treatment.

Within the analysis, seven wells had to be discarded due to higher optical density than the standard curve. According to the manufacturer's protocol, this could be due to faulty sample dilution or incomplete washing/drying of the wells. Repeating the test was recommended, but due to the constraints of using a single ELISA assay, this was not possible. Discarding these samples was a necessary step to ensure precision and validity of the analysis. Despite these exclusions, the remaining data provide a good basis for analysis of MOC1 and MOC2 cells production of PGE_2 after different radiation doses, as illustrated in Figure 38.

5.2 Discussion of Results

5.2.1 Comparison of immunosuppressor mechanism in MOC1 and MOC2 cells

The results indicate a difference in immunosuppressor mechanisms between MOC1 and MOC2 cells. MOC2 have higher base levels of both PD-L1 (Figure 22) and PGE_2 (Figure 37) while MOC1 showed a higher upregulation of these immunosuppressors in response to radiation. The same total doses given in two fractions, showed approximately the same PD-L1 signal, as delivered in one fraction (Figure 29), indicating that the tumor effect is the same even for fractionated dose delivery. The only exception was that MOC2 cells had a higher expression of PD-L1 after 3 fractions of 8 Gy (Figure 30). This was an interesting observation, given that the highest concentration of PGE_2 was discovered for the MOC1 cells after three fractions of 8 Gy (Figure 38). However, there was a large variation between the three experiments with PD-L1 measurements in MOC2 cells after 3 fractions of 8 Gy. A study performed by Botti et al found a positive correlation between COX-2 expression and PD-L1 expression in human melanoma cells ($BRAF^{V600E}$ A375 and $NRAS^{Q61R}$ SK-MEL-2). The COX-2 inhibitor celecoxib downregulated the expression of PD-L1 in vitro in a dose dependent matter (Botti et al., 2017). Our observations align with this finding, showing a correlation between the elevated PD-L1 and PGE_2 levels in both MOC1 and MOC2 cells.

The experiments indicate that MOC2 cells are highly immunosuppressive on their own, which remains unchanged when exposed to radiation. This aligns with the fact that MOC2 cells are a less immunogenic cell type, and as highlighted in Zelenay et al, the reduction of immunogenic signaling might be due to production of immunosuppressive factors. MOC1 cells on the other hand, are not as immunosuppressive, but become more immunosuppressive in response to ionizing radiation. This could indicate that cancers with characteristics like MOC1, which is a more immunogenic cell line, would benefit more from combination therapy of immune checkpoint inhibitors and radiation.

However, as discussed for the unspecific binding in section 5.1.2.3, also receptors for PD-L1 may increase as the cell goes through cell cycle. The high increase in cell size of MOC1 correlates with the higher measurements of PD-L1. It is possible that some of the PD-L1 signal increase could be explained by the increase in cell size, most likely due to G_2 arrest. This should be examined in future experiments.

To our knowledge, this is the first experiment that has investigated the effect of proton irradiation on PD-L1 expression in vitro. When MOC1 and MOC2 cells were positioned in front of the proton Bragg peak, the effect on PD-L1 signal was minimal, consistent with the effect observed after photon radiation at the equal doses. However, when exposed to proton radiation in the distal end of the Bragg peak, a significant increase in PD-L1 expression was observed, even at the lower doses (4Gy), for MOC1 and MOC2 cells (Figure

32). The PD-L1 signal increase after proton irradiation was comparable to the effect seen when MOC1 and MOC2 cells were irradiated with 10 and 12 Gy of photon radiation. When a high dose of 24 Gy with photon radiation was given in three fractions, an even higher upregulation was seen in both cell lines, where MOC2 had almost a three times higher signal than MOC1 cells, however with a high uncertainty. This calls for experiments investigating the effect of three proton dose fractions of for example 2 and 4 Gy in the distal end of the Bragg peak.

A recent study conducted within our group investigated responses in the two syngeneic tumor models MOC1 and MOC2 in C57BL/6J mice, following photon and proton irradiation, both with and without immune checkpoint inhibitors (PD-L1 inhibitors) (Rykkelid, 2023). The study discovered that the PD-L1 inhibitor alone resulted in a noteworthy 20±2% reduction in MOC1 tumor growth rates compared to controls. When irradiated with 5 Gy of photon radiaton, there was not induced any additional effects beyond the PD-L1 inhibitor treatment alone. However, for higher doses (10, 15, 20 Gy), the combination of PD-L1 inhibitor drugs and irradiation demonstrated reduced the tumor growth rates compared to irradiation or PD-L1 inhibitor treatment alone. Mice with MOC1 tumors mainly showed complete remission in groups treated with doses exceeding 10 Gy in combination with PD-L1 inhibitors. Considering the effect seen on the upregulation of PD-L1 on MOC1 cells after one fraction of photon radiation, this aligns with the effect seen on the tumors irradiated with the 5 Gy and the higher doses of 10, 15 and 20 Gy. For the lower doses (4 and 5 Gy) there were smaller upregulation of PD-L1 compared to the higher doses (10 and 12 Gy). Similar results were observed for proton irradiation.

The PD-L1 inhibitor alone did not show any reduction effect on the MOC2 tumors, as it did with MOC1. PD-L1 inhibitors in combination with photons did not show any significant effect on the MOC2 tumors either. The growth rate reduction from photons irradiation alone was the same as for the combination of photon irradiation and PD-L1 inhibitor. This trend aligns with the observations of the little effect that photons had on PD-L1 upregulation on MOC2 cells for these doses in this thesis. However, proton irradiation combined with PD-L1 had an effect on tumor growth of MOC2 tumors. In the proton experiments in this thesis, there was observed a higher effect of protons in the distal end of the Bragg peak while less in front of the Bragg peak, also for MOC2 cells. Even though the LET in the front of the Bragg peak of the low energy protons used in the experiment in this thesis, is closer to the clinical beam average LET, there will always be some protons of high LET comparable to that in our position in the distal end of the Bragg peak. The effect observed in vitro can therefore be part of the explanation for the observations in the mice experiments. However, all conclusions based on our in vitro proton experiment are uncertain since they are based on only one experiment.

The upregulation of PD-L1 signal on cancer cells after photon irradiation has also been observed in other studies. In Sato et al, the upregulation was seen in osteosarcoma (U2OS), lung cancer cells (H1299, A549) and prostate dancer (DU145) after irradiation of 10 and 20 Gy (Sato et al., 2017). In Wu et al. the humane bladder cell line HT1197 showed increased level of PD-L1 compare to control cells, for the doses 3, 6 and 9 Gy with the highest increase at 48 hours after irradiation (Wu et al., 2016). In Du et al. an upregulation of PD-L1 in a dose-dependent matter was detected in 3 human and 2 mouse liver cancer cells (Du et al., 2022).

As mentioned above, there were not any significant difference in the PD-L1 signal between the doses given either as one fraction or two fractions. There is obviously a fine balance between suppression and activation in the tumor microenvironment triggered by hypofractionation irradiation. Currently, it is not fully understood what dose and number of fractions of radiotherapy induces the immune activated tumor microenvironment, and what dose and number of fractions of radiotherapy causes the immunosuppressive tumor microenvironment (Wang, 2020). In our experiments, the 3x8Gy fractionation scheme showed a significant upregulation of PD-L1 in MOC1 and even higher in MOC2, and also an increase of PGE_2 in MOC1 cells. This indicates that this fractionation scheme in addition to be optimal for inducing an immunogenic response, could trigger a highly immunosuppressive tumor environment in MOC1 and MOC2 tumors. This is in line with findings of Wang et al. who state that there is a possibility that hypofractionation, in addition to inducing an immunogenic response, also triggers immunosuppressive mechanism that may counteracts for the antitumor effects (Wang, 2020).

Not many investigations of radiation effects on PGE_2 have been performed, but PGE_2 upregulation was found to be dose dependent in huma glioblastoma cells U251 (Brocard et al., 2015). The concentration of PGE_2 in the medium after 10 Gy was 15 [pg/ml]. Compared to the PGE_2 concentration from MOC1 and MOC2 the concentration was low, (and could be due to serum free medium), but an increase in the same order as was discovered in this thesis from the control was observed. The level was shown to increase immediately after irradiation and stay consistent over 48 hours (Brocard et al., 2015). In a different study performed by Hangai et al, the role of PGE_2 in murine G69 bladder cancer cells in vitro were investigated after chemotherapy. These cells had been shown to release DAMPs but did not undergo immunological cell death when treated with chemotherapy. In addition to DAMPs, it was discovered that G69 released PGE_2 in response to chemotherapy drugs. It was therefore hypothesized that PGE_2 counteracted the efficacy of DAMPs, by inhibiting immunologic cell death (ICD). The delicate balance between immunostimulatory and inhibitory DAMPs could be the cause. This influences the outcome of treatment-induced immunogenic cell death and makes PGE_2 blockade a potential strategy to increase the anti-tumor effect. This was validated in mouse models, where COX-2/PGE_2 blockade resulted in a

significantly enhanced anti-tumor response and suppressed tumor growth, especially when combined with chemotherapy drugs (Hangai et al., 2016).
The current treatment strategies focus mainly on confirming the immunostimulatory DAMP release to initiate ICD, neglecting the possibility of inhibitory DAMP being released from the cancer cells in response to treatment. Incorporating inhibitors of immunosuppressor into the treatment strategy could potentially increase the overall effectiveness of the treatment.

Our findings are in line with other studies and strongly indicate that there are mechanisms within cancer cells that upregulate the PD-L1 and PGE_2 production in response to the damage caused by ionizing radiation. In our experiments, a differential effect was seen in the two cell lines with different immunogenicity. However, to our knowledge no other studies compare cell lines with different immunogenic status. If this is a general phenomenon, it will be important to determine the immunogenicity of the tumor for each patient, to provide effective treatments. This is thus an important hypothesis that should be investigated in future research.

5.2.2 Comparison of immunogenic signaling in MOC1 and MOC2

Immunogenic signaling in the two cell lines after photon and proton irradiation was investigated in Senkaya's master thesis. In this thesis, the calreticulin expression on the cell membrane, which is considered an important DAMP induced by immunogenic cell death, was evaluated (2.5.1). MOC1 and MOC2 cells were irradiated with 4 and 8 Gy with photon and proton radiation in in front and in the distal end of the Bragg peak. Since the proton experiments performed in this thesis are not considered reliable and therefore difficult to conclude from, only the photon radiation experiments from Senkaya's thesis are considered.

Unirradiated MOC1 showed a relatively high signal of calreticulin that was not changed with dose or irradiation type. Unirradiated MOC2 had a lower signal but had a larger increase in level of calreticulin after irradiation, especially after 8 Gy. Normalized to the controls, the signal after 4 Gy of photon radiation were 1.17 ± 0.05 for MOC1 and 1.34 ± 0.07 for MOC2, and for 8 Gy of photon radiation the increased signal was 1.14 ± 0.01 for MOC1 and 1.81 ± 0.09 for MOC2 (Sankaya, 2022). This indicates that while MOC1 cells are more immunogenic without irradiation, MOC2 cells had a greater effect of irradiation in terms of surface exposed calreticulin.

This becomes very interesting when analyzed in combination with the data from the immunosuppressors, as it is almost the opposite. The indication of upregulation of PD-L1 on the cell membrane and concentration of PGE_2 show that MOC1 cells have immunosuppressor mechanism that is stimulated by radiation above 4 Gy, while no upregulation of the immunostimulatory calreticulin. MOC2 on the other hand, have a lower immunosuppressor upregulation of PD-L1 in response to radiation and no upregulation of PGE_2, and an upregulation of the immunostimulatory calreticulin. This indicates a balance

between the immunosuppressor and immune stimulatory signals of the cell lines, at least in response to doses up to 8 Gy. For the doses above 8 Gy, there is an even higher increase in both the immunosuppressor effects in MOC1 and only in PD-L1 immunosuppressor effects in MOC2. The calreticulin signal was not measured for doses above 8 Gy, but that would have been interesting to compare our results with.

5.2.3 Combination of PD-L1 and PGE_2 inhibitors

The synergistic potential of combining COX inhibitors, and thereby PGE_2 production inhibitors, with PD-L1 inhibitors holds significant promise for enhancing the effect of immunotherapy. Zelenay et al. performed a series of studies to evaluate the impact of COX inhibition in combination with immune modulation. In the study $Braf^{V600}$ cells were used and were analyzed for PGE_2 secretion. The cells are described as poorly immunogenic, and in line with our results, this cell line produced more PGE_2 compared to other cell lines tested in the same order as was observed with MOC1 and MOC2 cells.

Aspirin was used since it inhibits both COX-1 and COX-2 and was conveniently administered to mice through their drinking water. When administered alone, the aspirin exhibited limited tumor progression effect, possibly due to incomplete inhibition the COX activity. However, when aspirin was administered in combination with PD-L1 inhibitors, it promoted a rapid tumor regression and eradication of $Braf^{V600E}$ melanoma cells, compared to PD-L1 inhibitors alone, and showed a synergistic effect. The combination of aspirin and PD-L1 inhibitors treatment were also tested in mice bearing CT26 colorectal tumors and showed induced tumor growth control and complete shrinkage of tumors in 30% of the treated mice (Zelenay et al., 2015). The same effect was not observed in immunodeficient mice, indicating involvement of the immune system. This observation suggests that even a moderate level of COX inhibition could significantly amplify the impact of immunotherapies.

The combination of COX inhibitors in addition to immune checkpoint blockade shows potential in enhancing the anti-tumor effect. In light of our discoveries, the combination of PD-L1 and COX inhibitors (possibly PGE_2) and radiotherapy should be further investigated as a potential strategy to enhance the efficacy of cancer treatment.

5.3 Future perspectives

While the data obtained show promising insights, the statistical significance of the data is limited by the experiment repetitions and some observed variations. For higher reliability, additional repetitions of the PD-L1 experiments should be performed.

Additionally, the ELISA assay for quantification of PGE_2 secreted from irradiated MOC1 and MOC2 cells should be repeated. Especially since some samples had to be discarded due to too high optical density values. These repetitions would show if the result were reproducible and therefore increase the credibility of the results. It can also be evaluated if the samples should be analyzed in duplicates to increase the accuracy of the assay.

Since we have not found any other studies investigating the PD-L1 and PGE_2 following proton irradiation, this calls for more data and experiments. Only one PD-L1 experiment was performed on MOC1 and MOC2 cells following proton radiation. While these findings indicate a very interesting effect that radiation with a higher LET has on the cells, it is based on a limited dataset and cannot be considered as reliable data. Performing a minimum of two additional PD-L1 experiments with proton radiation to confirm the initial findings are necessary to improve the statistics for use of the data in a publication. As mentioned in section 5.2.1, the effect of three proton dose fractions should be investigated using lower doses than used for photons (8 Gy), for example 2 and 4 Gy. In addition, it would be interesting to quantify the PGE_2 secreted from the proton irradiated cells and compare it with the photon irradiated cells. A study using carbon ions with LET of 50 keV/µm, which is comparable to the LET of the protons in the distal end of the Bragg peak for the low energy protons used in this thesis, showed comparable levels of PGE_2 after 10 Gy of photons and 3 Gy of carbon ions (Allen et al., 2015).

To increase the reliability of these findings and draw more definitive conclusions, repetitions of the experiments should be performed and include a larger range of doses. This would provide more data for evaluating the impact proton irradiation has on PD-L1 signal and its potential to enhance the immunomodulatory effects of radiation therapy.

In addition, these issues should be further investigated:

- A549 cells were originally included in the thesis, but the data had to be discarded due to incorrect antibodies used in the analysis. Even though these are not as interesting to look at as MOC1 and MOC2 cells, as these can be tested in synergistic mouse models, we still have information about the immunostimulatory effects that A549 have in response to radiation. In addition to this there is much information on the A549 since this cell line is widely used. To perform the PD-L1 and PGE_2 analysis would give insight in the balance between the immunostimulatory and immunosuppressor effects and should be considered in the future
- To investigate the potential cause for the increased size of MOC1 cells, it is recommended to perform flow cytometry using PI staining of the DNA. This would provide more insight into the potential G_2 cell cycle arrest in response to radiation. This should be performed for MOC1 and MOC2 cell lines, to investigate if this has a correlation with the increased cell size and PD-L1 signal
- Considering that multiple studies observed a higher PD-L1 expression on the cells 48 hours after irradiation, a time dependent analysis experiment should be performed. Data from these timepoints could potentially show an even higher upregulation of PD-L1 compared to what was found at 24 hours in this thesis. This could provide important insight into the changes within the tumor microenvironment in response to irradiation over time
- As mentioned in several studies, the optimal dose and fractionation scheme for effect in tumor cells is not yet known. Therefore, different fractionation schemes could be tested to see if any other combinations of doses and number of fractions, give a higher upregulation of the immunosuppressors PD-L1 and PGE_2 in the tumor cells, also for proton irradiation
- The discovery of PD-L1 and PGE_2 upregulation in tumor cells following radiation, introduces an intriguing treatment strategy. By combining PD-L1 and PGE_2 inhibition with radiation therapy, there is potential to reduce the immunosuppressive mechanisms and hopefully increase treatment effectivity. This treatment combination should be evaluated in a synergic murine model

6 Conclusions

In this thesis, two different immunosuppressive pathways and their response to irradiation were studied. One was upregulation of PD-L1 (programmed death ligand 1) on tumor cells and the other was secretion of PGE_2 (prostaglandin E_2). The primary aim of this thesis was to investigate the complex immune related defense mechanisms exhibited by tumor cells in response to ionizing radiation. To investigate this aim, MOC1 and MOC2 cancer cells were irradiated with different doses, fractionation schemes and radiation types, followed by flow cytometry and ELISA to quantify the two immunosuppressing signals. The following conclusions can be drawn from the experiments performed in this thesis:

- Unirradiated MOC2 cells had a higher level of PD-L1 compared to MOC1 cells
- MOC1 showed an increase in PD-L1 in response to photon radiation above 4 Gy in a dose dependent manner
- MOC2 cells also showed an increase in PD-L1 level in a dose dependent matter, however a smaller increase than seen in MOC1 cells
- There was no significant difference between the PD-L1 level for the same total dose given in either one or two fractions in MOC1 and MOC2 cells
- The highest upregulation of PD-L1 was after 3x8 Gy for both MOC1 and MOC2 cells, where MOC2 had the highest level but also the highest uncertainty
- A single proton experiment indicates that both MOC1 and MOC2 cells have an upregulation of PD- L1 after proton irradiation in the distal end of the Bragg peak, even at the lower doses
- Unirradiated MOC2 (3314 [pg/ml]) secrete the most PGE_2 compared to MOC1 (1262 [pg/ml])
- MOC1 had an overall higher increase in secreted PGE_2 in response to doses of photon radiation above 8 Gy, with the highest difference at 3x8 Gy with 6475.44 [pg/ml] compared to MOC2 with 5566.5 [pg/ml]

These findings give an indication that cancer cells have intricate immunosuppressor mechanism that is upregulated in response to radiation and could be the cause for poor response to treatment and cancer recurrence. Therefore, treatment involving the combination of radiation and immune checkpoint inhibitors targeting the COX-2 and PD-L1 pathways, should be investigated to enhance tumor rejection in therapies. This potential is especially apparent for tumor types characterized with a higher immunogenicity. Hopefully, further research will continue and increase our knowledge about the complex tumor microenvironments and help us develop more efficient treatments for cancer.

7 References

Alberts, B. (2014). *Molecular Biology of the Cell* (Sixth ed.). Garland Publishing Inc.

Allen, C. P., Tinganelli, W., Sharma, N., Nie, J., Sicard, C., Natale, F., King, M., 3rd, Keysar, S. B., Jimeno, A., Furusawa, Y., Okayasu, R., Fujimori, A., Durante, M., & Nickoloff, J. A. (2015). DNA Damage Response Proteins and Oxygen Modulate Prostaglandin E2 Growth Factor Release in Response to Low and High LET Ionizing Radiation. *Front Oncol*, *5*, 260. https://doi.org/10.3389/fonc.2015.00260

Alsaab, H. O., Sau, S., Alzhrani, R., Tatiparti, K., Bhise, K., Kashaw, S. K., & Iyer, A. K. (2017). PD-1 and PD-L1 Checkpoint Signaling Inhibition for Cancer Immunotherapy: Mechanism, Combinations, and Clinical Outcome. *Front Pharmacol*, *8*, 561. https://doi.org/10.3389/fphar.2017.00561

Attix, F. H. (1986). *Introduction to Radiological Physics and Radiation Dosimetry*. Wiley-VCH.

Barsoumian, H. B., Sezen, D., Menon, H., Younes, A. I., Hu, Y., He, K., Puebla-Osorio, N., Wasley, M., Hsu, E., Patel, R. R., Yang, L., Cortez, M. A., & Welsh, J. W. (2022). High Plus Low Dose Radiation Strategy in Combination with TIGIT and PD1 Blockade to Promote Systemic Antitumor Responses. *Cancers*, *14*(1), 221. https://doi.org/10.3390/cancers14010221

Botti, G., Fratangelo, F., Cerrone, M., Liguori, G., Cantile, M., Anniciello, A. M., Scala, S., D'Alterio, C., Trimarco, C., Ianaro, A., Cirino, G., Caraco, C., Colombino, M., Palmieri, G., Pepe, S., Ascierto, P. A., Sabbatino, F., & Scognamiglio, G. (2017). COX-2 expression positively correlates with PD-L1 expression in human melanoma cells. *J Transl Med*, *15*(1), 46. https://doi.org/10.1186/s12967-017-1150-7

Brocard, E., Oizel, K., Lalier, L., Pecqueur, C., Paris, F., Vallette, F. M., & Oliver, L. (2015). Radiation-induced PGE₂sustains human glioma cell growth and survival through EGF signaling. *Oncotarget*, *6*(9), 6840-6849. https://doi.org/10.18632/oncotarget.3160

Caldwell, C., Johnson, C. E., Balaji, V. N., Balaji, G. A., Hammer, R. D., & Kannan, R. (2017). Identification and Validation of a PD-L1 Binding Peptide for Determination of PDL1 Expression in Tumors. *Scientific Reports*, *7*(1). https://doi.org/10.1038/s41598-017-10946-2

Dahl, O., Dale, J. E., & Brydøy, M. (2019). Rationale for combination of radiation therapy and immune checkpoint blockers to improve cancer treatment. *Acta Oncologica*, *58*(1), 9-20. https://doi.org/10.1080/0284186x.2018.1554259

Dahle, T. J., Rykkelid, A. M., Stokkevåg, C. H., Mairani, A., Görgen, A., Edin, N. J., Rørvik, E., Fjæra, L. F., Malinen, E., & Ytre-Hauge, K. S. (2017). Monte Carlo simulations of a low energy proton beamline for radiobiological experiments. *Acta Oncologica*, *56*(6), 779-786. https://doi.org/10.1080/0284186x.2017.1289239

Derrick, B., & White, P. (2016). Why Welch's test is Type I error robust. *The Quantitative Methods for Psychology*, *12*(1), 30-38. https://doi.org/10.20982/tqmp.12.1.p030

Dewan, M. Z., Galloway, A. E., Kawashima, N., Dewyngaert, J. K., Babb, J. S., Formenti, S. C., & Demaria, S. (2009). Fractionated but not single-dose radiotherapy induces an immune-mediated abscopal effect when combined with anti-CTLA-4 antibody. *Clin Cancer Res*, *15*(17), 5379-5388. https://doi.org/10.1158/1078-0432.CCR-09-0265

Donlon, N. E., Power, R., Hayes, C., Reynolds, J. V., & Lysaght, J. (2021). Radiotherapy, immunotherapy, and the tumour microenvironment: Turning an immunosuppressive

milieu into a therapeutic opportunity. *Cancer Lett*, *502*, 84-96. https://doi.org/10.1016/j.canlet.2020.12.045

Du, S. S., Chen, G. W., Yang, P., Chen, Y. X., Hu, Y., Zhao, Q. Q., Zhang, Y., Liu, R., Zheng, D. X., Zhou, J., Fan, J., & Zeng, Z. C. (2022). Radiation Therapy Promotes Hepatocellular Carcinoma Immune Cloaking via PD-L1 Upregulation Induced by cGAS-STING Activation. *Int J Radiat Oncol Biol Phys*, *112*(5), 1243-1255. https://doi.org/10.1016/j.ijrobp.2021.12.162

Faivre-Finn, C., Vicente, D., Kurata, T., Planchard, D., Paz-Ares, L., Vansteenkiste, J. F., Spigel, D. R., Garassino, M. C., Reck, M., Senan, S., Naidoo, J., Rimner, A., Wu, Y. L., Gray, J. E., Özgüroğlu, M., Lee, K. H., Cho, B. C., Kato, T., de Wit, M., . . . Antonia, S. J. (2021). Four-Year Survival With Durvalumab After Chemoradiotherapy in Stage III NSCLC-an Update From the PACIFIC Trial. *J Thorac Oncol*, *16*(5), 860-867. https://doi.org/10.1016/j.jtho.2020.12.015

Finetti, F., Travelli, C., Ercoli, J., Colombo, G., Buoso, E., & Trabalzini, L. (2020). Prostaglandin E2 and Cancer: Insight into Tumor Progression and Immunity. *Biology*, *9*(12), 434. https://doi.org/10.3390/biology9120434

Gan, S. D., & Patel, K. R. (2013). Enzyme Immunoassay and Enzyme-Linked Immunosorbent Assay. *Journal of Investigative Dermatology*, *133*(9), 1-3. https://doi.org/10.1038/jid.2013.287

Hall, E. J., & Giaccia, A. J. (2019). *Radiobiology for the Radiologist* (Eight Edition ed.). Wolters Kluwer.

Hangai, S., Ao, T., Kimura, Y., Matsuki, K., Kawamura, T., Negishi, H., Nishio, J., Kodama, T., Taniguchi, T., & Yanai, H. (2016). PGE2 induced in and released by dying cells functions as an inhibitory DAMP. *Proceedings of the National Academy of Sciences*, *113*(14), 3844-3849. https://doi.org/10.1073/pnas.1602023113

Hayashi, K., Nikolos, F., Lee, Y. C., Jain, A., Tsouko, E., Gao, H., Kasabyan, A., Leung, H. E., Osipov, A., Jung, S. Y., Kurtova, A. V., & Chan, K. S. (2020). Tipping the immunostimulatory and inhibitory DAMP balance to harness immunogenic cell death. *Nature Communications*, *11*(1). https://doi.org/10.1038/s41467-020-19970-9

Jin, K., Qian, C., Lin, J., & Liu, B. (2023). Cyclooxygenase-2-Prostaglandin E2 pathway: A key player in tumor-associated immune cells. *Front Oncol*, *13*, 1099811. https://doi.org/10.3389/fonc.2023.1099811

Judd, N. P., Winkler, A. E., Murillo-Sauca, O., Brotman, J. J., Law, J. H., Lewis, J. S., Jr., Dunn, G. P., Bui, J. D., Sunwoo, J. B., & Uppaluri, R. (2012). ERK1/2 regulation of CD44 modulates oral cancer aggressiveness. *Cancer Res*, *72*(1), 365-374. https://doi.org/10.1158/0008-5472.CAN-11-1831

Konstantinou, G. N. (2017). Enzyme-Linked Immunosorbent Assay (ELISA). In *Methods in Molecular Biology* (pp. 79-94). Springer New York. https://doi.org/10.1007/978-1-4939-6925-8_7

Kreftregisteret. (2022). *Cancer in Norway 2021 - Cancer incidence, mortality, survival and prevalence in Norway*. https://www.kreftregisteret.no/globalassets/cancer-in-norway/2021/cin_report.pdf

Lhuillier, C., Rudqvist, N.-P., Elemento, O., Formenti, S. C., & Demaria, S. (2019). Radiation therapy and anti-tumor immunity: exposing immunogenic mutations to the immune system. *Genome Medicine*, *11*(1). https://doi.org/10.1186/s13073-019-0653-7

Maecker, H. T., & Trotter, J. (2006). Flow cytometry controls, instrument setup, and the determination of positivity. *Cytometry Part A*, *69A*(9), 1037-1042. https://doi.org/10.1002/cyto.a.20333

Maity, B., Sheff, D., & Fisher, R. A. (2013). Immunostaining: detection of signaling protein location in tissues, cells and subcellular compartments. *Methods Cell Biol*, *113*, 81-105. https://doi.org/10.1016/B978-0-12-407239-8.00005-7

Mckelvey, K. J., Hudson, A. L., Back, M., Eade, T., & Diakos, C. I. (2018). Radiation, inflammation and the immune response in cancer. *Mammalian Genome*, *29*(11-12), 843-865. https://doi.org/10.1007/s00335-018-9777-0

Mckinnon, K. M. (2018). Flow Cytometry: An Overview. *Current Protocols in Immunology*, *120*(1). https://doi.org/10.1002/cpim.40

Pardoll, D. M. (2012). The blockade of immune checkpoints in cancer immunotherapy. *Nat Rev Cancer*, *12*(4), 252-264. https://doi.org/10.1038/nrc3239

Parham, P. (2021). *The Immune System* (Fifth ed.). W. W. Norton & Company.

Podgorsak, E. B. (2010). *Radiation Physics for medical Physicists* (Second Edition978- ed.). Springer. https://doi.org/https://doi.org/10.1007/978-3-642-00875-7

Punnanitinont, A., Kannisto, E. D., Matsuzaki, J., Odunsi, K., Yendamuri, S., Singh, A. K., & Patnaik, S. K. (2020). Sublethal Radiation Affects Antigen Processing and Presentation Genes to Enhance Immunogenicity of Cancer Cells. *International Journal of Molecular Sciences*, *21*(7), 2573. https://doi.org/10.3390/ijms21072573

Rodríguez-Ruiz, M. E., Vanpouille-Box, C., Melero, I., Formenti, S. C., & Demaria, S. (2018). Immunological Mechanisms Responsible for Radiation-Induced Abscopal Effect. *Trends in Immunology*, *39*(8), 644-655. https://doi.org/10.1016/j.it.2018.06.001

Rodriguez-Ruiz, M. E., Vitale, I., Harrington, K. J., Melero, I., & Galluzzi, L. (2020). Immunological impact of cell death signaling driven by radiation on the tumor microenvironment. *Nature Immunology*, *21*(2), 120-134. https://doi.org/10.1038/s41590-019-0561-4

Ruud, M. D. E.-O. (2020). *Immunogenic signaling in lung cancer in response to ionizing radiation* University of Oslo].

Rykkelid, A. M., Sinha, P. M., Asonganyi, F. C., Horsman, M. R., Sørensen, B. S., Søland, T. M., Schreurs, O. J. F., Malinen, E., Edin, N. F. J. (2023). Synergistic effects of combing proton- or X-irradiation with anti-PDL1 immunotherapy in two murine oral cancers. (in Review)

Sankaya, F. (2022). *Immunogenic Signaling in Human Lung and Mouse Oral Cancer Cells After X-ray and Proton Irradiation* University of Oslo].

Sato, H., Niimi, A., Yasuhara, T., Permata, T. B. M., Hagiwara, Y., Isono, M., Nuryadi, E., Sekine, R., Oike, T., Kakoti, S., Yoshimoto, Y., Held, K. D., Suzuki, Y., Kono, K., Miyagawa, K., Nakano, T., & Shibata, A. (2017). DNA double-strand break repair pathway regulates PD-L1 expression in cancer cells. *Nature Communications*, *8*(1). https://doi.org/10.1038/s41467-017-01883-9

Schaue, D., Ratikan, J. A., & Iwamoto, K. S. (2012). Cellular Autofluorescence following Ionizing Radiation. *PLoS ONE*, *7*(2), e32062. https://doi.org/10.1371/journal.pone.0032062

Segeritz, C.-P., & Vallier, L. (2017). Cell Culture: Growing Cells as Model Systems In Vitro. In *Basic Science Methods for Clinical Researchers*. Elsevier.

Thingstad, E. K. (2019). *Immunogenic calreticulin signaling in lung and glioblastoma cancer cells after x-ray and proton irradiation* University of Oslo].

Tian, X., Liu, K., Hou, Y., Cheng, J., & Zhang, J. (2018). The evolution of proton beam therapy: Current and future status. *Mol Clin Oncol*, *8*(1), 15-21. https://doi.org/10.3892/mco.2017.1499

Tzanoudaki, M., & Konsta, E. (2023). Basic Principles of Flow Cytometry. In *Intraoperative Flow Cytometry* (pp. 9-31). Springer International Publishing. https://doi.org/10.1007/978-3-031-33517-4_2

Vaes, R. D. W., Hendriks, L. E. L., Vooijs, M., & De Ruysscher, D. (2021). Biomarkers of Radiotherapy-Induced Immunogenic Cell Death. *Cells*, *10*(4), 930. https://doi.org/10.3390/cells10040930

Waldeland, E., Hole, E. O., Sagstuen, E., & Malinen, E. (2010). The energy dependence of lithium formate and alanine EPR dosimeters for medium energy x rays. *Med Phys*, *37*(7), 3569-3575. https://doi.org/10.1118/1.3432567

Wang, Y. (2020). Advances in Hypofractionated Irradiation-Induced Immunosuppression of Tumor Microenvironment. *Front Immunol*, *11*, 612072. https://doi.org/10.3389/fimmu.2020.612072

Wu, C.-T., Chen, W.-C., Chang, Y.-H., Lin, W.-Y., & Chen, M.-F. (2016). The role of PD-L1 in the radiation response and clinical outcome for bladder cancer. *Scientific Reports*, *6*(1), 19740. https://doi.org/10.1038/srep19740

Zelenay, S., van der Veen, A. G., Bottcher, J. P., Snelgrove, K. J., Rogers, N., Acton, S. E., Chakravarty, P., Girotti, M. R., Marais, R., Quezada, S. A., Sahai, E., & Reis e Sousa, C. (2015). Cyclooxygenase-Dependent Tumor Growth through Evasion of Immunity. *Cell*, *162*(6), 1257-1270. https://doi.org/10.1016/j.cell.2015.08.015

8 Appendix

8.1 PD-L1 Assay

PD-L1 assay for flow cytometry (no dye, control as sample)

The assay was optimized for cell line MOC1+2. Different cell lines might need higher or lower concentrations of antibodies.

Compound	*Amount/sample + control (4 dishes)*			*Storage*
PBS	150 ml	-	-	Fridge cell lab
PBS w/BSA(1%)	2 mL	-	-	Freezer chemical storage
TrypLE	8	-	-	Freezer chemical storage
Medium	16	-	-	Fridge cell lab
Primary antibody	2,25 µl in 450 µl PBS w/BSA (5 µL/mL)	-	-	Freezer instrument lab
Isotype				

Primary antibody: **Mouse Anti-PD-L1/B7-H1 Alexa Fluor 647 conjugated antibody (R&D FAB90781R)**

Isotype control: **Rabbit IgG Alexa Fluor 647 conjugated antibody (R&D ICI051R)**

PBS and medium at room temperature

Ice from Ice machine

1. **Split and harvest samples**
   Prepare Eppendorf tubes (1.5 ml), write dose, number and PD-L1/isotype
   Add 4 ml cold medium to one normal tube (12 ml) for each sample.

   Remove medium from samples
   Flush with 5 ml warm PBS
   Add 2ml warm TrypLE, incubate for about 6-10 min
   Suspend to single cells with 2 ml pipette
   Add suspended cells into the tubes with medium
   Centrifuge 200 xg, 4 min, put on ice and aspirate.
   Add two ml cold PBS to each sample and resuspend, then transfer 1 ml cell solution into Eppendorf tubes, 1 for primary antibody, 1 for isotype control.
   Centrifuge 200 xg, 4 min, put on ice and aspirate before adding primary/isotype antibody.

2. **Primary Antibody and isotype control**
   Mix primary antibody: number of samples x (0, 5 µl primary ab/100 µl PBS w/BSA).
   Mix isotype antibody: number of samples x (0, 5 µl isotype/100 µl PBS w/BSA).
   (Add 0.25 µl P/I and 50 µl PBS w/BSA to have extra)

   Add 100 µl of primary or isotype solution to each sample and resuspend
   Incubate in dark for 30 min on ice.

3. **Wash**
   Add 1 ml PBS to each sample and mix ligthly, centrifuge 200 xg, 4 min.
   Aspirate supernatant.
   Repeat once more, where the cells are resuspended in the PBS.
   Resuspend the pellets in 250*[1] µl PBS and store at 4°C until flow cytometry analysis.

4. **Live/dead staining, filtering, and flow analysis**
   Prior to flow cytometry analysis, add 0.5*[2] µl propidium iodine (PI) 1.0 mg/ml to the samples for live/dead staining, right before filtering into tubes and running flow.

Abbreviation	Name	Substance	Channel
PA	Primary Antibody	**Anti-PD-L1/B7-H1 Alexa Fluor 647**	FL4
IA	Isotype Antibody	**IgG Alexa Fluor 647**	FL4
PI	Live/Death	Propidium iodide solution	FL2, FL3

*[1] When using Attune Nxt flow cytometer, resuspend the cells in 750 µl

*[2] When using Attune Nxt flow cytometer, add 1.5 µl of PI

8.1.1 Raw data from PD-L1 assays

8.1.1.1 One fraction of photon irradiation on MOC1 cells

Table 7: Raw data from PD-L1 flow cytometry assay on MOC1 cells irradiated with one fraction of 4 Gy and 8 Gy photon irradiation.

Date	Dose [Gy]	Biological replicate	Primary antibody (median)	Isotype control (median)
30.08.2022	Control	1	777	614
		2	791	640
	4	1	820	659
		2	878	702
	8	1	1119	828
		2	977	802
04.10.2022	Control	1	923	617
		2	979	642
	4	1	996	722
		2	977	736
	8	1	1155	816
		2	1180,5	834
04.11.2022	Control	1	825	618
		2	760	604
	4	1	783	632
		2	1130	987
	8	1	969	808
		2	1197	977
19.03.2023	Control	1	609	536
		2	615	528
	4	1	637	533
		2	654	539
	8	1	800	656
		2	764	676
28.05.2023	Control	1	4945	4364
		2	4944	4466
	4	1	6325	5412
		2	6361	5398
	8	1	8585	7261
		2	8403	6839

Table 8: Raw data from PD-L1 flow cytometry assay on MOC1 cells irradiated with one fraction of 5 Gy and 10 Gy of photon irradiation. These experiments were performed by Nina F. J. Edin

Date	Dose [Gy]	Biological replicate	Primary antibody (median)	Isotype (median)
02.02.2022	Control	1	607	433
		2	593	429
	5	1	741	489
		2	704	477
	10	1	879	586
		2	901	561
24.02.2022	Control	1	589	469
		2	570	450
	5	1	713	489
		2	659	503
	10	1	766	533
		2	744	507
23.03.2022	Control	1	558	402
		2	559	376
	5	1	651	436
		2	702	455
	10	1	813	489
		2	707	436

Table 9: Raw data from PD-L1 flow cytometry assay on MOC1 cells irradiated with one fraction of 12 Gy of photon irradiation.

Date	Dose [Gy]	Biological replicate	Primary antibody (median)	Isotype (median)
03.04.2023 (morning)	Control	1	822	749
		2	844	769
	12	1	1730	1262
		2	1711	1305
03.04.2023 (afternoon)	Control	1	830	687
		2	782	687
	12	1	1638	1284
		2	1511	1255
06.05.2023	Control	1	136	105
		2	132	105
	12	1	SAMPLE LOST	177
		2	240	188
15.05.2023	Control	1	5828	4905
		2	5362	4542
	12	1	11118	7333
		2	9742	7510
13.06.2023	Control	1	3820	3303
		2	3788	3300
	12	1	6458	5521
		2	5820	5048

8.1.1.2 One fraction of photon irradiation on MOC2 cells

Table 10: Raw data from PD-L1 flow cytometry assay on MOC2 cells irradiated with one fraction of 4 Gy and 8 Gy photon irradiation.

Date	Dose [Gy]	Biological replicate	Primary antibody (median)	Isotype (median)
31.08.2023	Control	1	1128	892
		2	1139	853
	4	1	995	710
		2	990	733
	8	1	1129	772,5
		2	1041	841
04.10.2022	Control	1	991	754
		2	956	788,5
	4	1	1180	895
		2	1375	1085
	8	1	1243	934,5
		2	1243	1002
04.11.2022	Control	1	1586	1360
		2	1268	1165,5
	4	1	1222	1047
		2	2767	2577
	8	1	1335	1181
		2	1136	995,5
19.03.2023	Control	1	912	646
		2	872	648
	4	1	959,5	698,5
		2	918	660
	8	1	1036	750
		2	1024	740
28.05.2023	Control	1	13772	11657
		2	13784	11381
	4	1	15821	13172
		2	15689	12515
	8	1	17892	14339
		2	17585	14266

Table 11: Raw data from PD-L1 flow cytometry assay on MOC2 cells irradiated with one fraction of 5 Gy and 10 Gy of photon irradiation. These experiments were performed by Nina F. J. Edin

Date	Dose [Gy]	Biological replicate	Primary antibody (median)	Isotype (median)
02.02.2022	Control	1	736	481
		2	693	460
	5	1	778	429
		2	711	476
	10	1	722	522
		2	708	497
24.02.2022	Control	1	742	643
		2	718	606
	5	1	692	612
		2	786	583
	10	1	887	721
		2	875	670
23.03.2022	Control	1	755	541
		2	762	514
	5	1	830	562
		2	817	561
	10	1	972	598
		2	940	634

Table 12: Raw data from PD-L1 flow cytometry assay on MOC2 cells irradiated with one fraction of 12 Gy of photon irradiation. The value indicated in red, was excluded from the analysis, since the majority of the cells in the sample had broken membranes.

Date	Dose [Gy]	Biological replicate	Primary antibody (median)	Isotype (median)
03.04.2023 (morning)	Control	1	1522	1237
		2	1492	1217
	12	1	2098	1558
		2	1826	1470
03.04.2023 (afternoon)	Control	1	1100,5	1183
		2	1371	1167
	12	1	1797,5	1386
		2	1817	1361,5
06.05.2023	Control	1	228	158
		2	371	300
	12	1	323	233
		2	285	187
15.05.2023	Control	1	11569	8867
		2	11292	8514
	12	1	13487	9793
		2	13622	9768
13.06.2023	Control	1	9041	7312
		2	8976	7140
	12	1	14515	11115
		2	14620	11404

8.1.1.3 One fraction of photon irradiation on A549 cells

Table 13: Raw data from PD-L1 flow cytometry assay on A549 cells irradiated with one fraction of 5 Gy and 10 Gy of photon irradiation.

Date	Dose [Gy]	Biological replicate	Primary antibody (median)	Isotype (median)
17.11.2022	Control	1	679	659
		2	687,5	618
	4	1	859	794
		2	729	696
	8	1	830	764
		2	794	729
24.11.2022	Control	1	752	708
		2	726	699
	4	1	845	833
		2	878	851
	8	1	962	970
		2	953	920
02.12.2022	Control	1	727	684
		2	716	659
	4	1	963	898
		2	861	827
	8	1	1002	935
		2	1035	953

8.1.1.4 Two fractions of photon irradiation on MOC1 cells

Table 14: Raw data from PD-L1 flow cytometry assay on MOC1 cells irradiated with two fractions of 2+2 Gy and 4+4 Gy photon irradiation.

Date	Dose [Gy]	Biological replicate	Primary antibody (median)	Isotype (median)
12.02.2023	Control	1	727	628
		2	712	601
	2+2	1	755	615
		2	741	598
	4+4	1	813	654
		2	808	686
20.02.2023	Control	1	865	656
		2	841	620
	2+2	1	872	679
		2	831	653
	4+4	1	960	726
		2	954	754
15.03.2023	Control	1	957	769
		2	850	665
	2+2	1	886	726
		2	895	708
	4+4	1	1078	839
		2	1014	844

Table 15: Raw data from PD-L1 flow cytometry assay on MOC1 cells irradiated with two fractions of 6+6 Gy of photon irradiation.

Date	Dose [Gy]	Biological replicate	Primary antibody (median)	Isotype (median)
03.04.2023 (morning)	Control	1	822	749
		2	844	769
	6+6	1	1639	1236
		2	1551,5	1276
03.04.2023 (afternoon)	Control	1	830	687
		2	782	687
	6+6	1	1517	1178
		2	1523	1234
06.05.2023	Control	1	136	105
		2	132	105
	6+6	1	255	193
		2	232	181

8.1.1.5 Two fractions of photon irradiation on MOC2 cells

Table 16: Raw data from PD-L1 flow cytometry assay on MOC2 cells irradiated with two fractions of 2+2 Gy and 4+4 Gy photon irradiation.

Date	Dose [Gy]	Biological replicate	Primary antibody (median)	Isotype (median)
12.02.2023	Control	1	1066	870
		2	1032	847
	2+2	1	1103	891
		2	1184	953
	4+4	1	1253	1015
		2	1284	1080
20.02.2023	Control	1	1155	926
		2	1144	954
	2+2	1	1208	962
		2	1217	954
	4+4	1	1391	1102
		2	1329	999
15.03.2023	Control	1	1394	1186
		2	1242	909
	2+2	1	1318	971
		2	1306	976
	4+4	1	1750	1240
		2	1441	1041

Table 17: Raw data from PD-L1 flow cytometry assay on MOC2 cells irradiated with two fractions of 6+6 Gy of photon irradiation. The value indicated in reed, is excluded from the analysis, since was the signal detected from a sample where most of the cells had a broken membrane.

Date	Dose [Gy]	Biological replicate	Primary antibody (median)	Isotype (median)
03.04.2023 (morning)	Control	1	1522	1237
		2	1492	1217
	6+6	1	1918	1439
		2	1940	1441,5
03.04.2023 (afternoon)	Control	1	1102	1162
		2	1369	1165
	6+6	1	1679	1376
		2	1807	1324
06.05.2023	Control	1	228	158
		2	371	300
	6+6	1	283	181
		2	416	333

8.1.1.6 Three fractions of photon irradiation on MOC1 cells

Table 18: Raw data from PD-L1 flow cytometry assay on MOC1 cells irradiated with three fractions of 8 Gy of photon irradiation, making a total of 24 Gy

Date	Dose [Gy]	Biological replicate	Primary antibody (median)	Isotype (median)
13.06.2023	Control	1	3820	3303
		2	3788	3300
	8+8+8	1	14284	12072
		2	14315	11657
20.06.2023	Control	1	4810	4249
		2	3939	3435
	8+8+8	1	11747	9603
		2	11654	9683
20.06.2023	Control	1	3860	3329
		2	3873	3326
	8+8+8	1	13327	11257
		2	64405	61968

8.1.1.7 Three fractions of photon irradiation on MOC2 cells

Table 19: Raw data from PD-L1 flow cytometry assay on MOC2 cells irradiated with three fractions of 8 Gy of photon irradiation, making a total of 24 Gy

Date	Dose [Gy]	Biological replicate	Primary antibody (median)	Isotype (median)
13.06.2023	Control	1	9041	7313
		2	8976	7140
	8+8+8	1	21837	15898
		2	22111	15785
20.06.2023	Control	1	9348	6529
		2	9245	6520
	8+8+8	1	27508	12675
		2	25633	12038
20.06.2023	Control	1	9541	6408
		2	9379	6311
	8+8+8	1	26777	12134
		2	46478	29823

8.1.1.8 One fraction of proton irradiation on MOC1 and MOC2 cells

Table 20: Raw data from PD-L1 flow cytometry assay on MOC1 cells irradiated with one fraction of 4 and 8 Gy of proton irradiation. Cells were irradiated in front of the Bragg peak (P1) and in the distal end of the Bragg peak (P5)

Date	Position	Dose [Gy]	Biological replicate	Primary antibody (median)	Isotype (median)
08.09.2023	P1	Control	1	741	564
			2	710	555
			3	662	550
		4	1	679	523
			2	712	569
			3	670	595
		8	1	775	614
			2	834	609
			3	842	677
	P5	Control	1	663	558
			2	643	556
			3	634	545
		4	1	1083	791
			2	1036	772
			3	1138	862
		8	1	1102,5	769
			2	1080	780
			3	1082,5	799

Table 21: Raw data from PD-L1 flow cytometry assay on MOC2 cells irradiated with one fraction of 4 and 8 Gy of proton irradiation. Cells were irradiated in front of the Bragg peak (P1) and in the distal end of the Bragg peak (P5)

Date	Position	Dose [Gy]	Biological replicate	Primary antibody (median)	Isotype (median)
14.09.2023	P1	Control	1	1209	965
			2	1160	958
			3	1110	939
		4	1	1170	963
			2	1180	901
			3	1175	934,5
		8	1	1221	920
			2	1237	895
			3	1184	917
	P5	Control	1	1209	965
			2	1160	958
			3	1110	939
		4	1	1355	931
			2	1480	1076
			3	1391	981
		8	1	1609	1105
			2	1652	1122
			3	1641	1141

8.1.2 Forward scatter signal for MOC1 and MOC2

Table 22: The Forward scatter signal (FSC) for MOC1 and MOC2, irradiated with 4, 8, 12, 6+6 and 8+8+8 Gy, where the two last are given in two and three fractions.

Date	Dose [Gy]	Biological replicate	MOC1 (FSC median)	MOC2 (FSC median)
28.05.2023	Control	1	338,398	570,558
		2	335,214	558,618
		3	352,885	529,963
		4	361,884	537,509
	4	1	386,249	626,461
		2	403,497	639,661
		3	419,734	641,061
		4	430,959	619,855
	8	1	570,147	714,979
		2	541,767	721,065
		3	562,651	710,823
		4	560,771	713,743
08.05.2023	Control	1	330,805	563,759
		2	368,576	570,702
		3	396,89	560,375
		4	367,461	573,425
	12	1	SAMPLE LOST	615,786
		2	663,109	621,096
		3	653,926	612,846
		4	651,442	623,799
	6+6	1	575,048	605,872
		2	611,984	616,43
		3	568,761	612,988
		4	577,268	614,896
15.05.2023	Control	1	399,391	626,344
		2	398,048	602,017
		3	392,091	610,13
		4	390,415	597,633
	12	1	637,254	797,221
		2	663,763	793,159
		3	668,385	796,747
		4	674,076	784,178

13.06.2023	Control	1	372,985	586,414
		2	362,39	619,024
		3	405,683	600,552
		4	393,127	589,27
	12	1	426,265	731,46
		2	437,755	726,936
		3	418,79	733,915
		4	417,659	722,711
	8+8+8	1	564,375	778,712
		2	597,017	768,23
		3	587,562	765,868
		4	605,387	767,141
20.06.2023 (m)	Control	1	367,021	549,342
		2	354,187	545,684
		3	347,762	560,009
		4	352,397	560,402
	8+8+8	1	549,324	624,629
		2	548,883	619,183
		3	572,97	627,951
		4	573,919	615,501
20.06.2023 (a)	Control	1	318,074	560,525
		2	321,142	552,742
		3	336,334	554,629
		4	330,073	542,697
	8+8+8	1	575,979	608,659
		2	580,237	603,629
		3	575,481	626,665
		4	581,603	618,837

8.2 ELISA assay

SAMPLE PREPARATION

All samples require a 3-fold dilution. A suggested 3-fold dilution is 150 µL of sample + 300 µL of Calibrator Diluent RD5-56.

SAMPLE COLLECTION & STORAGE

The sample collection and storage conditions listed below are intended as general guidelines. Sample stability has not been evaluated.

Samples containing mouse or rat IgG may interfere with this assay.
Cell Culture Supernates - Remove particulates by centrifugation. Assay immediately or aliquot and store samples at ≤ -20 °C. Avoid repeated freeze-thaw cycles.

REAGENT PREPARATION

Bring all reagents to room temperature before use.

Wash Buffer - If crystals have formed in the concentrate, warm to room temperature and mix gently until the crystals have completely dissolved. Add 20 mL of Wash Buffer Concentrate to 480 mL of deionized or distilled water to prepare 500 mL of Wash Buffer.

Substrate Solution - Color Reagents A and B should be mixed together in equal volumes within 15 minutes of use. Protect from light. 200 µL of the resultant mixture is required per well.

PGE_2 Standard - Refer to the vial label for reconstitution volume. Reconstitute the PGE_2 Standard with deionized or distilled water. This reconstitution produces a stock solution of 25,000 pg/mL. Mix the standard to ensure complete reconstitution and allow the standard to sit for a minimum of 15 minutes with gentle agitation prior to making dilutions.

Pipette 900 µL of Calibrator Diluent RD5-56 into the 2500 pg/mL tube. Pipette 500 µL into the remaining tubes. Use the 25,000 pg/mL standard stock to produce a dilution series (below). Mix each tube thoroughly and change pipette tips between each transfer. The 2500 pg/mL standard serves as the high standard. Calibrator Diluent RD5-56 serves as the zero standard (B0) (0 pg/mL).

ASSAY PROCEDURE

Bring all reagents and samples to room temperature (18-23 °C) before use. It is recommended that all standards, controls, and samples be assayed in duplicate.

1. Prepare all reagents, working standards, and samples as directed in the previous sections.
2. Remove excess microplate strips from the plate frame, return them to the foil pouch containing the desiccant pack, and reseal.
3. Add 200 µL of Calibrator Diluent RD5-56 to the non-specific binding (NSB) wells.
4. Add 150 µL of Calibrator Diluent RD5-56 to the zero standard (B_0) wells.
5. Add 150 µL of standard, control, or sample* to the remaining wells.
6. Add 50 µL of the Primary Antibody Solution to each well **(excluding the NSB wells)**. All wells except the NSB wells will now be blue in color.
7. Securely cover with a plate sealer, and incubate for 1 hour at room temperature on a horizontal orbital microplate shaker (0.12" orbit) set at 500 ± 50 rpm. A plate layout is provided to record standards and samples assayed.
8. **Do not wash the plate.** Add 50 µL of PGE_2 Conjugate to each well. All wells except the NSB wells will now be violet in color.
9. Cover with a new plate sealer, and incubate for 2 hours at room temperature on the shaker.
10. Aspirate each well and wash, repeating the process three times for a total of four washes. Wash by filling each well with Wash Buffer (400 µL) using a squirt bottle, manifold dispenser, or autowasher. Complete removal of liquid at each step is essential to good performance. After the last wash, remove any remaining Wash Buffer by aspirating or decanting. Invert the plate and blot it against clean paper towels.
11. Add 200 µL of Substrate Solution to each well. Incubate for 30 minutes at room temperature **on the benchtop. Protect from light.**
12. Add 100 µL of Stop Solution to each well. The color in the wells should change from blue to yellow. If the color in the wells is green or the color change does not appear uniform, gently tap the plate to ensure thorough mixing.
13. Determine the optical density of each well within 30 minutes, using a microplate reader
    set to 450 nm. If wavelength correction is available, set to 540 or 570 nm. If wavelength correction is not available, subtract readings at 540 or 570 nm from the readings at 450 nm. This subtraction will correct for optical imperfections in the plate. Readings made directly at 450 nm without correction may be higher and less accurate.

*Samples require dilution. See Sample Preparation section.

CALCULATION OF RESULTS

Average the duplicate readings for each standard, control, and sample then subtract the average NSB optical density (O.D.).

Create a standard curve by reducing the data using computer software capable of generating a four parameter logistic (4-PL) curve-fit. As an alternative, construct a standard curve by plotting the mean absorbance for each standard on a linear y-axis against the concentration on a logarithmic x-axis and draw the best fit curve through the points on the graph. Do not include the B_0 in the standard curve.

If desired, % B/B_0 can be calculated by dividing the corrected OD for each standard or sample by the corrected B_0 O.D. and multiplying by 100.

Calculate the concentration of PGE_2 corresponding to the mean absorbance from the standard curve.

Since samples have been diluted, the concentration read from the standard curve must be multiplied by the dilution factor.

8.2.1 Raw data

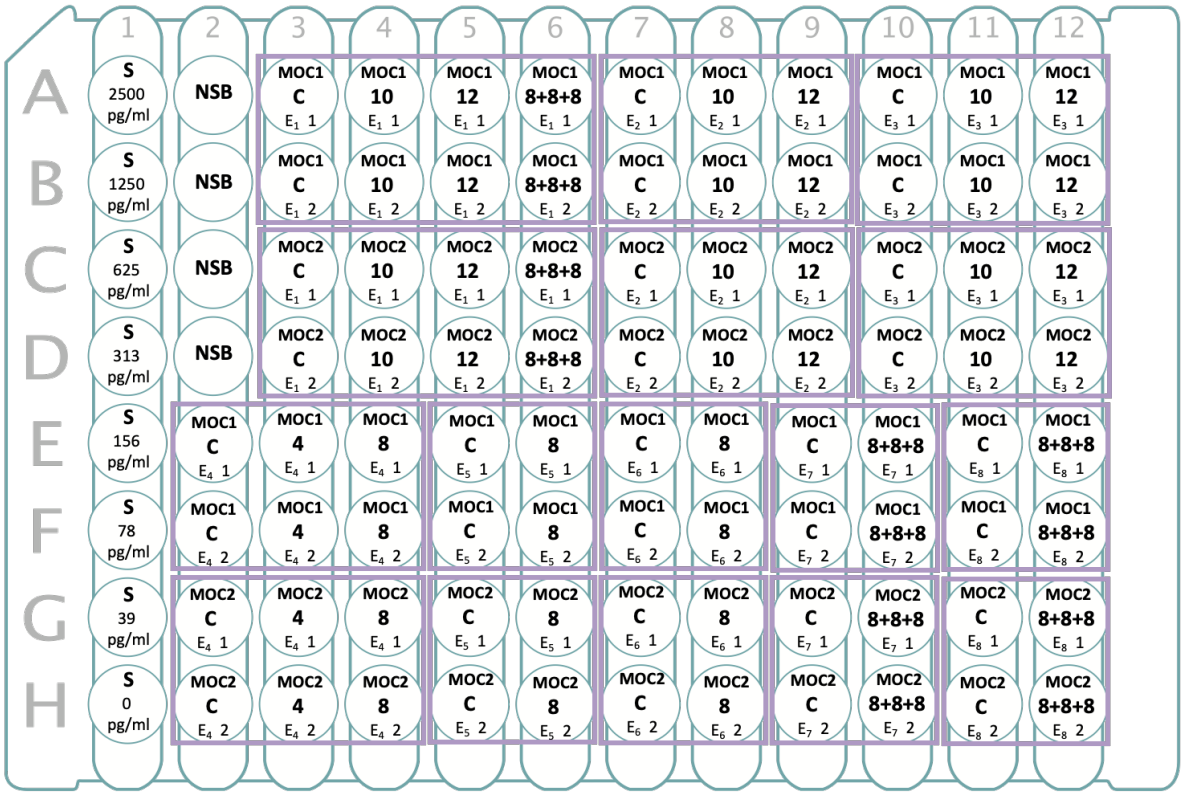

Figure 39: An overview over the placements of the samples in the plate during the ELISA analysis. In each well, the cell line the sample belongs to is indicated on the top, the treatment the cells received is indicated in the middle, if it is either a control or which dose it was irradiated with. 8+8+8 indicates the samples that were irradiated with three doses of 8 Gy. On the bottom, the left 'E_1' indicates with experiment repetition the sample is a part of, and the right number indicates the biological repetition number. The experiment samples that belong together is marked. The left column has the standard curve, which is a serial dilution of PGE_2 standard concentrate. The NSB wells are non -specific binding wells and are wells where no primary antibody solution is added and is used to correct the other samples.

Table 23: The raw data from the PGE_2 ELISA assay on medium sampled from MOC1 and MOC2 cells irradiated with 4, 8, 10, 12 and three fractions of 8 Gy. An overview over the samples added in each well is given in Figure 39.

	1	2	3	4	5	6	7	8	9	10	11	12
A	0,089	0,012	0,308	0,303	3,072	0,090	0,338	0,307	0,311	0,383	0,249	0,176
B	0,170	0,011	0,320	0,221	3,124	0,182	0,318	0,288	0,294	0,358	0,218	0,237
C	0,244	0,010	0,196	0,202	0,491	0,122	0,180	0,153	0,191	0,165	2,253	0,149
D	0,336	0,008	0,173	0,198	0,188	0,116	0,161	0,163	0,171	1,899	2,866	0,139
E	0,368	0,404	0,333	0,375	0,298	0,329	0,311	0,297	0,271	0,090	0,258	0,094
F	0,411	0,389	0,378	0,355	0,257	0,265	0,301	0,276	0,265	0,103	0,231	0,124
G	0,411	0,324	0,310	3,476	0,253	0,407	0,275	0,192	0,133	0,126	0,131	0,144
H	0,400	0,338	0,317	3,446	0,243	0,265	0,243	0,269	0,154	0,140	0,133	0,130

8.2.2 Alternative analysis of the ELISA data

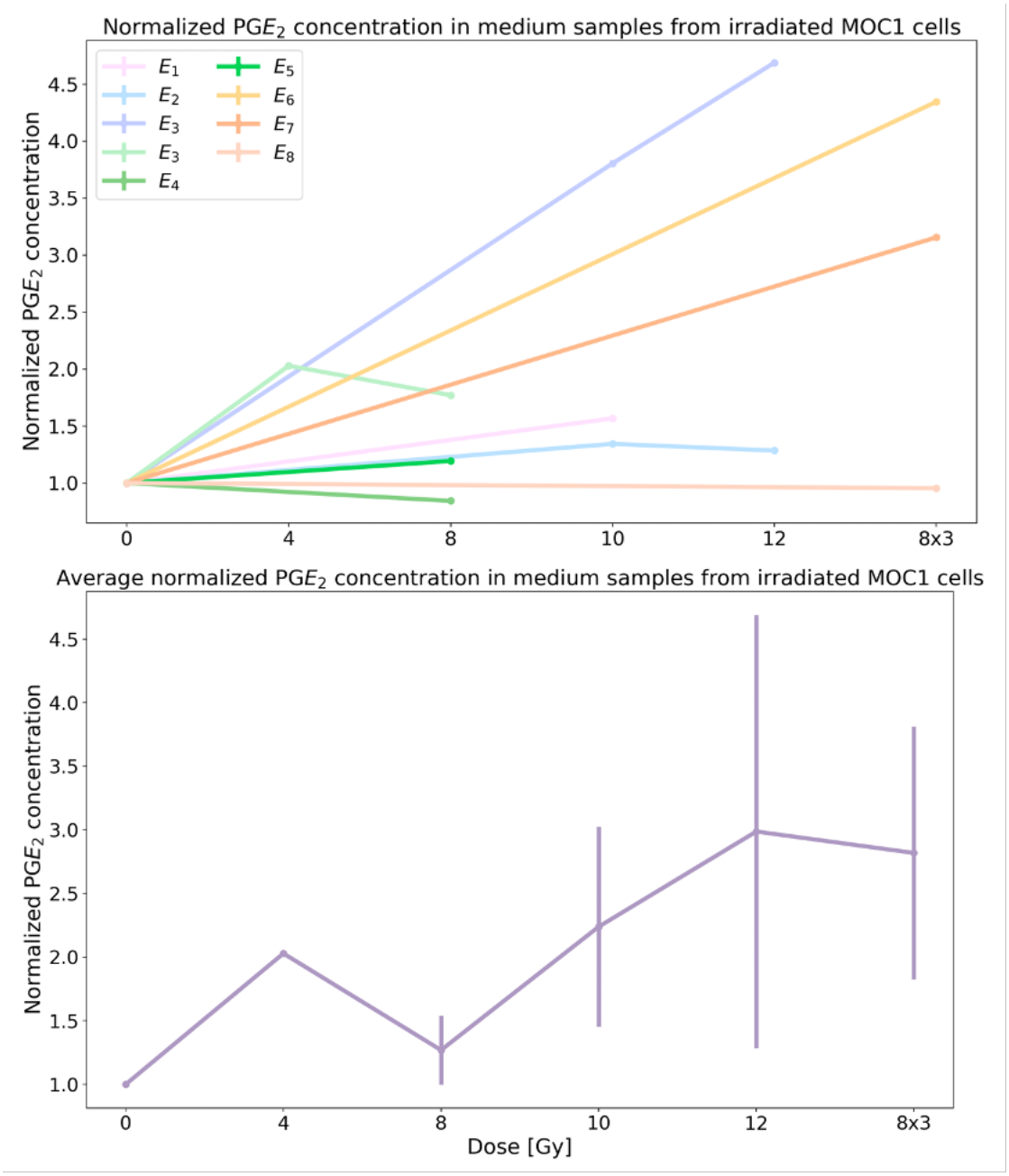

Figure 40: ***The normalized PGE2 concentration in medium from MOC1 cells after irradiation*** *with 4 Gy (n=1), 8 Gy (n=3), 10 Gy (n=3), 12 Gy (n=2) and three fractions of 8 Gy (n=3), where 'n' is number of repetitions. The samples were harvested 24 hours after the total dose was delivered. The data was calculated individually, and then averaged. This caused a high uncertainties and very variable data. This can be explained by variation in the data caused by the ELISA analysis, and not by the concentrations in the samples. Another analysis method was used based on this. The error bars represent the standard error of the mean. Only one experiment was analyzed for 4 Gy, therefore there are no error bars.*

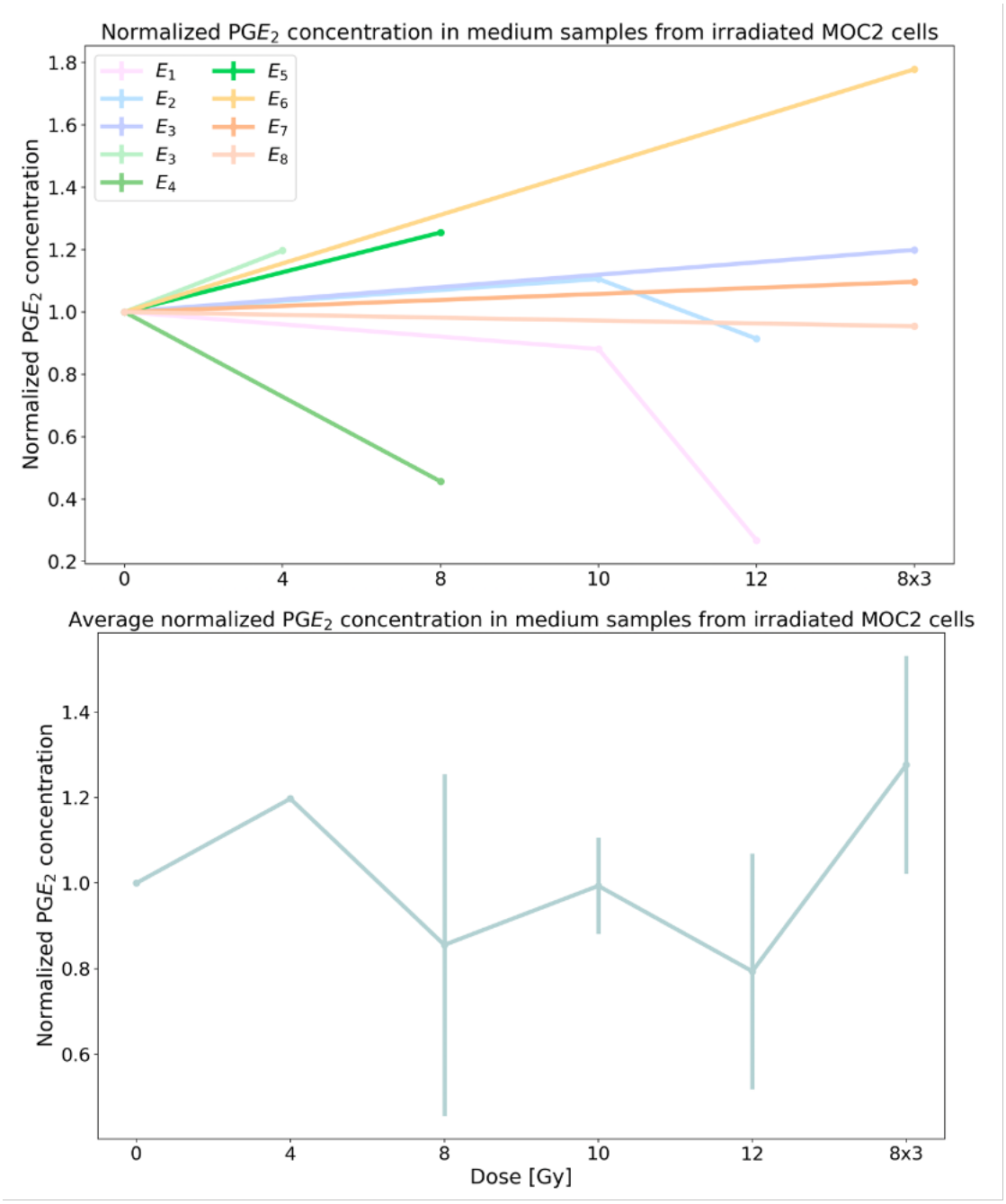

Figure 41: ***The normalized PGE$_2$ concentration in medium from MOC2 cells after irradiation*** *with 4 Gy (n=1), 8 Gy (n=2), 10 Gy (n=2), 12 Gy (n=3) and three fractions of 8 Gy (n=3), where 'n' is number of repetitions. The samples were harvested 24 hours after the total dose was delivered. The data was calculated individually, and then averaged. This caused a high uncertainties and very variable data. This can be explained by variation in the data caused by the ELISA analysis, and not by the concentrations in the samples. Another analysis method was used based on this. The error bars represent the standard error of the mean. Only one experiment was analyzed for 4 Gy, therefore there are no error bars.*

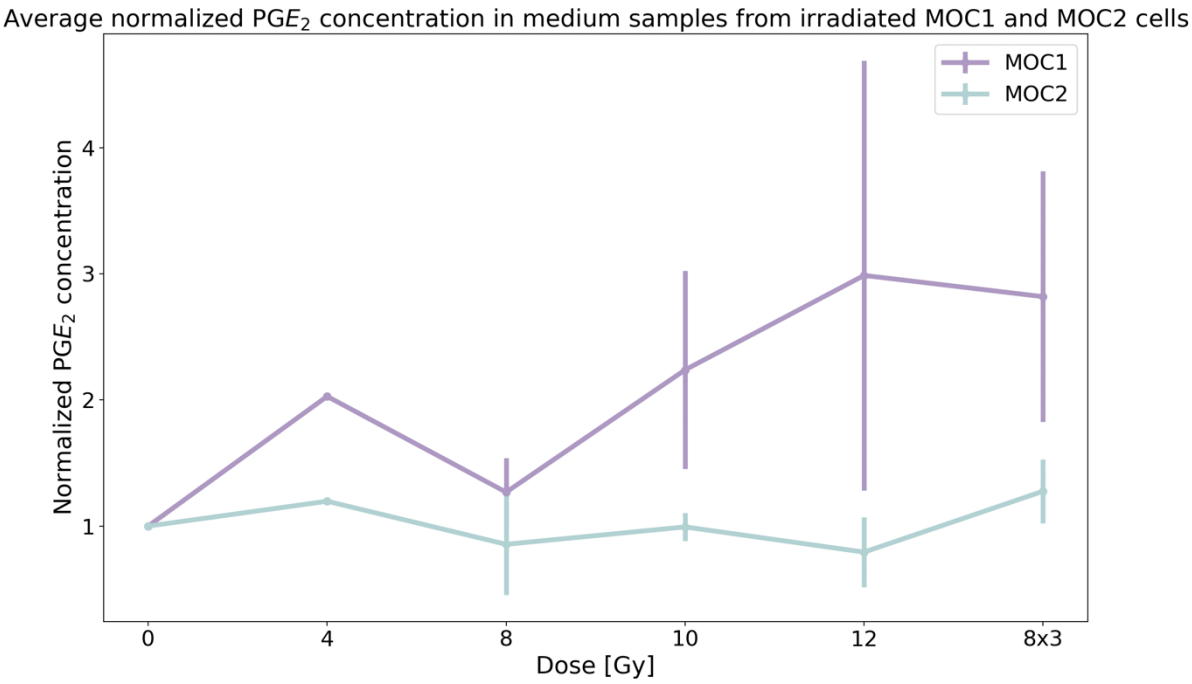

Figure 42: ***The normalized PGE_2 concentration in medium from MOC1 and MOC2 cells after irradiation****. The samples were harvested 24 hours after the total dose was delivered. For MOC1 the data consist of the doses 4 Gy (n=1), 8 Gy (n=3), 10 Gy (n=3), 12 Gy (n=2) and three fractions of 8 Gy (n=3), and for MOC2 the doses tested was 4 Gy (n=1), 8 Gy (n=2), 10 Gy (n=2), 12 Gy (n=3) and three fractions of 8 Gy (n=3), where 'n' is number of repetitions. The data was calculated individually, and then averaged. This caused a high uncertainties and very variable data. This can be explained by variation in the data caused by the ELISA analysis, and not by the concentrations in the samples. Another analysis method was used based on this. The error bars represent the standard error of the mean. Only one experiment was analyzed for 4 Gy, therefore there are no error bars.*

8.3 P-values and t-values from statistical test performed on the data

Table 24: The table states the p-values and t-values from t-tests on PD-L1 signal between unirradiated MOC1 control cells and MOC1 cells that received one-fraction of photon radiation. The t-tests were performed on the data for the doses: 4 Gy (n=6), 5 Gy (n=3), 8 Gy (n=6), 10 Gy (n=3), 12 Gy (n=5), where 'n' represents number of experiments. The tests were performed by using the function ttest_ind from scipy.stats in Python3.

Dose [Gy]	4	5	8	10	12
p-value	0.9656	0.0004	0.06	0.008	0.012
t-value	0.0458	48.7183	2.56	10.7000	4.326

Table 25: The table states the p-valuse and t-values from t-tests on PD-L1 signal between unirradiated MOC2 control cells and MOC2 cells that received one-fraction of photon radiation. The t-tests were performed on the data for the doses: 4 Gy (n=6), 5 Gy (n=3), 8 Gy (n=6), 10 Gy (n=3), 12 Gy (n=5), where 'n' represents number of experiments. The tests were performed by using the function ttest_ind from scipy.stats in Python3.

Dose [Gy]	4	5	8	10	12
p-value	0.082	0.038	0.074	0.43	0.002
t-value	2.307	4.9844	2.400	0.98	7.131

Table 26: The table states the p-values and t-values from t-tests between the PD-L1 signal after one-fraction of photon radiation, on MOC1 and MOC2 cells. The t-tests were performed on the data for the doses: 4 Gy (n=6), 5 Gy (n=3), 8 Gy (n=6), 10 Gy (n=3), 12 Gy (n=5), where 'n' represents number of experiments. The tests were performed by using the function ttest_ind from scipy.stats in Python3.

Dose [Gy]	4	5	8	10	12
p-value	0.343	0.024	0.41	0.11	0.097
t-value	-1.029	5.693	0.877	2.46	2.062

Table 27: The table states the p-values and t-values from t-tests between the PD-L1 signal on MOC1 control cells and on irradiated MOC1 cells with two fractions of photon radiation. The t-test were performed on the data for the doses: 2+2 Gy (n=3), 4+4 Gy (n=3), and 6+6 Gy (n=3), where 'n' represents number of experiments. The tests were performed by using the function ttest_ind from scipy.stats in Python3.

Dose [Gy]	2+2	4+4	6+6
p-value	0.963	0.213	0.0078
t-value	-0.0525	1.8063	11.3434

Table 28: The table states the p-values and t-values from t-tests between the PD-L1 signal on MOC2 control cells against MOC2 cells after two-fractions of photon radiation. The t-tests were performed on the data for the doses: 2+2 Gy (n=3), 4+4 Gy (n=3), and 6+6 Gy (n=3), where 'n' represents number of experiments. The tests were performed by using the function ttest_ind from scipy.stats in Python3.

Dose [Gy]	2+2	4+4	6+6
p-value	0.029	0.12	0.026
t-value	5.693	2.61	6.082

Table 29: The table states the p-values and t-values from t-tests between the PD-L1 signal on MOC1 and MOC2 cells after two-fractions of photon radiation. The t-tests were performed on the data for the doses: 2+2 Gy (n=3), 4+4 Gy (n=3), and 6+6 Gy (n=3), where 'n' represents number of experiments. The tests were performed by using the function ttest_ind from scipy.stats in Python3.

Dose [Gy]	2+2	4+4	6+6
p-value	0.239	0.158	0.012
t-value	-1.579	-1.7746	4.412

Table 30: The table states the p-value and t-value from a t-test between the PD-L1 signal on unirradiated MOC1 cells and MOC1 cells after three fractions of photon radiation. The t-test was performed on the data for the doses: 8+8+8 Gy (n=3) where 'n' represents number of experiments. The tests were performed by using the function ttest_ind from scipy.stats in Python3.

Dose [Gy]	8+8+8
p-value	0.012
t-value	9.079

Table 31: The table states the p-value and t-value from a t-test between the PD-L1 signal on unirradiated MOC2 cells and MOC2 cells after three fractions of photon radiation. The t-test was performed on the data for the doses: 8+8+8 Gy (n=3) where 'n' represents number of experiments. The tests were performed by using the function ttest_ind from scipy.stats in Python3.

Dose [Gy]	8+8+8
p-value	0.077
t-value	3.394

Table 32: The table states the p-value and t-value from a t-test between the PD-L1 signal on MOC1 and MOC2 cells, after three fractions of photon radiation. The t-test was performed on the data for the doses: 8+8+8 Gy (n=3) where 'n' represents number of experiments. The tests were performed by using the function ttest_ind from scipy.stats in Python3.

Dose [Gy]	8+8+8
p-value	0.155
t-value	-2.201

Table 33: The table states the p-values and t-values from t-tests between the PD-L1 signal on MOC1 cells after one and two fractions of the same total dose of photon radiation. The t-tests were performed on the data for the total doses: 4, 8 and 12 Gy. One fraction data consist of 5 experiments, and two fractions consists of 3 experiments. The tests were performed by using the function ttest_ind from scipy.stats in Python3.

Total dose [Gy]	4	8	12
p-value	0.947	0.171	0.929
t-value	0.069	1.580	0.093

Table 34: The table states the p-values and t-values from t-tests performed on the PD-L1 signal between MOC2 cells after one and two fractions of the same total dose of photon radiation. The t-tests were performed on the data for the total doses: 4, 8 and 12 Gy. One fraction consists of 5 experiments, and two fractions consists of 3 experiments. The tests were performed by using the function ttest_ind from scipy.stats in Python3.

Total dose [Gy]	4	8	12
p-value	0.747	0.328	0.756
t-value	-0.339	-1.150	0.328

Table 35: The table states the p-values and t-values from t-tests on forward scatter signal between unirradiated MOC1 control cells and MOC1 cells that received one, two and three-fractions of photon radiation. The t-tests were performed on 16 control values and the data for the doses: 4 Gy (n=4) 8 Gy (n=4), 12 Gy (n=11), 6+6 (n=4) and 8+8+8 (n=12), where 'n' represents number of signal values. The tests were performed by using the function ttest_ind from scipy.stats in Python3.

Dose [Gy]	4	8	12	6+6	8+8+8
p-value	0.019	$6.788 \cdot 10^{-10}$	0.0002	$2.810 \cdot 10^{-6}$	$5.250 \cdot 10^{-20}$
t-value	-3.226	-21.540	-5.5464	-18.246	-25.925

Table 36: The table states the p-values and t-values from t-tests on forward scatter signal between unirradiated MOC2 control cells and MOC2 cells that received one, two and three-fractions irradiation of photon radiation. The t-test is performed on 16 control values and the data for the doses: 4 Gy (n=4) 8 Gy (n=4), 12 Gy (n=12), 6+6 (n=4) and 8+8+8 (n=12) where 'n' represents number of signal values. The tests were performed by using the function ttest_ind from scipy.stats in Python3.

Dose [Gy]	4	8	12	6+6	8+8+8
p-value	$3.707 \cdot 10^{-5}$	$8.511 \cdot 10^{-13}$	$5.820 \cdot 10^{-5}$	0.0004	0.002
t-value	-5.873	-18.472	-5.791	-4.3091	-3.852

Table 37: The table states the p-values and t-values from t-tests between the forward scatter signal on MOC1 and MOC2 cells, after one-, two and three-fractions irradiation of photon radiation. The t-tests were performed on the data for the doses: 4 Gy (n=4) 8 Gy (n=4), 12 Gy (MOC1 n=11, MOC2 n=12), 6+6 (n=4) and 8+8+8 (n=12) where 'n' represents number of experiments. The tests were performed by using the function ttest_ind from scipy.stats in Python3.

Dose [Gy]	4	8	12	6+6	8+8+8
p-value	0.357	0.0002	0.011	0.0002	$3.350 \cdot 10^{-10}$
t-value	1.052	17.257	3.009	19.072	11.252

Table 38: The table states the p-values and t-values from t-tests between the unspecific binding signal on MOC1 and MOC2 cells after one-, two and three-fractions irradiation of photon radiation. The t-tests were performed on the data for the doses: 4 Gy (n=2) 8 Gy (n=2), 12 Gy (n=6), 6+6 (n=2) and 8+8+8 (n=6) where 'n' represents number of experiments. The tests were performed by using the function ttest_ind from scipy.stats in Python3.

Dose [Gy]	4	8	12	6+6	8+8+8
p-value	0.162	0.08	0.014	0.290	0.270
t-value	3.825	7.416	3.399	1.955	1.232